

Field Line Resonance in Two and a Half Dimensions

DRAFT VERSION CREATED ON APRIL 6, 2016

1

© Charles A. McEachern 2016

2



3

The text of this work is licensed under a Creative Commons

Attribution-ShareAlike 4.0 International license.

4

⁵ Acknowledgements

⁶ Acknowledgement placeholder.

⁷ Dedication

⁸ Dedication placeholder.

Abstract

¹⁰ Abstract placeholder.

Contents

¹¹	Acknowledgements	i
¹³	Dedication	ii
¹⁴	Abstract	iii
¹⁵	List of Tables	vii
¹⁶	List of Figures	viii
¹⁷	1 Introduction	1
¹⁸	1.1 Structure of the Present Work	2
¹⁹	2 The Near-Earth Environment	4
²⁰	2.1 The Outer Magnetosphere	4
²¹	2.2 The Inner Magnetosphere	6
²²	2.3 The Ionosphere	8
²³	2.4 Geomagnetic Storms and Substorms	9
²⁴	3 Field Line Resonance	11
²⁵	3.1 Harmonic Structure	14
²⁶	3.2 Azimuthal Modenumber	17
²⁷	3.3 Poloidal and Toroidal Polarizations	18
²⁸	3.4 Giant Pulsations	20
²⁹	3.5 Motivations for the Present Work	21

30	4 Waves in Cold Resistive Plasma	24
31	4.1 Guided Propagation	26
32	4.2 Compressional Propagation	27
33	4.3 High Altitude Limit	29
34	4.4 Implications to the Present Work	30
35	5 “Tuna Half” Dimensional Model	32
36	5.1 Coordinate System	33
37	5.2 Physical Parameter Profiles	37
38	5.3 Driving	40
39	5.4 Maxwell’s Equations	43
40	5.5 Boundary Conditions	47
41	6 Electron Inertial Effects	52
42	6.1 The Boris Factor	53
43	6.2 Parallel Currents and Electric Fields	55
44	6.3 Inertial Length Scales	61
45	6.4 Discussion	62
46	7 Numerical Results	64
47	7.1 Finite Poloidal Lifetimes: Dayside	65
48	7.2 Spatial Distribution of Energy: Dayside	70
49	7.3 Finite Poloidal Lifetimes: Nightside	75
50	7.4 Spatial Distribution of Energy: Nightside	79
51	7.5 Modenumber and Compressional Coupling	82
52	7.6 Ground Signatures and Giant Pulsations	86
53	7.7 Discussion	90
54	8 Observations	92
55	8.1 Sampling Bias and Event Selection	93
56	8.2 Rate of Pc4 Events	96
57	8.3 Rate of Pc4 Events by Amplitude	99
58	8.4 Rate of Pc4 Events by Frequency	102

59	8.5 Rate of Pc4 Events by Phase	103
60	8.6 Rate of Pc4 Events by Spectral Width	106
61	8.7 Discussion	107
62	9 Conclusion	108
63	9.1 Summary of Results	108
64	9.2 Future Work	108
65	References	110

⁶⁶ List of Tables

⁶⁷	3.1 IAGA Magnetic Pulsation Frequency Bands	12
⁶⁸	5.1 Typical Parameters for the Tuna Density Profile	38
⁶⁹	5.2 Integrated Atmospheric Conductivity	48

⁷⁰ List of Figures

⁷¹ 2.1	Outer Magnetosphere Cutaway	5
⁷² 2.2	Inner Magnetosphere Cutaway	7
⁷³ 3.1	Alfvén Bounce Frequencies	13
⁷⁴ 3.2	First and Second Harmonic Resonances	15
⁷⁵ 3.3	Large and Small Azimuthal Modenumbers	17
⁷⁶ 3.4	Poloidal Mode Structure	19
⁷⁷ 3.5	Toroidal Mode Structure	20
⁷⁸ 4.1	Compressional Alfvén Wave Cutoff Frequencies	31
⁷⁹ 5.1	Nonorthogonal Dipole Grid	37
⁸⁰ 5.2	Alfvén Speed Profiles	39
⁸¹ 5.3	Ionospheric Conductivity Profiles	40
⁸² 5.4	Decreasing Penetration with Increasing Modenumber	42
⁸³ 5.5	Sym-H for June 2013 Storm	43
⁸⁴ 6.1	Plasma Frequency Profile	54
⁸⁵ 6.2	Electric Field Snapshots	56
⁸⁶ 6.3	Current and Poynting Flux at 100 km	57
⁸⁷ 6.4	Current and Poynting Flux at 1000 km	59
⁸⁸ 6.5	Power Density at the Ionosphere	60
⁸⁹ 6.6	Parallel Electric Fields by Perpendicular Grid Resolution	62
⁹⁰ 7.1	Poloidal and Toroidal Energy: Quiet Day, Typical Plasmasphere	68
⁹¹ 7.2	Poloidal and Toroidal Energy: Quiet Day, Large Plasmasphere	69
⁹² 7.3	Radial Distribution of Poloidal Energy: Quiet Day, Typical Plasmasphere	72
⁹³ 7.4	Radial Distribution of Poloidal Energy: Quiet Day, Large Plasmasphere	73

94	7.5 Radial Distribution of Toroidal Energy: Quiet Day	74
95	7.6 Poloidal and Toroidal Energy: Active Night, Driving at $L = 5$	77
96	7.7 Poloidal and Toroidal Energy: Active Night, Driving at $L = 6$	78
97	7.8 Radial Distribution of Poloidal Energy: Active Night, Driving at $L = 6$	80
98	7.9 Radial Distribution of Toroidal Energy: Active Night	81
99	7.10 Compressional Coupling to the Poloidal Mode: Quiet Day	84
100	7.11 Compressional Coupling to the Poloidal Mode: Quiet Night	85
101	7.12 Dayside Ground Magnetic Fields	88
102	7.13 Nightside Ground Magnetic Fields	89
103	8.1 Distribution of Usable Van Allen Probe Data	95
104	8.2 Observation Rate of Pc4 Events	97
105	8.3 Observation Rate of Pc4 Events by Mode	99
106	8.4 TEST FIGURE	100
107	8.5 TEST FIGURE	101
108	8.6 TEST FIGURE	102
109	8.7 TEST FIGURE	103
110	8.8 TEST FIGURE	104
111	8.9 TEST FIGURE	105
112	8.10 TEST FIGURE	106
113	8.11 TEST FIGURE	107

¹¹⁴ **Chapter 1**

¹¹⁵ **Introduction**

¹¹⁶ 1859 was a pivotal year in human history. The United States moved steadily toward
¹¹⁷ the American Civil War, which would abolish slavery and consolidate the power of
¹¹⁸ the federal government. A slew of conflicts in Southern Europe, such as the Austro-
¹¹⁹ Sardinian War, set the stage for the unification of Italy. The Taiping Civil War — one
¹²⁰ of the bloodiest conflicts of all time — is considered by many to mark the beginning
¹²¹ of modern Chinese history. *Origin of Species* was published. The first transatlantic
¹²² telegraph cable was laid.

¹²³ Meanwhile, ambivalent to humanity, the Sun belched an intense burst of charged parti-
¹²⁴ cles and magnetic energy directly at Earth. The resulting geomagnetic storm¹ caused
¹²⁵ telegraph systems to fail across the Western hemisphere, electrocuting operators and
¹²⁶ starting fires[36, 97]. Displays of the northern lights were visible as far south as Cuba.

¹²⁷ The Solar Storm of 1859 was perhaps the most powerful in recorded history, but by no
¹²⁸ means was it a one-time event. The Sun discharges hundreds of coronal mass ejections
¹²⁹ (CMEs) per year, of all sizes, in all directions. In fact, a comparably large CME narrowly
¹³⁰ missed Earth in 2012[73]. Had it not, it's estimated it would have caused widespread,
¹³¹ long-term electrical outages, with a damage toll on the order of 10^{12} dollars[67].

¹The Solar Storm of 1859 is also called the Carrington Event, after English astronomer Richard Carrington. He drew a connection between the storm's geomagnetic activity and the sunspots he had observed the day before.

132 The Sun’s extreme — and temperamental — effect on Earth’s magnetic environment
133 makes a compelling case for the ongoing study of space weather. Such research has
134 evolved over the past century from sunspot counts and compass readings to multi-
135 satellite missions and supercomputer simulations. Modern methods have dramatically
136 increased humanity’s understanding of the relationship between the Sun and the Earth;
137 however, significant uncertainty continues to surround geomagnetic storms, substorms,
138 and the various energy transport mechanisms that make them up.

139 The present work focuses in particular on the phenomenon of field line resonance: Alfvén
140 waves bouncing between the northern and southern hemispheres. Such waves play an
141 important part in the energization of magnetospheric particles, the transport of energy
142 from high to low altitude, and the driving of currents at the top of the atmosphere.

143 1.1 Structure of the Present Work

144 Chapter 2 surveys the near-Earth environment. Prominent features of the magneto-
145 sphere are defined. The response of the magnetosphere to transient solar wind events
146 is summarized.

147 Chapter 3 introduces the field line resonance phenomenon, in terms of both the under-
148 lying physics and notable work on the topic. Jargon is introduced to clarify important
149 elements of wave structure. Several open questions about field line resonances (FLRs)
150 are offered as motivations for the present work.

151 Chapter 4 lays the groundwork for a numerical model by exploring the fundamental
152 equations of waves in a cold, resistive plasma — such as Earth’s magnetosphere. Char-
153 acteristic scales are gleaned from the resulting dispersion relations.

154 Chapter 5 presents Tuna, a new two and a half dimensional simulation designed specif-
155 ically for the realistic modeling of FLRs. Tuna’s non-orthogonal geometry, height-
156 resolved ionosphere, novel driving mechanism, and coupling to the atmosphere are ex-
157 plained.

158 Chapter 6 considers the addition of electron inertial effects to Tuna, touches on what
159 can be learned from them, and shows that they incur an unreasonable computational
160 cost. (Electron inertia is neglected in the results presented in other chapters.)

161 Chapter 7 describes the core numerical results of the work, unifying several of the
162 questions posed in Chapter 3. Significant depth is added to past work on finite poloidal
163 lifetimes[65, 79]. Interplay between poloidal-toroidal coupling, shear-compressional cou-
164 pling, and Joule dissipation is considered from several angles.

165 Chapter 8 puts the numerical results in physical context through the analysis of data
166 from the Van Allen Probes mission. FLR occurrence rates are considered in terms of
167 location, mode structure, and polarization – parameters which have been only partially
168 addressed by other recent FLR surveys[17, 71].

169 Chapter 9 briefly summarizes the results shown in the above chapters — the code
170 development, analysis of numerical results, and satellite observation — and suggests
171 further directions.

¹⁷² **Chapter 2**

¹⁷³ **The Near-Earth Environment**

¹⁷⁴ From Earth’s surface to a height of a hundred kilometers or so, the atmosphere is a
¹⁷⁵ well-behaved fluid: a collisional ensemble of neutral atoms. Higher up, its behavior
¹⁷⁶ changes dramatically. As altitude increases, solar ultraviolet radiation becomes more
¹⁷⁷ intense, which ionizes atmospheric atoms. Density also decreases, slowing collisional
¹⁷⁸ recombination. Whereas the neutral atmosphere is held against Earth’s surface by
¹⁷⁹ gravity, the motion of charged particles is dominated by Earth’s geomagnetic field, as
¹⁸⁰ well as the electromagnetic disturbances created as that field is hammered by the solar
¹⁸¹ wind.

¹⁸² The present section outlines the structure of the magnetosphere; that is, the region of
¹⁸³ space governed primarily by Earth’s magnetic field. Particular emphasis is placed on
¹⁸⁴ structures which relate closely to field line resonance.

¹⁸⁵ **2.1 The Outer Magnetosphere**

¹⁸⁶ Plasma behavior within Earth’s magnetosphere is ultimately driven by the solar wind: a
¹⁸⁷ hot (~ 100 eV), fast-moving (~ 100 km/s) plasma threaded by the interplanetary magnetic
¹⁸⁸ field (~ 1 nT)¹. The density of the solar wind is on the order of 10^6 /cm³; in a laboratory

¹Listed values correspond to the solar wind at Earth’s orbit.

189 setting, this would constitute an ultra-high vacuum (atmospheric density at sea level is
190 $\sim 10^{19} / \text{cm}^3$), but compared to much of the magnetopause it's quite dense.



Figure 2.1: TODO: The outer magnetosphere...

191 The magnetosphere's outer boundary represents a balance between the solar wind dy-
192 namic pressure and the magnetic pressure of Earth's dipole field. On the dayside, the
193 dipole is compressed, pushing this boundary to within about $10 R_E$ of Earth². The
194 nightside magnetosphere is stretched into a long tail which may exceed $50 R_E$ in width
195 and $100 R_E$ in length.

196 When the interplanetary magnetic field opposes the geomagnetic field at the nose of
197 the magnetosphere, magnetic reconnection occurs. Closed magnetospheric field lines
198 "break," opening up to the interplanetary magnetic field³. They then move tailward

²Distances in the magnetosphere are typically measured in units of Earth radii: $1 R_E \equiv 6378 \text{ km}$.

³Closed field lines connect at both ends to the magnetic dynamo at Earth's core. Open field lines meet Earth at only one end; the other connects to the interplanetary magnetic field. The distinction is important because charged particle motion is guided by magnetic field lines, as discussed in Chapter 3.

199 across the poles, dragging their frozen-in plasma with them⁴. Reconnection in the tail
200 allows magnetic field lines to convect back to the day side, across the flanks. This
201 process is called the Dungey cycle[23].

202 Viewed from the north, the Dungey cycle involves a clockwise flow of flux and plasma on
203 the dusk side and a counterclockwise flow on the dawn side. The motion is accompanied
204 by a convection electric field, per Ohm's law⁵.

205 **TODO:** Jets from magnetic reconnection... release of magnetic tension!

206 Consistent with Ampère's law, the interplanetary magnetic field is separated from the
207 magnetosphere by a current sheet: the magnetopause. On the dayside, the magne-
208 topause current flows duskward; on the nightside, it flows downward around the mag-
209 netail.

210 Plasma within the tail is cool ($\sim 100 \text{ eV}$) and rarefied ($\sim 10^{-2} / \text{cm}^3$). Earth's dipole is
211 significantly deformed in the magnetotail; field lines in the northern lobe of the tail
212 points more or less Earthward, and vice versa. The two lobes are divided by the plasma
213 sheet, which is comparably hot ($\sim 10^3 \text{ eV}$) and dense ($\sim 1 / \text{cm}^3$). The plasma sheet
214 carries a duskward current which connects to the magnetopause current.

215 2.2 The Inner Magnetosphere

216 Within about **TODO:** $L \sim 10$ (where L is the McIlwain parameter⁶), the dipole
217 magnetic field is not appreciably deformed by the solar wind. As a result, the structures
218 in the inner magnetosphere follow closely from the motion of charged particles in an
219 ideal dipole field.

⁴In the outer magnetosphere (as well as most of the inner magnetosphere), collisions are so infrequent that magnetic flux is said to be “frozen in” to the plasma. Charged particles move freely along magnetic field lines, but cannot cross from one line to another. Compression of the magnetic field is synonymous with compression of the ambient plasma.

⁵In the case of an ideal plasma, Ohm's law takes the form $\underline{E} + \underline{U} \times \underline{B} = 0$.

⁶The McIlwain parameter L is used to index field lines in Earth's dipole geometry: $L \equiv \frac{r}{\sin^2 \theta}$ for colatitude θ and radius r in Earth radii. For example, the $L = 5$ field line passes through the equatorial plane at a geocentric radius of $5 R_E$, then meets the Earth at a colatitude of $\arcsin \sqrt{\frac{1}{5}} \sim 27^\circ$ (equally, a latitude of $\arccos \sqrt{\frac{1}{5}} \sim 63^\circ$).

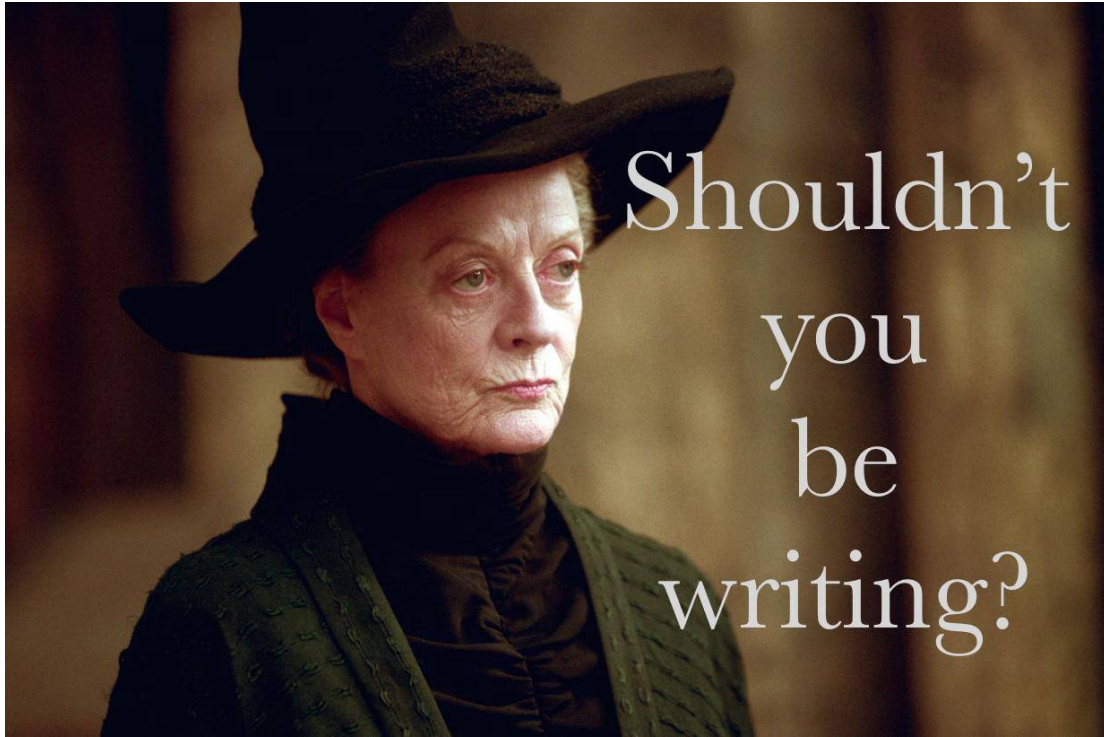


Figure 2.2: TODO: The inner magnetosphere...

- 220 The plasmasphere — a cold (~ 1 eV), dense ($10^2 / \text{cm}^3$ to $10^4 / \text{cm}^3$) torus of corotating
221 plasma — is formed by the outward drift of atmospheric ions along magnetic closed
222 field lines. Its outer boundary, is thought to represent a balance between the corotation
223 electric field (per the rotation of Earth's magnetic dipole) and the convection electric
224 field (associated with the convection of magnetic flux during the Dungey cycle). Particle
225 density drops sharply at the edge of the plasmasphere; the boundary is called the
226 plasmapause. The plasmapause typically falls around $L = 4$, though during prolonged
227 quiet times it can extend to $L = 6$ or larger.
- 228 Energetic particles trapped within the inner magnetosphere are divided into two popu-
229 lations.
- 230 The Van Allen radiation belts are made up of particles with energy above 10^5 eV or
231 so. The inner belt ($L \lesssim 2$) is primarily composed of protons, the decay remnants of

232 neutrons freed from the atmosphere by cosmic rays. The outer belt ($L \gtrsim 4$) is primarily
233 composed of high-energy electrons.

234 Particles with energies of 10^3 eV to 10^5 eV make up the ring current, which extends
235 from $L \sim 3$ to $L \sim 5$. Gradient-curvature drift carries ions and electrons in opposite
236 directions; the net result is a westward current. During quiet times, the ring current
237 causes magnetic a southward magnetic field on the order of 1 nT at Earth's equator⁷.

238 2.3 The Ionosphere

239 Earth's neutral atmosphere is an excellent insulator. Collisions are so frequent that
240 charged particles quickly thermalize and recombine. The breakdown of air molecules
241 into a conductive plasma (as happens during a lightning strike, for example) requires
242 electric fields on the order of 10^9 mV/m.

243 Currents are also suppressed by the magnetosphere. In the absence of collisions, elec-
244 trons and ions drift alongside one another in response to an electric field, creating no
245 net current perpendicular to the magnetic field⁸. Magnetic field lines are (to a good
246 approximation) equipotential contours; electric fields do not form along them to drive
247 parallel currents.

248 The ionosphere is a sweet spot between the two regimes. Collisions are frequent enough
249 to disrupt the drift of ions, but not frequent enough to immobilize the electrons. The
250 result is nonzero Pedersen and Hall conductivity, corresponding to current along the
251 electric field and in the $\underline{B} \times \underline{E}$ direction respectively. Collisions in the ionosphere
252 also give rise to a finite parallel conductivity, allowing for the formation of potential
253 structures along the magnetic field line.

254 **TODO: Field-aligned currents depend on the level of geomagnetic activity... but do**
255 **they ever completely go away?**

⁷For comparison, Earth's dipole field points north at the equator with a magnitude over 10^4 nT.

⁸The so-called E -cross- B drift is associated with a velocity of $\underline{U} = \frac{1}{B^2} \underline{E} \times \underline{B}$, independent of a charged particle's mass or sign.

256 The convection electric field (associated with the Dungey cycle, Section 2.1) drives Ped-
257 ersen currents in the ionosphere. It is these currents that give rise to the strongest mag-
258 netic fields on the ground. Pedersen currents flow downward on the flanks and duskward
259 across the poles. The currents remain divergence-free by connecting to field-aligned cur-
260 rents at the edges of the polar cap. The field-aligned currents, in turn, connect to the
261 magnetopause current, the cross-tail current, and the (partial) ring current.

262 When electron density is low, thermal velocities may be unable to carry enough current
263 to satisfy $\nabla \cdot \underline{J} = 0$. This leads to the formation of potential structures along geomagnetic
264 field lines in the ionosphere. Such structures accelerate particles along magnetic field
265 lines, leading to the precipitation of energetic particles into the atmosphere. As the
266 particles thermalize, they excite atmospheric atoms. The resulting spontaneous emission
267 is often in the visible spectrum, giving rise to the aurora.

268 **TODO:** Particles can also be excited by Alfvén waves... this probably goes in Chapter 3.
269

270 **2.4 Geomagnetic Storms and Substorms**

271 The quiet geomagnetic behavior described above is periodically disturbed by transient
272 solar phenomena such as corotating interaction regions (CIRs) and coronal mass ejec-
273 tions (CMEs). CMEs, as noted in Chapter 1, are bursts of unusually dense solar wind
274 which are ejected from regions of high magnetic activity on the Sun; they are most
275 common at the height of the eleven-year solar cycle. CIRs, on the other hand, occur
276 when a relatively fast region of the solar wind catches up to an earlier and slower-moving
277 pocket of solar wind, resulting in a pair of shockwaves.

278 During a storm, increased solar wind intensity results in enhanced magnetic reconnection
279 on the dayside. As the newly-opened field lines are swept tailward, the convection
280 electric field is strengthened. The plasmasphere — the outer boundary of which is
281 set by a balance between the convection electric field and the (more or less constant)
282 corotation electric field — sheds its outer layers. A large number of energetic particles
283 are also injected into the ring current[69].

284 The strength of the storm is gauged by the size of the magnetic perturbation created
285 by the ring current⁹. A small storm has a magnitude of 50 nT to 100 nT. Large storms
286 may reach 250 nT to 500 nT. The Carrington Event, mentioned in Chapter 1, is thought
287 to have exceeded 1700 nT[97].

288 The main phase of a storm typically lasts for several hours. Storm recovery — the grad-
289 ual return of the storm index to zero — typically lasts several days. The plasmapause
290 refilling occurs on timescales of **TODO: ???**. Geomagnetic storms occur tens of times
291 per year at the height of the solar cycle, and just a few times per year otherwise.

292 Whereas storms are prompted by large solar wind events on the dayside, geomagnetic
293 substorms are primarily a nightside occurrence. As flux accumulates in the tail, mag-
294 netic tension builds in the stretched field lines. A substorm is an impulsive release of
295 that tension.

296 **TODO: Phases of a substorm.** Definition of a substorm comes from [1]. Revised by [70].

297

298 At substorm onset, a burst of reconnection occurs in the tail. A jet of plasma is launched
299 Earthward from the reconnection site (and another is launched tailward, and lost to the
300 solar wind). The Earthward plasma injection injects particles into the ring current.
301 The outer radiation belt is depleted, then repopulated. Energetic particles precipitate
302 into the atmosphere, giving rise to a distinctive **TODO: hour-long** sequence of auroral
303 signatures.

304 Concurrent with substorm onset, impulsive Alfvén waves are observed with periods of
305 a minute or two. The precise ordering of events — whether reconnection causes the
306 waves, or vice versa, or if they share a common cause — remains controversial.

307 Each substorm lasts several hours, including the time it takes for the ring current to
308 return to pre-substorm levels. Several substorms may occur per day during quiet times.
309 During a storm, substorms become far more frequent; by the time one has ended,
310 another may have already begun.

⁹The most commonly used storm index is Dst, which is computed hourly using measurements from several ground magnetometers near the equator. The Sym-H index, used in Section 5.3, is computed once per minute.

311 **Chapter 3**

312 **Field Line Resonance**

- 313 The motion of a charged particle in a dipole field can be described in terms of three
314 fundamental motions. The first is cyclotron motion: a particle orbits around a magnetic
315 field line in accordance with the Lorentz force. The second is bounce motion: while
316 orbiting, the particle moves along the field line like a bead on a wire, back and forth
317 between the northern and southern hemispheres¹. The third is drift motion: as particles
318 orbit and bounce, they also move azimuthally around Earth per the gradient-curvature
319 drift.
- 320 Characteristic timescales for each of the above motions depend on particle energy. Elec-
321 tron cyclotron motion is on the order of TODO: ... in the ionosphere, and closer to
322 TODO: ... in the tail; ions gyrate slower by three orders of magnitude due to their
323 larger mass. TODO: Bounce... Drift...
- 324 Wave-particle resonance arises when a particle's periodic motion matches with the fre-
325 quency of a coincident electromagnetic wave[25, 64, 75, 86]. In the particle's rest frame,
326 the wave then appears as a net electric field. This allows a net movement of energy

¹As a particle approaches Earth, it experiences an ever-stronger magnetic field. The particle's perpendicular kinetic energy increases in proportion with the magnetic field in order to conserve its first adiabatic invariant. When the perpendicular kinetic energy can no longer increase — that is, when the parallel kinetic energy is zero — the particle bounces back. (If the parallel kinetic energy is sufficiently large, the particle doesn't bounce; it precipitates into the atmosphere.)

327 between the wave and the particle. The interaction is analogous to a surfer moving
 328 along with — and being accelerated by — a wave in the ocean.

329 In the present work, the waves in question are field line resonances (FLRs). An FLR
 330 is a standing harmonic on a geomagnetic field line. It can also be envisioned as a
 331 superposition of traveling waves, reflecting back and forth between its northern and
 332 southern foot points at the conducting ionosphere. These waves travel at the Alfvén
 333 speed². The fundamental equations of field line resonance were presented by Dungey in
 334 1954[22]; since then, they have remained a topic of active study.

335 So-called ultra low frequency waves — of which FLRs are a subset — are categorized
 336 by morphology. Continuous (long-lived) pulsations are termed Pc, while irregular pul-
 337 sations are called Pi. Within each are a number of frequency bands; see Table 3.1[46].

Table 3.1: IAGA Magnetic Pulsation Frequency Bands

	Pc1	Pc2	Pc3	Pc4	Pc5	Pi1	Pi2
Period (s)	0.2–5	5–10	10–45	45–150	150–600	1–40	40–150
Frequency (mHz)	200–5000	100–200	22–100	7–22	2–7	25–1000	7–25

338 **TODO:** Boundaries between wave bands are, in practice, not strict. They are sometimes
 339 fudged to better match phenomenological boundaries.

340 FLRs fall into the Pc3, Pc4, and Pc5 ranges. The present work focuses specifically
 341 on the Pc4 band: waves with periods of a minute or two. Frequencies in the Pc4
 342 range typically coincide with Alfvén bounce times³ near the plasmapause: $L \sim 4$ to
 343 $L \sim 6$ [3, 17, 26, 57]⁴. In fact, the large radial gradients in the Alfvén speed near the
 344 plasmapause act as an effective potential well, trapping FLRs[16, 51, 54, 55, 63, 89].

²The Alfvén speed is given by v_A is given by $v_A^2 \equiv \frac{B^2}{\mu_0 \rho}$, where B is the magnitude of the magnetic field, μ_0 is the magnetic constant, and ρ is the mass density of the ambient plasma. It can vary by several orders of magnitude over the length of a magnetic field line.

³The Alfvén frequency is the inverse of the Alfvén bounce time: $\frac{2\pi}{\omega_A} \equiv \oint \frac{dz}{v_A}$.

⁴Not coincidentally, these are the same L -shells where the Van Allen Probes spend most of their time; see Chapter 8.

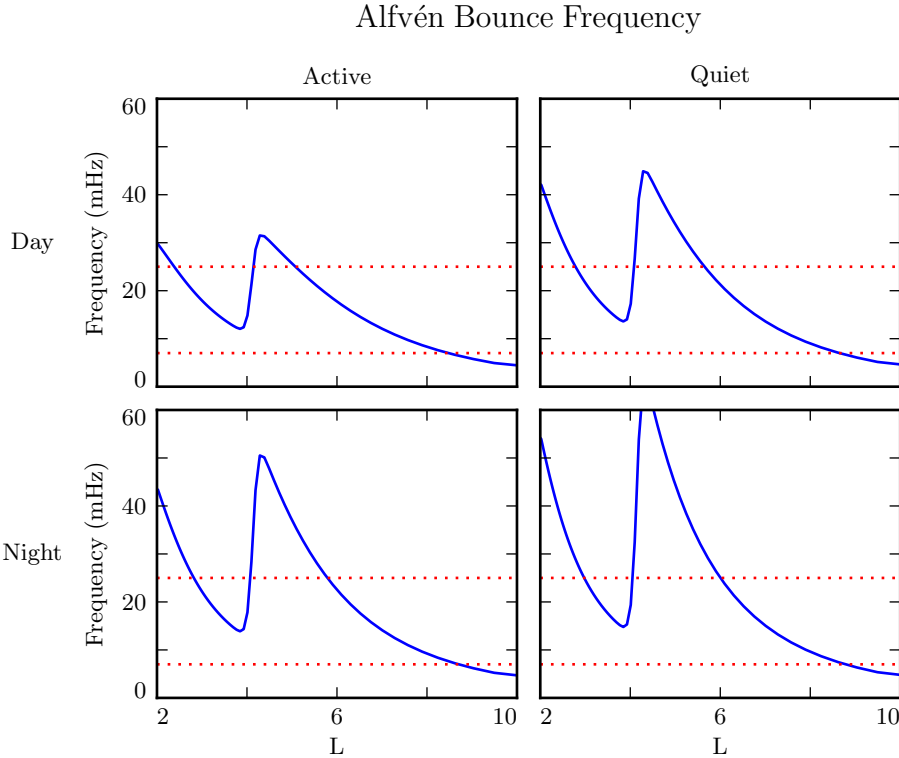


Figure 3.1: The above are bounce frequencies for an Alfvén wave moving back and forth along a geomagnetic field line. Alfvén speeds are computed based on profiles from Kelley[49], as discussed in Section 5.2. Notably, the bounce frequency depends significantly on the position of the plasmasphere, taken here to be at $L = 4$. Dotted lines indicate the Pc4 frequency range: 7 mHz to 25 mHz.

- 345 In addition to being radially localized, FLRs in the Pc4 frequency band (also called Pc4
- 346 pulsations, or just Pc4s) are localized in magnetic local time (MLT⁵). They have also
- 347 been shown to occur preferentially on the dayside, during storms or storm recovery[3,
- 348 17, 26, 53, 57, 98].
- 349 In the inner magnetosphere, the Alfvén frequency — and thus the frequency of FLRs
- 350 — often coincides with integer or half-integer⁶ multiples of particle drift frequencies[18].

⁵Noon points toward the Sun and midnight away from it, with 06:00 and 18:00 at the respective dawn and dusk flanks.

⁶See Section 3.1.

351 The resulting wave-particle interactions can give rise to significant energization and
352 radial diffusion of the particles. In some cases, the waves also include an electric field
353 parallel to the background magnetic field, contributing to the precipitation of energetic
354 particles into the neutral atmosphere[33, 34, 94, 104].

355 The present chapter introduces the structural characteristics of FLRs, how those charac-
356 teristics affect wave behavior, and several unresolved questions related to that behavior.

357 **TODO:** The polarization of long-period Alfven waves is rotated by $\sim 90^\circ$ when passing
358 through the ionosphere[42]. A wave that is azimuthally polarized in space is polarized
359 north-south on the ground, and vice versa. It has been noted specifically that Pgs
360 exhibit east-west polarized ground signatures[93].

361 **TODO:** Other planets[32]? Seems exciting but maybe not relevant.

362 3.1 Harmonic Structure

363 Wave structure along a geomagnetic field line is indicated by harmonic number. The
364 first (or fundamental) harmonic has a wavelength twice as long as the field line. It
365 exhibits an antinode in the perpendicular electric field at the equator, along with a
366 node in the perpendicular magnetic field. The second harmonic is a single wavelength
367 along the field line. Its perpendicular magnetic perturbation has an antinode at the
368 equator, while its perpendicular electric field has a node. Figure 3.2 shows a qualitative
369 sketch of each: a series of snapshots in time, in the rest frame of the wave. Perpendicular
370 electric and magnetic field perturbations are shown in blue and red respectively.

371 A first-harmonic FLR that is periodic or localized in the azimuthal direction is conducive
372 to drift-resonant wave-particle interactions[18, 76]. The particle is like a child on a swing:
373 whenever the path of the particle (or child) gets close to the wave (parent), it gets a
374 push, and always in the same direction. The wave fields spend half its time pointing
375 the other direction, just as the parent must shift their weight backward to get ready for
376 the next push, but at that point the particle (child) is far away.

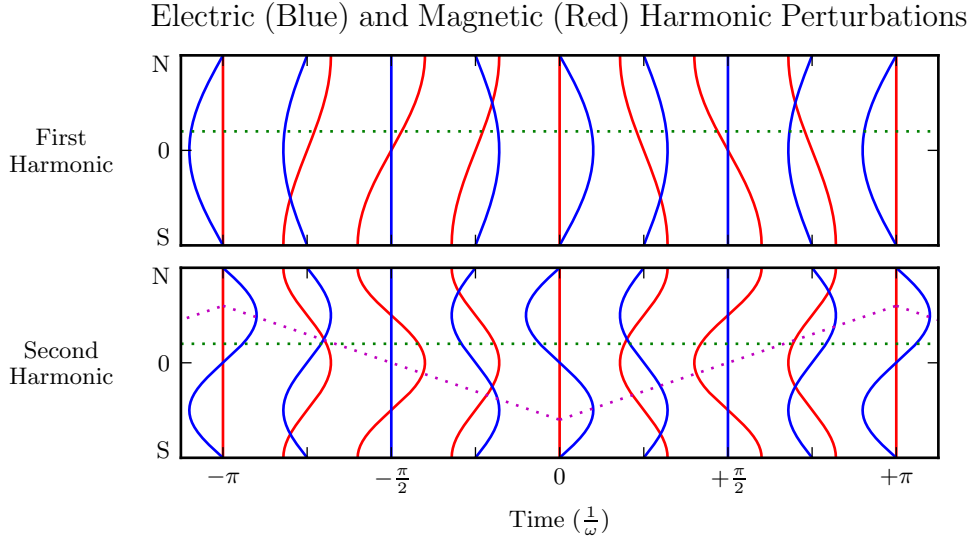


Figure 3.2: The first (or fundamental) harmonic has an antinode in its perpendicular electric field (blue) at the equator, along with a node in its perpendicular magnetic field perturbation (red). A single satellite can identify the first harmonic by the relative phase of the electric and magnetic field perturbations: an observer north of the equator (green) will see the magnetic field perturbation lead the electric field by 90° . The second harmonic is the opposite: it has an electric field node at the equator, and an observer north of the equator will see the magnetic field perturbation lag the electric field by 90° . The purple line sketches the path of a particle in drift-bounce resonance; in the particle’s rest frame, the electric field is always to the right. **TODO:** Actually, toroidal waves are flipped — Faraday’s law gives $\frac{\partial}{\partial t} B_x \sim \frac{\partial}{\partial z} E_y$ but $\frac{\partial}{\partial t} B_y \sim -\frac{\partial}{\partial z} E_x$.

377 Second-harmonic FLRs interact with particles through the drift-bounce resonance, which
 378 is slightly more complicated. As the particle drifts azimuthally, it also zig-zags north-
 379 south. The combination of those two periodic motions must align with the phase of
 380 the wave electric field. An example path is shown by the purple line in Figure 3.2: the
 381 particle experiences a rightward electric field throughout the wave’s oscillation.

The drift and drift-bounce resonance conditions are written, respectively[90]:

$$\omega - m\omega_D = 0 \quad \text{and} \quad \omega - m\omega_D = \omega_B \quad (3.1)$$

382 Where ω is the frequency of the wave, ω_D and ω_B are the particle's drift and bounce
383 frequencies respectively, and m is the wave's azimuthal modenumber, as discussed in
384 Section 3.2.

385 In principle, the first and second harmonics can be distinguished by their frequencies,
386 even from a single-point observation[15, 35]. In practice, however, this is not a reliable
387 approach[91]. There are significant uncertainties surrounding the number density profile
388 — and thus the Alfvén speed profile — along a geomagnetic field line.

389 Harmonic structure can also be deduced by noting the phase offset between the wave
390 magnetic field and its electric field (or the plasma velocity)[17, 93]. In Figure 3.2,
391 the green line indicates an observer just north of the magnetic equator. For the first
392 harmonic, the observer sees the electric field waveform lead the magnetic field by a
393 phase of 90° ; for the second harmonic, the electric field waveform lags by 90° . (South
394 of the equator, the signs are reversed.) Notably, this approach has only become viable
395 with the advent of satellites carrying both electric and magnetic field instrumentation,
396 such as THEMIS in 2007[4] and the Van Allen Probes⁷ in 2012[87].

397 Strictly speaking, the the phase offset of the electric and magnetic fields does not provide
398 the harmonic number — only its parity. It's reasonably safe to assume that an even mode
399 is the second harmonic; the second harmonic is by far the most commonly observed[45,
400 84, 92], due in part to its excitement by the antisymmetric balloon instability[9, 11,
401 13, 86]. However, the distinction between the first and third harmonics is not always
402 clear; this issue is discussed further in Chapter 8. Higher harmonics than that are not
403 expected in the Pc4 frequency band.

404 **TODO:** Second-harmonic FLRs are unlikely to cause ground signatures[93].

405 **TODO:** Dai found a nice event[18] that was unambiguously determined to be a fundamental-
406 mode Pc4 in drift-resonant interaction with $\sim 10^5$ eV ions. Consistent with [95]. Other
407 observations of odd harmonics: [105, 27].

⁷The Van Allen Probes were previously called RBSP, for Radiation Belt Storm Probes.

408 **3.2 Azimuthal Modenumber**

409 The wavelength of an FLR in the azimuthal direction is indicated by its azimuthal
410 wavelength. A wave with modenumber m has an azimuthal wavelength that spans $\frac{24}{m}$
411 hours in MLT.



Figure 3.3: TODO: Large and small azimuthal modenumbers.

412 Waves with small azimuthal modenumbers ($0 < m < 10$) are typically driven by broad-
413 band energy sources at the magnetosphere's boundary, such as variations in the so-
414 lar wind pressure[19, 39, 50, 108, 109], sporadic magnetic reconnection[43], or Kelvin-
415 Helmholtz waves on the magnetopause[10, 58, 85]. In the low- m regime, the shear and
416 compressional Alfvén waves are coupled, which allows energy to move across field lines
417 until the driving frequency lines up with the local Alfvén frequency[60]. Because of their
418 broadband energy source, low- m FLRs often have a mishmash of frequencies present in
419 their spectra[17].

- 420 When the azimuthal modenumber is large (or, equally, when the azimuthal wavelength
 421 is small), the shear and compressional Alfvén waves are decoupled[15, 79]⁸. As a result,
 422 FLRs must be driven from within the magnetosphere. Proposed energy sources include
 423 phase space gradients near the plasmapause[18], particularly as the plasmasphere refills
 424 after a storm or substorm[26, 56].
- 425 The ionosphere is known to attenuate waves with small spatial extent in the perpendic-
 426 ular direction[44, 103, 107]. As a result, FLRs may create no signature on the ground if
 427 their azimuthal modenumber is large. For example, a recent paper by Takahashi shows
 428 a strong (2 nT at $L \sim 10$), clear resonance with $|m| \gtrsim 70$ and no corresponding ground
 429 signature[91].

Southwood[86] and Glassmeier[30] show that a low frequency wave passing through the ionosphere on its way to Earth will be attenuated per

$$\frac{B_E}{B_I} = \frac{\Sigma_H}{\Sigma_P} \exp\left(-m \frac{R_I - R_E}{R_E \sin \theta}\right) \quad (3.2)$$

- 430 Where B_E and B_I are the magnetic field strengths at R_E (Earth's surface, 6783 km
 431 geocentric) and R_I (the ionosphere, \sim 6900 km geocentric) respectively. The integrated
 432 ionospheric Pedersen and Hall conductivities, Σ_P and Σ_H , are typically within a factor
 433 of two of one another. Field lines near the plasmapause can be traced to Earth at
 434 $\sin \theta \sim 0.4$. That is, by the time it reaches the ground, the magnetic field from an FLR
 435 with $m = 10$ is weaker by a factor of two; at $m = 100$, the factor is closer to 100.

436 3.3 Poloidal and Toroidal Polarizations

- 437 Based on polarization, each FLR can be classified as either poloidal or toroidal. The
 438 poloidal mode is a field line displacement in the meridional plane, as shown in Figure 3.4,
 439 with an accompanying electric field in the azimuthal direction. The toroidal mode's
 440 magnetic displacement is azimuthal, per Figure 3.5; the associated electric field is in the
 441 meridional plane.

⁸Equally, the strength of a wave's parallel component hint at its modenumber, a point which is revisited in Chapter 8.

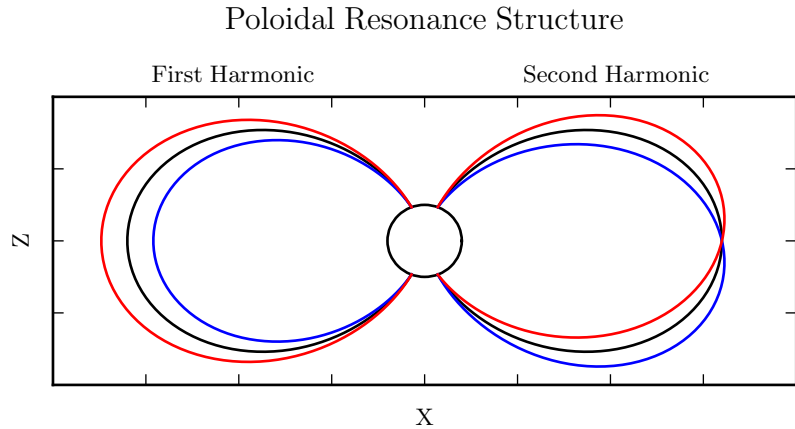


Figure 3.4: The poloidal resonance is a magnetic field in the meridional plane. The displacement is radial near the equator, and can be accompanied by enhancement in the parallel magnetic field near the ionosphere. The first harmonic is shown on the left, and the second harmonic on the right. Lines are colored red and blue only to contrast with the unperturbed black field line.

442 Both poloidal and toroidal waves are noted for their ability to contribute to the energiza-
 443 tion and radial diffusion of trapped particles. The poloidal mode interacts more strongly,
 444 since its electric field is aligned with the trapped particles’ drift motion. Poloidally-
 445 polarized waves are also more prone to creating magnetic signatures on the ground, due
 446 to ducting in the ionosphere[28, 37].

447 Toroidal modes have been shown to far outnumber poloidal modes[3]. Perhaps not
 448 coincidentally, poloidally-polarized waves rotate asymptotically to the toroidal mode[65,
 449 66, 79]. Poloidal waves with low azimuthal modenumber — such as those driven by
 450 broadband sources at the magnetopause — rotate on timescales comparable to their
 451 oscillation periods.

452 **TODO:** Fishbone instability[12, 68]. Like the poloidal mode, but for lab plasmas.

453 **TODO:** Poloidal and toroidal modes are coupled by the ionospheric Hall conductivity[48].
 454 The Hall conductivity also increases the “ringtime” of these resonances, allowing them

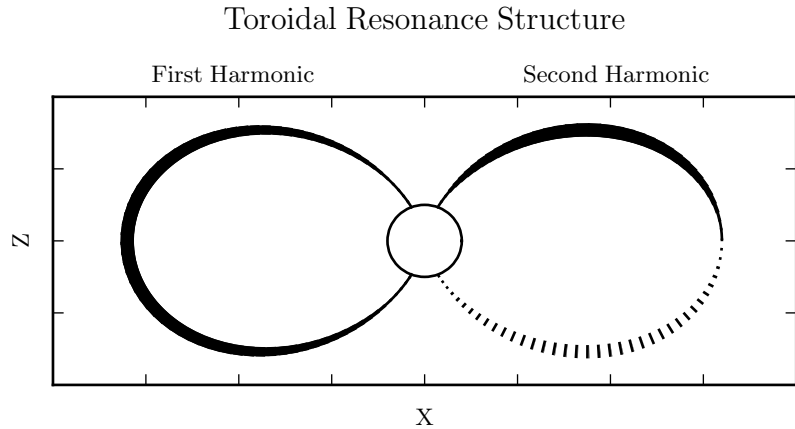


Figure 3.5: A toroidally-polarized FLR has a magnetic perturbation in the azimuthal direction, as shown. Bold lines are taken to be above the page, and dotted lines below the page, with the displacement indicated by the line's width. The first harmonic — where the entire field line oscillates in and out of the page — is shown on the left. The second harmonic is on the right, with northern and southern halves perturbed in opposite directions.

455 to oscillate through the inductive process rather than be dissipated as Joule heating[101].

456

457 TODO: Toroidal modes show a clear frequency dependence with L . Poloidal modes less
458 so. Citation...?

459 3.4 Giant Pulsations

460 The study of geomagnetic pulsations long predates satellites, sounding rockets, or even
461 the word “magnetohydrodynamics”⁹. Large, regular oscillations in the magnetic field
462 were noted as early as 1901[5]. Eventually, the term “giant pulsation,” or Pg, arose to
463 describe such pulsations.

⁹The term was first used by Alfvén in the 1940s[2].

464 On the ground, Pgs are notable for their strikingly sinusoidal waveforms, their eastward
465 drifts, and their specific occurrence pattern: Pgs are typically seen pre-dawn, at latitudes
466 of 60° to 70° . Pgs generally fall into the Pc4 frequency band¹⁰. Their harmonic structure
467 was a source of controversy for decades, but recent multisatellite observations seem to be
468 in agreement that they are odd harmonics, probably fundamental[31, 41, 52, 53, 90, 93].
469 They are poloidally polarized, with modenumbers $10 \lesssim m \lesssim 40$ [29, 41, 76, 82, 93].

470 Whereas FLRs are waves in space which may produce ground signatures, “giant pul-
471 sation” refers to the ground signature specifically¹¹. That is, Takahashi’s satellite ob-
472 servation of a sinusoidal, morningside, high- m , fundamental poloidal resonance was not
473 classified as a Pg because it did not produce a signal on the ground[91].

474 **TODO: Pgs are localized to within 2° to 5° in latitude[71, 90, 99].**

475 Due to their remarkably clear waveforms, Pgs are typically found by “visual inspection
476 of magnetometer data”[71]. Over the course of the past century, a number of multi-year
477 (sometimes multi-decade[7]) surveys have totaled nearly one thousand Pg events. On
478 average, a ground magnetometer near 66° magnetic latitude observes ~ 10 Pg events per
479 year[7, 40, 81, 88]. Observations are not distributed uniformly; rather, giant pulsations
480 become more common near the equinox and during times of low solar activity.

481 Unlike Pc4 pulsations in general, Pgs show no particular correlation with storm phase[71].
482 However, they do often occur as the magnetosphere recovers from a substorm[71, 82].

483 3.5 Motivations for the Present Work

484 A great deal has been learned — and continues to be learned — through observations of
485 field line resonance. However, the cost-to-benefit ratio is climbing. As summarized in the
486 sections above, FLR behavior depends significantly on harmonic structure, azimuthal
487 modenumber, and polarization — not to mention frequency, spectral width, and so

¹⁰The Pc4 range is periods of 45 s to 140 s, while Pgs are often said to range from 60 s to 200 s[7].

¹¹Historically, the wave designations shown in Table 3.1 all referred to ground phenomena. Over time,
they have come to describe satellite observations as well, including those without corresponding sig-
natures on the ground.

488 on. With each degree of freedom comes the necessity for an additional simultaneous
489 observation.

490 Similarly, as FLRs have been shown to depend on ever-more-specific magnetospheric
491 conditions, analytical techniques have fallen out of favor. The height-resolved iono-
492 sphere, the multidimensional Alfvén speed profile, and the inconvenient geometry com-
493 bine to create a problem beyond the reasonable purview of pencil and paper.

494 That is, the topic of field line resonance is ripe for numerical modeling.

495 Past models of the magnetosphere have been ill-suited for the consideration of FLRs.
496 Reasons include overly-simplified treatment of the ionospheric boundary, no consider-
497 ation of the plasmapause, limited range in m , and the inability to compute ground
498 signatures. Chapter 5 presents a model which addresses these issues, allowing the com-
499 putation of field line resonance with unparalleled attention to realism.

500 The model allows a bird’s-eye view of the structure and evolution of FLRs. As such,
501 not only can several open questions be addressed, but their answers serve to unify a
502 number of seemingly-disparate properties described in the sections above.

503 The rotation of poloidally-polarized waves to the toroidal mode is investigated. Par-
504 ticular attention is paid to the importance of azimuthal modenumber and ionospheric
505 conductivity. The interplay between said rotation and the transport of energy across
506 field lines — which also depends on azimuthal modenumber — is considered as well.

507 By their nature, drifting particles have the potential to spur wave-particle interactions
508 at all MLT. However, Pc4 observations are strongly peaked on the dayside. In a 2015
509 paper, Dai notes, “It is not clear why noncompressional [high- m] Pc4 poloidal waves,
510 which are presumably driven by instability within the magnetosphere, preferentially
511 occur on the dayside”[17]. Motoba, later that year, echoes, “It is unclear whether other
512 generation mechanisms of fundamental standing waves ... can explain the localization
513 of Pgs in local time”[71]. This, too, is considered numerically: to what degree is field
514 line resonance affected by the (day-night asymmetric) conditions of the ionosphere?

515 **TODO:** Transition... With the above in mind, what data would be super helpful?

516 It's been shown that a ground magnetometer 66° north of the magnetic equator observes
517 \sim 10 Pg events per year. It's also been shown that poloidal Pc4s are rare compared to
518 toroidal ones, and that most poloidal Pc4s are even harmonics. However, little attention
519 has been paid to how these rates line up with one another. Given the relative occurrence
520 rate of poloidal and toroidal waves, of odd and even harmonics, and of diffuse and sharp
521 spectral peaks, just how unusual are giant pulsations?

522 **Chapter 4**

523 **Waves in Cold Resistive Plasma**

524 Before delving into the implementation of the numerical model, it's instructive to consider the fundamental equations of waves in a cold, resistive plasma.

The evolution of electric and magnetic fields is governed by Ampère's law and Faraday's law. Notably, the present work takes the linearized versions of Maxwell's equations; the vectors \underline{E} and \underline{B} indicate perturbations above the zeroth-order magnetic field.

$$\underline{\epsilon} \cdot \frac{\partial}{\partial t} \underline{E} = \frac{1}{\mu_0} \nabla \times \underline{B} - \underline{J} \quad \frac{\partial}{\partial t} \underline{B} = -\nabla \times \underline{E} \quad (4.1)$$

Current follows Ohm's law. For currents perpendicular to the background magnetic field, Kirchhoff's formulation is sufficient. Conductivity is much higher along the magnetic field lines¹, so it's appropriate to also include the electron inertial term².

$$0 = \underline{\sigma}_{\perp} \cdot \underline{E}_{\perp} - \underline{J}_{\perp} \quad \frac{1}{\nu} \frac{\partial}{\partial t} J_z = \sigma_0 E_z - J_z \quad (4.2)$$

¹The dipole coordinate system is defined rigorously in Section 5.1; at present, it's sufficient to take \hat{z} parallel to the zeroth-order magnetic field, and \hat{x} and \hat{y} perpendicular to \hat{z} (and to each other).

²Electron inertial effects are not included in the model described in Chapter 5, or in the results in Chapter 7; however, their implementation and impact are explored in Chapter 6.

Derivatives in Equations (4.1) and (4.2) can be evaluated by performing a Fourier transform. They can then be combined, eliminating the magnetic field and current terms.

$$\begin{aligned} 0 &= \underline{\underline{E}}_{\perp} + \frac{v_A^2}{\omega^2} (\underline{k} \times \underline{k} \times \underline{E})_{\perp} + \frac{i}{\epsilon_{\perp}\omega} \underline{\sigma}_{\perp} \cdot \underline{\underline{E}}_{\perp} \\ 0 &= E_z + \frac{c^2}{\omega^2} (\underline{k} \times \underline{k} \times \underline{E})_z + \frac{i\omega_P^2}{\omega(\nu - i\omega)} E_z \end{aligned} \quad (4.3)$$

The speed of light, Alfvén speed (including the displacement current correction), plasma frequency, and parallel conductivity are defined in the usual way:

$$c^2 \equiv \frac{1}{\mu_0\epsilon_0} \quad v_A^2 \equiv \frac{1}{\mu_0\epsilon_{\perp}} \quad \omega_P^2 \equiv \frac{ne^2}{m_e\epsilon_0} \quad \sigma_0 \equiv \frac{ne^2}{m_e\nu} \quad (4.4)$$

Using the vector identity $\underline{k} \times \underline{k} \times \underline{E} = \underline{k} \underline{k} \cdot \underline{E} - k^2 \underline{E}$, Equation (4.3) can be reassembled into a single expression,

$$0 = \left(\underline{\underline{\mathbb{I}}} + \frac{1}{\omega^2} \underline{\underline{V}}^2 \cdot \underline{k} \underline{k} - \frac{k^2}{\omega^2} \underline{\underline{V}}^2 + \frac{i}{\omega} \underline{\underline{\Omega}} \right) \cdot \underline{E} \quad (4.5)$$

Where $\underline{\underline{\mathbb{I}}}$ is the identity tensor and in x - y - z coordinates,

$$\underline{\underline{V}}^2 \equiv \begin{bmatrix} v_A^2 & 0 & 0 \\ 0 & v_A^2 & 0 \\ 0 & 0 & c^2 \end{bmatrix} \quad \text{and} \quad \underline{\underline{\Omega}} \equiv \begin{bmatrix} \frac{\sigma_P}{\epsilon_{\perp}} & \frac{-\sigma_H}{\epsilon_{\perp}} & 0 \\ \frac{\sigma_H}{\epsilon_{\perp}} & \frac{\sigma_P}{\epsilon_{\perp}} & 0 \\ 0 & 0 & \frac{\omega_P^2}{(\nu - i\omega)} \end{bmatrix} \quad (4.6)$$

526 In Equation (4.5), the expression in parentheses is the dispersion tensor. Nontrivial
527 solutions exist only when its determinant is zero. This gives rise to a seventh-order
528 polynomial in ω , so rather than a direct solution it's necessary to consider limits of
529 specific interest.

530 Without loss of generality, the wave vector \underline{k} may be taken to lie in the x - z plane — that
531 is, with $k_y = 0$. The distinction between the two perpendicular directions is discussed
532 in Section 4.4.

533 **4.1 Guided Propagation**

534 The wave vector of a field line resonance aligns closely to the background magnetic
535 field. By supposing that the two align exactly (that is, taking $k_x = 0$), the parallel and
536 perpendicular components of the dispersion relation are decoupled.

The parallel-polarized component — that is, the solution when $E_x = E_y = 0$ — is quadratic, and thus can be solved directly.

$$0 = \omega^2 + i\nu\omega - \omega_P^2 \quad \text{so} \quad \omega = -\frac{i\nu}{2} \pm \sqrt{\omega_P^2 - \frac{\nu^2}{4}} \quad (4.7)$$

537 It bears noting that the plasma frequency is large — not just compared to Pc4 frequencies,
538 but even compared to the collision frequencies in the ionosphere³.

Expanding Equation (4.7) with respect to large ω_P , the dispersion relation becomes

$$\omega^2 = \omega_P^2 \pm i\nu\omega_P + \dots \quad (4.8)$$

539 Equation (4.8) can hardly be called a wave, as it does not depend on the wave vector
540 \underline{k} . Rather, it is the plasma oscillation⁴: electrons vibrating in response to a charge
541 separation along the background magnetic field.

542 The plasma oscillation is not specifically relevant to the study of field line resonance.
543 The two phenomena are separated by six orders of magnitude in frequency. The topic
544 is revisited in Chapter 6 insomuch as it is inseparable from the electron inertial effects
545 in Ohm's law.

³The collision frequency may match or exceed the plasma frequency for a thin slice at the bottom of the ionosphere, where the density of neutral atoms is large; however, it falls off quickly. Above an altitude of 200 km, conservatively[74], the plasma frequency exceeds the collision frequency by an order of magnitude or more.

⁴The plasma oscillation is also called the Langmuir wave, after Irving Langmuir.

The perpendicular ($E_z = 0$) components of the dispersion relation give an expression quartic in ω .

$$0 = \omega^4 + 2i\frac{\sigma_P}{\epsilon_\perp}\omega^3 - \left(2k_z^2v_A^2 + \frac{\sigma_P^2 + \sigma_H^2}{\epsilon_\perp^2}\right)\omega^2 - 2ik_z^2v_A^2\frac{\sigma_P}{\epsilon_\perp}\omega + k_z^4v_A^4 \quad (4.9)$$

Like the parallel-polarized component above, Equation (4.9) can be solved directly. Noting that \pm and \oplus are independent,

$$\omega = \left(\frac{\pm\sigma_H - i\sigma_P}{2\epsilon_\perp}\right) \oplus \sqrt{k_z^2v_A^2 + \left(\frac{\pm\sigma_H - i\sigma_P}{2\epsilon_\perp}\right)^2} \quad (4.10)$$

Also like the parallel-polarized component, the exact solution is less useful than its Taylor expansion. The Pedersen and Hall conductivities are large near the ionospheric boundary, but fall off quickly; for the vast majority of the field line, the ratios $\frac{\sigma_P}{\epsilon_\perp}$ and $\frac{\sigma_H}{\epsilon_\perp}$ are small compared to field line resonance frequencies. Expanding with respect to small conductivity gives

$$\omega^2 = k_z^2v_A^2 \oplus k_zv_A\frac{\sigma_H \pm i\sigma_P}{\epsilon_\perp} + \dots \quad (4.11)$$

546 This is the shear Alfvén wave, with a shift to its frequency due to the conductivity of
 547 the ionosphere. It travels along the background magnetic field like a bead on a string,
 548 with electric and magnetic field perturbations perpendicular to the magnetic field line
 549 (and to one another).

550 4.2 Compressional Propagation

551 The partner to guided motion is compressional motion; in order for energy to move
 552 across field lines, the wave vector must have a component perpendicular to \hat{z} . If the
 553 wave vector is completely perpendicular to the magnetic field line ($k_z = 0$), the parallel
 554 and perpendicular components of the dispersion relation decouple, as in Section 4.1.

The parallel-polarized ($E_x = E_y = 0$) component of the dispersion relation is

$$0 = \omega^3 + i\nu\omega^2 - (k_x^2 c^2 + \omega_P^2) \omega - ik_x^2 c^2 \nu \quad (4.12)$$

Equation (4.12) can be solved directly, though its solution (as a cubic) is far too long to be useful. Expanding with respect to the large plasma frequency, gives

$$\omega^2 = k^2 c^2 + \omega_P^2 - i\nu\omega_P + \dots \quad (4.13)$$

555 This is the O mode, a compressional wave with an electric field perturbation along
 556 the background magnetic field. Like the plasma oscillation discussed in Section 4.1, its
 557 frequency is very large compared to that of a field line resonance.

The perpendicular-polarized ($E_z = 0$) component of the compressional dispersion relation is also cubic.

$$0 = \omega^3 + 2i\frac{\sigma_P}{\epsilon_\perp}\omega^2 - \left(2k_x^2 v_A^2 + \frac{\sigma_P^2 + \sigma_H^2}{\epsilon_\perp^2}\right) \omega - ik_x^2 v_A^2 \frac{\sigma_P}{\epsilon_\perp} \quad (4.14)$$

A wave moving across magnetic field lines near the ionospheric boundary will encounter large $\frac{\sigma_P}{\epsilon_\perp}$ and $\frac{\sigma_H}{\epsilon_\perp}$, while at moderate to high altitudes those ratios will be small. Solving Equation (4.14) in those two limits respectively gives:

$$\omega^2 = k_x^2 v_A^2 \pm ik_x v_A \frac{\sigma_P}{\epsilon_\perp} + \dots \quad \text{and} \quad \omega^2 = k_x^2 v_A^2 + \left(\frac{\sigma_H \pm i\sigma_P}{\epsilon_\perp}\right)^2 + \dots \quad (4.15)$$

558 In both limits, Equation (4.15) describes a compressional Alfvén wave. The magnetic
 559 field perturbation is along the background magnetic field — indicating compression of
 560 the frozen-in plasma — while the electric field perturbation is perpendicular to both
 561 the magnetic field and the wave vector.

562 **TODO: Double check terminology. Jesse's dissertation disagrees with Bob's notes.**

563 4.3 High Altitude Limit

564 In the limit of large radial distance, it's reasonable to take the collision frequency to
 565 zero; doing so also neglects the Pedersen and Hall conductivities.

Whereas in Sections 4.1 and 4.2 it was the parallel-polarized component of the dispersion relation that factored out from the other two, the high altitude limit decouples the component polarized out of the x - z plane. The y -polarized dispersion ($E_x = E_z = 0$) is simply:

$$\omega^2 = k^2 v_A^2 \quad (4.16)$$

566 Equation (4.16) describes an Alfvén wave with an arbitrary angle of propagation. De-
 567 pending on the angle between the wave vector and the background magnetic field, it
 568 could be guided, compressional, or somewhere in between. Regardless of propagation
 569 angle, the electric field perturbation is perpendicular to both the direction of propaga-
 570 tion and the magnetic field perturbation.

The other two components (from $E_y = 0$) of the high altitude dispersion tensor give an expression quadratic in ω^2 :

$$0 = \omega^4 - (k_x^2 c^2 + k_z^2 v_A^2 + \omega_P^2) \omega^2 + k_z^2 v_A^2 \omega_P^2 \quad (4.17)$$

Which can be solved for

$$\omega^2 = \frac{1}{2} (k_x^2 c^2 + k_z^2 v_A^2 + \omega_P^2) \pm \sqrt{\frac{1}{4} (k_x^2 c^2 + k_z^2 v_A^2 + \omega_P^2)^2 - k_z^2 v_A^2 \omega_P^2} \quad (4.18)$$

Noting again that ω_P is very large, the two roots can be expanded to

$$\omega^2 = k_z^2 v_A^2 \left(1 + \frac{k_x^2 c^2 + k_z^2 v_A^2}{\omega_P^2} \right) + \dots \quad \text{and} \quad \omega^2 = k_x^2 c^2 + k_z^2 v_A^2 + \omega_P^2 + \dots \quad (4.19)$$

571 The first is a shear Alfvén wave, as in Equation (4.11). The second oscillates faster than
 572 the plasma frequency; like the plasma oscillation in Equation (4.8) and the O mode in
 573 Equation (4.13), it's far outside the Pc4 frequency range.

574 4.4 Implications to the Present Work

575 The present section's findings carry three significant implications for the present work.
 576 First — with the exception of the plasma oscillation and similar modes, which are
 577 revisited in Chapter 6 — waves propagate at the Alfvén speed. This, in combination
 578 with the grid configuration, will constrain the time step that can be used to model them
 579 numerically. The time step must be sufficiently small that information traveling at the
 580 Alfvén speed cannot “skip over” entire grid cells⁵.

Second, the results of the present section allow an estimate of the magnitude of parallel electric field that might be expected from a field line resonance compared to its perpendicular electric field. Between the full dispersion tensor form in Equation (4.5) and the Alfvén wave described by Equation (4.19),

$$\left| \frac{E_z}{E_x} \right| = \frac{k_x k_z c^2}{\omega^2 - k_x^2 c^2 - \omega_P^2} \sim \frac{k^2 c^2}{\omega_P^2} \quad (4.20)$$

581 In essence, the relative magnitudes of the parallel and perpendicular electric fields should
 582 be in proportion to the square of the relative magnitudes of the electron inertial length
 583 (1 km to 100 km) and the wavelength ($\sim 10^5$ km). That is, parallel electric fields should
 584 be smaller than the perpendicular electric fields by six or more orders of magnitude.
 585 Finally, the dispersion relations shown above indicate how the behavior of a field line
 586 resonance should behave as the azimuthal modenumber becomes large.
 587 Whereas the shear Alfvén wave's dispersion relation depends only on the parallel com-
 588 ponent of the wave vector, the compressional Alfvén wave depends on its magnitude:
 589 $\omega^2 = k^2 v_A^2$. If the frequency is smaller than $k v_A$, the wave will become evanescent. The

⁵As is the convention, the time step is scaled down from the smallest Alfvén zone crossing time by a Courant factor, typically 0.1, meaning that it takes at least ten time steps to cross a grid cell.

590 wave vector's magnitude can be no smaller than its smallest component, however, and
 591 the azimuthal component scales with the azimuthal modenumber: $k_y \sim \frac{m}{2\pi r}$.

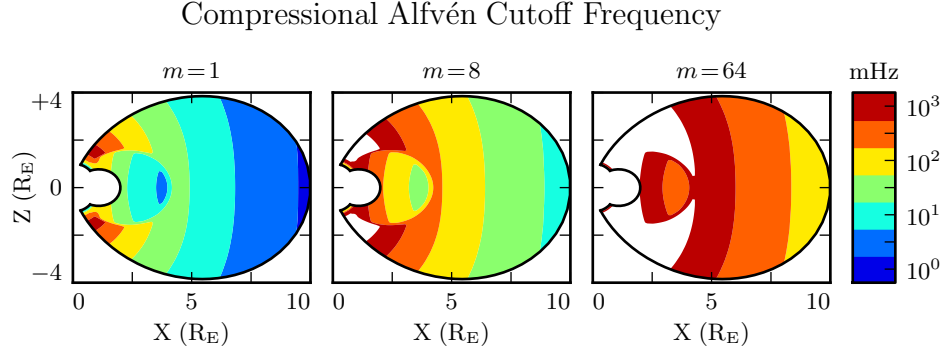


Figure 4.1: Taking $k_y \sim \frac{m}{2\pi r}$ as a lower bound for the magnitude of the wave vector, the above figure demonstrates the lowest frequency at which compressional Alfvén waves may propagate as a function of position and m . Regions shown in white are off the color scale — they have a lower bound on the order of 10^4 mHz or more. The above Alfvén frequency profile is from Kelley[49], for quiet dayside conditions, as discussed in Section 5.2.

592 This imposes a frequency cutoff on compressional Alfvén waves which scales with the
 593 azimuthal modenumber, as shown in Figure 4.1. At small values of m , most of the mag-
 594 netosphere is conducive to compressional Alfvén waves in the Pc4 frequency range. As
 595 m increases, and the wave vector with it, the inner magnetosphere becomes increasingly
 596 inaccessible to them.

597 **Chapter 5**

598 **“Tuna Half” Dimensional Model**

599 The present section describes the implementation of Tuna, a new two and a half dimensional
600 Alfvén wave code based largely on work by Lysak[59, 62].

601 The half-integer dimensionality refers to the fact that Tuna’s spatial grid resolves a
602 two-dimensional slice of the magnetosphere, but that electric and magnetic fields —
603 as well as their curls — are three-dimensional vectors. This apparent contradiction is
604 reconciled by the use of a fixed azimuthal modenumber, m . Electric and magnetic fields
605 are taken to be complex-valued, varying azimuthally per $\exp(im\phi)$; derivatives with
606 respect to ϕ are then replaced by a factor of im .

607 Unlike a fully three-dimensional code, Tuna cannot resolve the evolution of wave structures
608 in the azimuthal direction. Furthermore, the model does not allow coupling between
609 the dayside and nightside magnetospheres. What Tuna does offer is efficiency.
610 The model’s economical geometry allows it to include a realistic Earthward boundary:
611 grid spacing on the order of 10 km, a height-resolved ionospheric conductivity tensor,
612 and even the computation of magnetic field signatures at the ground. Such features are
613 computationally infeasible for a large global code.

614 Tuna was developed with field line resonance in mind. As discussed in Chapter 3,
615 such waves are azimuthally localized, minimizing the importance of Tuna’s missing half
616 dimension. Moreover, because field line resonances are known to be affected by both

617 the ionosphere and the plasmasphere, a faithful treatment of the inner magnetosphere
618 is a crucial part of studying them numerically.

619 Perhaps the most exciting feature of Tuna is its novel driving mechanism: ring current
620 perturbation. Codes similar to Tuna have traditionally been driven using compressional
621 pulses at the outer boundary[59, 62, 101, 102]. This has precluded the investigation of
622 waves with large azimuthal modenumber — such as giant pulsations — which are guided,
623 and thus must be driven from within the magnetosphere.

624 TODO: The dipole geometry isn't super new, but it's not widely used. The height-
625 resolved ionosphere is new and exciting! Ground signatures are new and exciting!

626 TODO: The support software — the driver and the plotter — are also significant. Do
627 they get mentioned here? Does the Git repository where the code can be accessed get
628 mentioned here?

629 5.1 Coordinate System

Field line resonance has traditionally been modeled by straightening the field lines into a rectangular configuration[22, 65], by unrolling the azimuthal coordinate into a cylindrical coordinate system[79], or through the use of dipole coordinates[78]¹:

$$x \equiv -\frac{\sin^2 \theta}{r} \quad y \equiv \phi \quad z \equiv \frac{\cos \theta}{r^2} \quad (5.1)$$

630 Where r , θ , and ϕ take on their usual spherical meanings of radial distance, colatitude,
631 and azimuthal angle respectively.

632 The dipole coordinate x is constant over each equipotential shell², y is azimuthal angle,
633 and z indexes each field line from south to north. The unit vectors \hat{x} , \hat{y} , and \hat{z} point

¹The dipole coordinates x , y and z are perhaps more commonly named μ , ϕ , and ν respectively; however, in the present work, μ and ν take other meanings.

²In fact, x is inversely proportional to the McIlwain parameter L .

634 in the crosswise³ (radially outward at the equator), azimuthal (eastward), and parallel
 635 (northward at the equator) directions respectively.

Notably, the dipole coordinates in Equation (5.1) are normal to one another. While mathematically convenient, they do not readily accommodate a fixed-altitude boundary at the ionosphere, nor do they allow the dipole magnetic field to intersect the boundary at an oblique angle, as Earth's field does. As a solution, a nonorthogonal set of dipole coordinates was developed numerically by Proehl[77], then formalized analytically by Lysak[59] in terms of their contravariant components:

$$u^1 = -\frac{R_I}{r} \sin^2 \theta \quad u^2 = \phi \quad u^3 = \frac{R_I^2}{r^2} \frac{\cos \theta}{\cos \theta_0} \quad (5.2)$$

636 Above, R_I is the position of the ionosphere relative to Earth's center; it's typically taken
 637 to be $1 R_E + 100 \text{ km}$.

638 Like the dipole coordinates x , y , and z , Lysak's coordinates u^1 , u^2 , and u^3 correspond to
 639 L -shell, azimuthal angle, and position along a field line respectively. However, compared
 640 to z , u^3 has been renormalized using the invariant colatitude⁴ θ_0 . As a result, u^3 takes
 641 the value $+1$ at the northern ionospheric boundary and -1 at the southern ionospheric
 642 boundary for all field lines.

Because Lysak's coordinate system is not orthogonal⁵, it's necessary to consider covariant and contravariant basis vectors separately.

$$\hat{e}_i \equiv \frac{\partial}{\partial u^i} \underline{x} \quad \hat{e}^i \equiv \frac{\partial}{\partial \underline{x}} u^i \quad (5.3)$$

Covariant basis vectors \hat{e}_i are normal to the curve defined by constant u^i , while contravariant basis vectors \hat{e}^i are tangent to the coordinate curve (equivalently, \hat{e}^i is normal

³In the context of in situ measurements taken near the equatorial plane, \hat{x} is referred to as the radial direction; however, the present work extends the dipole grid to low altitudes, where \hat{x} can be more horizontal than vertical. The term "crosswise" is meant to indicate that \hat{x} is defined by the cross product of \hat{y} and \hat{z} .

⁴The invariant colatitude is the colatitude θ at which a field line intersects the ionosphere. It is related to the McIlwain parameter by $\cos \theta_0 \equiv \sqrt{1 - \frac{R_I}{L}}$.

⁵Curves of constant u^1 and curves of constant u^3 can intersect at non-right angles.

to the plane defined by constant u^j for all $j \neq i$). These vectors are reciprocal⁶ to one another, and can be combined to give components of the metric tensor $\underline{\underline{g}}$ [20].

$$\hat{e}^i \cdot \hat{e}_j = \delta_j^i \quad g_{ij} \equiv \hat{e}_i \cdot \hat{e}_j \quad g^{ij} \equiv \hat{e}^i \cdot \hat{e}^j \quad (5.4)$$

The metric tensor allows rotation between covariant and contravariant representations of vectors.

$$A_i = g_{ij} A^j \quad \text{and} \quad A^i = g^{ij} A_j \quad \text{where} \quad A_i \equiv \underline{A} \cdot \hat{e}_i \quad \text{and} \quad A^i \equiv \underline{A} \cdot \hat{e}^i \quad (5.5)$$

In addition, the determinant of the metric tensor is used to define cross products and curls⁷.

$$(\underline{A} \times \underline{B})^i = \frac{\varepsilon^{ijk}}{\sqrt{g}} A_j B_k \quad \text{and} \quad (\nabla \times \underline{A})^i = \frac{\varepsilon^{ijk}}{\sqrt{g}} \frac{\partial}{\partial u^j} A_k \quad \text{where} \quad g \equiv \det \underline{\underline{g}} \quad (5.6)$$

Explicit forms of the basis vectors and metric tensor can be found in the appendix of Lysak's 2004 paper[59]. At present, it's sufficient to note the mapping between Lysak's basis vectors and the usual dipole unit vectors.

$$\hat{x} = \frac{1}{\sqrt{g^{11}}} \hat{e}^1 \quad \hat{y} = \frac{1}{\sqrt{g^{22}}} \hat{e}^2 \quad \hat{z} = \frac{1}{\sqrt{g^{33}}} \hat{e}^3 \quad (5.7)$$

⁶⁴³ TODO: Do these need to be written out? Referring people to the code, which will be in a public Git repository, is also a possibility.

The basis vectors can also be mapped to the spherical unit vectors, though Equation (5.8) is valid only at the ionospheric boundary.

$$\hat{\theta} = \frac{1}{\sqrt{g_{11}}} \hat{e}_1 \quad \hat{\phi} = \frac{1}{\sqrt{g_{22}}} \hat{e}_2 \quad \hat{r} = \frac{1}{\sqrt{g_{33}}} \hat{e}_3 \quad (5.8)$$

⁶The symbol δ_j^i is the Kronecker delta; the present work also makes use of the Levi-Civita symbol ε^{ijk} and Einstein's convention of implied summation over repeated indeces[24].

⁷The square root of the determinant of the metric tensor is called the Jacobian. It's sometimes denoted using the letter J , which is reserved for current in the present work.

645 The coordinates converge at the equatorial ionosphere, so an inner boundary is necessary
646 to maintain finite grid spacing. It's typically placed at $L = 2$. The outer boundary is
647 at $L = 10$. The dipole approximation of Earth's magnetic field is tenuous at the outer
648 boundary (particularly on the dayside); however, in practice, wave activity is localized
649 inside $L \sim 7$. The grid is spaced uniformly in u^1 , which gives finer resolution close to
650 Earth and coarser resolution at large distances.

651 Spacing in u^3 is set by placing grid points along the outermost field line. The points are
652 closest together at the ionosphere, and grow towards the equator. The spacing increases
653 in a geometric fashion, typically by 3%.

654 Typically, Tuna uses a grid 150 points in u^1 by 350 points in u^3 . The result is a resolution
655 on the order of 10 km at the ionosphere, which increases to the order of 10³ km at the
656 midpoint of the outermost field line.

657 There are no grid points in u^2 due to the two-and-a-half-dimensional nature of the
658 model. Fields are assumed to vary as $\exp(imu^2)$ — equally, $\exp(im\phi)$ — so derivatives
659 with respect to u^2 are equivalent to a factor of im . In effect, the real component of
660 each field is azimuthally in phase with the (purely real) driving, while imaginary values
661 represent behavior that is azimuthally offset.

662 The simulation's time step is set based on the grid spacing. As is the convention, δt is
663 set to match the smallest Alfvén zone crossing time, scaled down by a Courant factor
664 (typically 0.1). It bears noting that the smallest crossing time need not correspond to
665 the smallest zone; the Alfvén speed peaks several thousand kilometers above Earth's
666 surface, in the so-called Ionospheric Alfvén Resonator[62]. A typical time step is on the
667 order of 10⁻⁵ s.

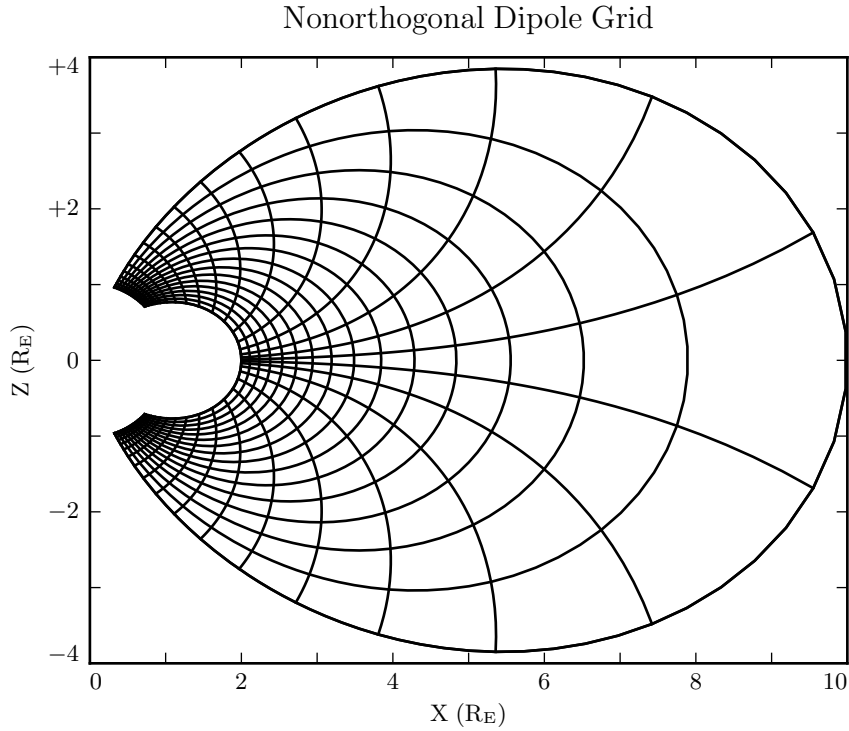


Figure 5.1: The model’s nonorthogonal dipole grid. Every fifth point is shown in each direction. The high concentration of grid points near Earth’s equator is a consequence of the coordinate system, which converges at the equatorial ionosphere. Earth (not shown) is centered at the origin with unit radius.

668 5.2 Physical Parameter Profiles

Tuna models Earth’s magnetic field to be an ideal dipole, so the zeroth-order field strength is written in the usual form:

$$\underline{B}_0 = 3.1 \times 10^4 \text{ nT} \left(\frac{R_E}{r} \right)^3 \left(2 \cos \theta \hat{r} - \sin \theta \hat{\theta} \right) \quad (5.9)$$

Number density is taken to be the sum of an inverse-radial-dependent auroral profile and a plasmaspheric profile dependent on the L -shell[62]:

$$n = n_{AZ} \frac{r_{AZ}}{r} + n_{PS} \exp\left(\frac{-L}{L_{PS}}\right) \left(\frac{1}{2} - \frac{1}{2} \tanh \frac{L - L_{PP}}{\delta L_{PP}} \right) \quad (5.10)$$

669 Where typical values are shown in Table 5.1.

Table 5.1: Typical Parameters for the Tuna Density Profile

Variable	Value	Description
L_{PS}	1.1	Scale L of the plasmasphere.
L_{PP}	4.0	Location of the plasmapause.
δL_{PP}	0.1	Thickness of the plasmapause.
n_{AZ}	$10 / \text{cm}^3$	Number density at the base of the auroral zone.
n_{PS}	$10^4 / \text{cm}^3$	Number density at the base of the plasmasphere.
r_{AZ}	1 R_E	Scale height of the auroral density distribution.

The perpendicular component of the electric tensor, ϵ_{\perp} , is computed based on Kelley's[49] tabulated low-density values, ϵ_K , which are adjusted to take into account the effects of high density in the plasmapause.

$$\epsilon_{\perp} = \epsilon_K + \frac{Mn}{B_0^2} \quad (5.11)$$

670 Where M is the mean molecular mass, which is large ($\sim 28 \text{ u}$) at 100 km altitude, then
671 drops quickly (down to 1 u by $\sim 1000 \text{ km}$)[62].

672 The Alfvén speed profile is computed from the perpendicular electric constant in the
673 usual way, $v_A^2 \equiv \frac{1}{\mu_0 \epsilon_{\perp}}$. This form takes into account the effect of the displacement
674 current, which becomes important in regions where the Alfvén speed approaches the
675 speed of light.

676 While the density profile is held constant for all runs discussed in the present work,
677 the Alfvén speed profile is not. Four different profiles are used for the low-density

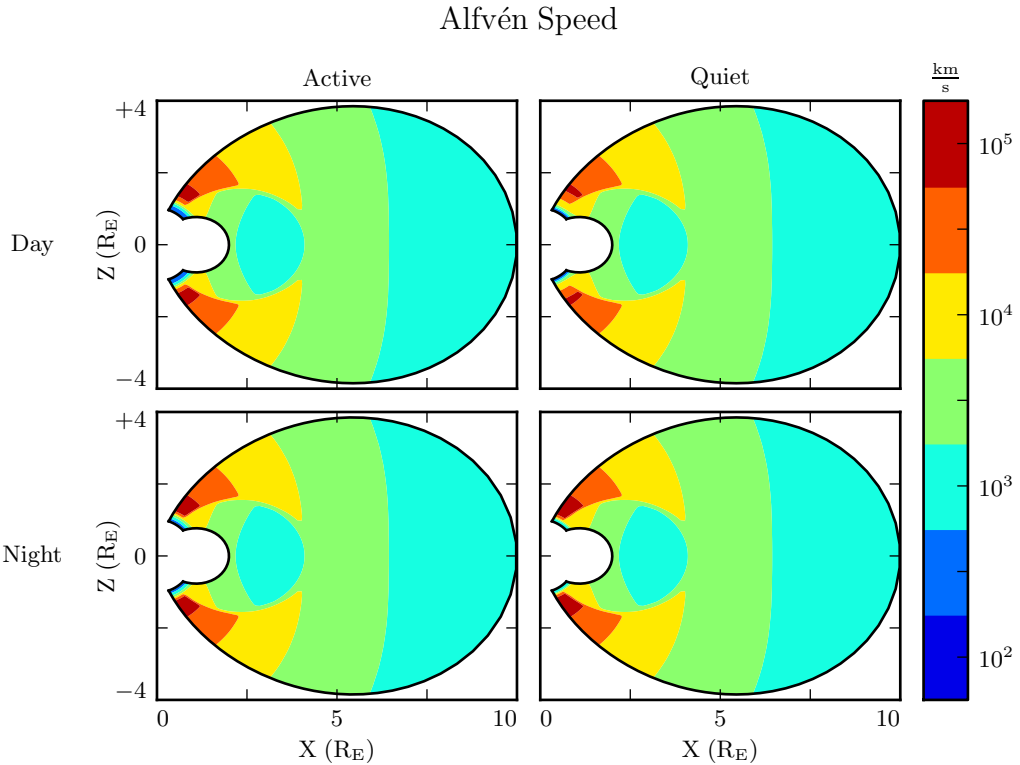


Figure 5.2: Alfvén speed profiles are based on low-density values tabulated by Kelley[49]. They are adjusted to take into account the density of the plasmapause and mass loading near the Earthward boundary.

678 perpendicular electric constant ϵ_K , corresponding to the differing ionospheric conditions
 679 between the dayside and the nightside, and between the high and low points in the
 680 solar cycle. These differences are visible in Figure 5.2, particularly in the size of the
 681 ionospheric Alfvén resonator (the peak in Alfvén speed in the high-latitude ionosphere).

682 **TODO:** Runs are only carried out for day and night... is it even worth showing the
 683 flank profile?

684 Ionospheric conductivity profiles are also based on values tabulated by Kelley, adjusted
 685 by Lysak[62] to take into account the abundance of heavy ions near the Earthward
 686 boundary. Pedersen, Hall, and parallel conductivities are each resolved by altitude, as
 687 shown in Figure 5.3.

Pedersen (Blue), Hall (Red), and Parallel (Green) Conductivities

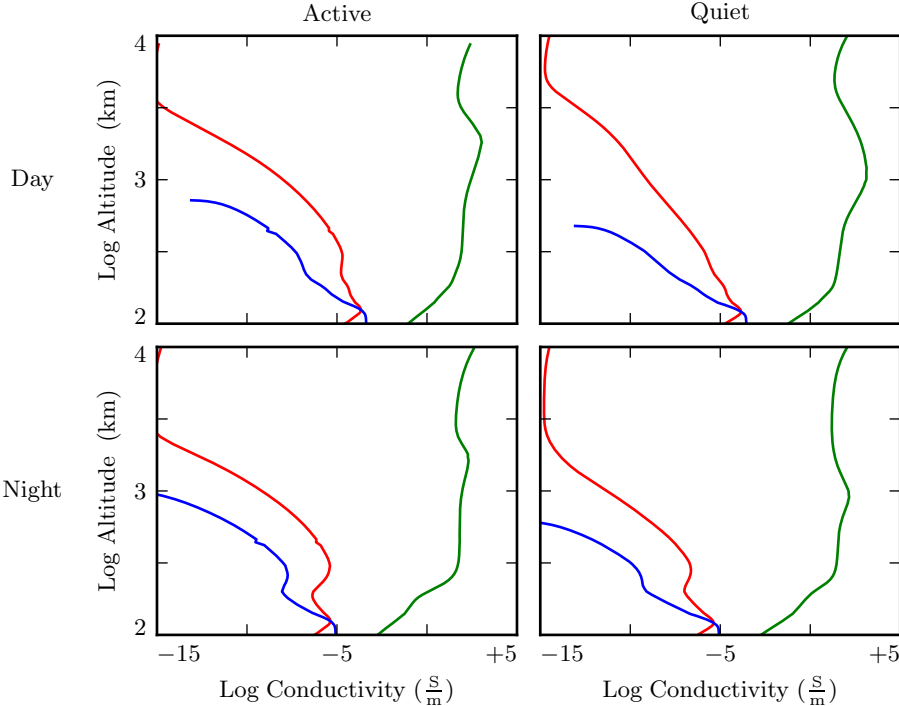


Figure 5.3: Ionospheric conductivity profiles are adapted by Lysak[62] from Kelley's tabulated values[49]. These profiles allow Tuna to simulate magnetosphere-ionosphere coupling under a variety of conditions.

688 Tuna's physical parameter profiles are static over the course of each run. Even so-called
 689 ultra low frequency waves like Pc4 pulsations are fast compared to convective timescales
 690 in the magnetosphere.

691 5.3 Driving

692 Models similar to Tuna have traditionally been driven using compression at the outer
 693 boundary[59, 62, 101, 102]. Such driving acts as a proxy for solar wind compression,
 694 Kelvin-Helmholtz effects at the magnetopause, and so on. However, because of the

695 constraints imposed by the dispersion relation for Alfvén waves⁸, simulations driven from
696 the outer boundary are constrained to the consideration of waves with low azimuthal
697 modenumber (equivalently, large azimuthal wavelength).

698 This issue is demonstrated in Figure 5.4. At low modenumber, energy delivered at
699 the outer boundary propagates across field lines in order to stimulate resonances in
700 the inner magnetosphere. However, as modenumber increases, Alfvén waves become
701 increasingly guided, and the inner magnetosphere is unaffected by perturbations at the
702 outer boundary.

703 In order to simulate high-modenumber Alfvén waves in the inner magnetosphere — such
704 as giant pulsations — a new driving mechanism is necessary. Perturbation of the ring
705 current is a natural choice, as Alfvén waves in the Pc4 range are known to interact with
706 ring current particles through drift and drift-bounce resonances. The ring current is a
707 dynamic region, particularly during and after geomagnetic storms; it's easy to imagine
708 the formation of localized inhomogeneities.

709 In order to estimate an appropriate magnitude for perturbations of the ring current,
710 the Sym-H storm index is used. The index is measured once per minute, and so cannot
711 directly detect ring current modulations in the Pc4 frequency range. Instead, the index
712 is transformed into the frequency domain, allowing a fit of its pink noise⁹.

713 **TODO:** Sym-H is basically the same as Dst[100].

714 As shown in Figure 5.5, a Fourier transform of the Sym-H index (taken here from the
715 June 2013 storm) suggests that magnetic field perturbations at Earth's surface due to
716 ring current activity in the Pc4 frequency range could be up to the order of 10^{-2} nT.
717 Supposing that the ring current is centered around $5 R_E$ geocentric, that corresponds to
718 a current on the order of 0.1 MA. Tuna's driving is spread using a Gaussian profile in
719 u^1 (typically centered at $L = 5$) and u^3 (typically centered just off the equator), with a
720 characteristic area of $1 R_E^2$; this gives a current density on the order of $10^{-4} \mu\text{A}/\text{m}^2$.

⁸See Section 4.4.

⁹Pink noise, also called $\frac{1}{f}$ noise, refers to the power law decay present in the Fourier transforms of all manner of physical signals.

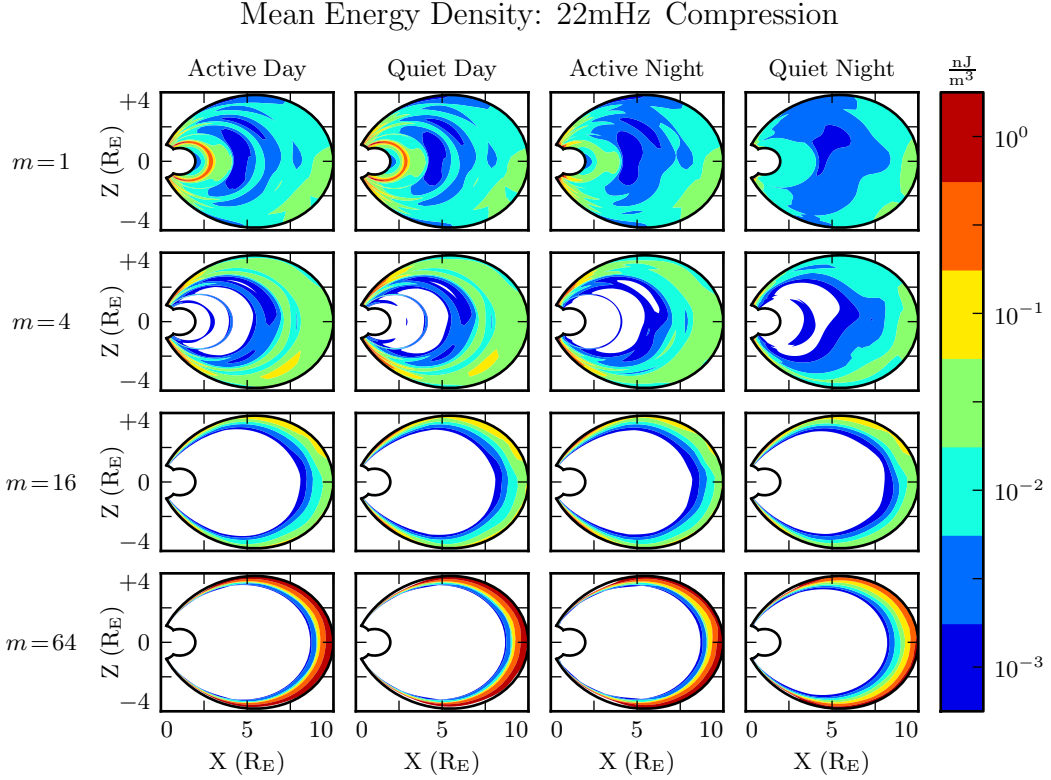


Figure 5.4: Each cell presents the mean energy density over the course of a 300 s run, as a function of position, due to compressional driving at the outer boundary. Azimuthal modenumber varies by row, and ionospheric conditions vary by column. For runs with small azimuthal modenumber, it's clear that energy is able to propagate across field lines and stimulate wave activity in the inner magnetosphere. When the modenumber is large, energy is unable to penetrate to the inner magnetosphere. Notably, the large values on the bottom row should be taken with a grain of salt; it's not clear that the model's results are reliable when waves are continuously forced against the boundary.

- 721 TODO: Admittedly, estimating the strength of localized perturbations using Sym-H —
 722 an index averaged over the entire globe — is a bit of a kludge.
- 723 In situ observations of Pc4 pulsations and giant pulsations have shown waves with
 724 modenumbers across the range $1 \lesssim m \lesssim 100$ [17, 18, 91]. Simulations are carried out
 725 across that range, corresponding to ring current perturbations with azimuthal extent as
 726 small as $0.5 R_E$.

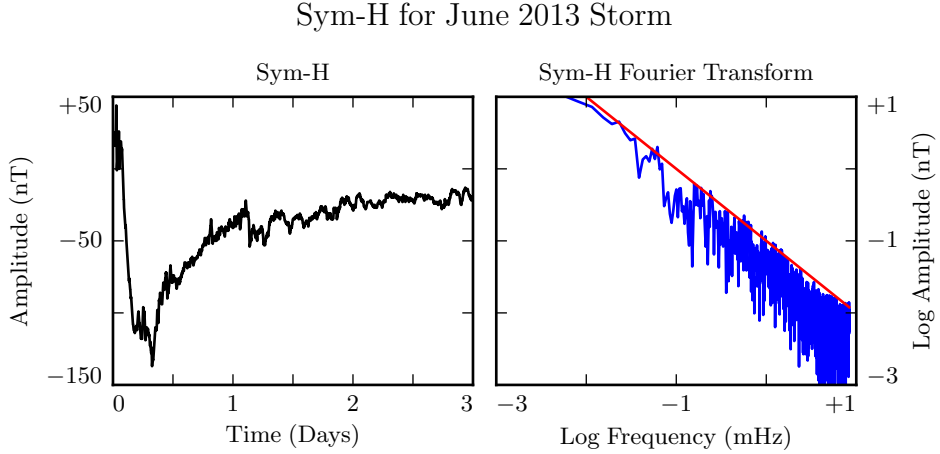


Figure 5.5: The Sym-H storm index[72] measures magnetic perturbations on Earth’s surface due to ring current activity. The amplitude of oscillations in the Pc4 range is estimated by fitting the pink noise in its Fourier transform.

727 TODO: Driving is delivered in the azimuthal component of the current only.

728 TODO: Driving is sinusoidal.

729 TODO: In case it’s not clear: Chapter 7 discusses ONLY simulations using ring current driving. The only compressional driving we look at is Figure 5.4.

731 5.4 Maxwell’s Equations

732 Tuna simulates the evolution of electromagnetic waves in accordance with Ampère’s
733 law and Faraday’s law. Computation is carried out on a Yee grid[106]: electric fields
734 and magnetic fields are offset by half a time step, and each field component is defined
735 on either odd or even grid points in each dimension to ensure that curls are computed
736 using centered differences.

The Ohmic current in Ampère’s law is replaced with $\underline{\sigma} \cdot \underline{E}$ per Kirchhoff’s formulation of Ohm’s law. Then, taking \underline{J} to represent the driving current discussed in Section 5.3,

Maxwell's equations can be written

$$\frac{\partial}{\partial t} \underline{B} = -\nabla \times \underline{E} \quad \underline{\epsilon} \cdot \frac{\partial}{\partial t} \underline{E} = \frac{1}{\mu_0} \nabla \times \underline{B} - \underline{J} - \underline{\sigma} \cdot \underline{E} \quad (5.12)$$

It is convenient to introduce shorthand for the curl of each field: $\underline{C} \equiv \nabla \times \underline{E}$ and $\underline{F} \equiv \nabla \times \underline{B} - \mu_0 \underline{J}$. Or, recalling Equation (5.6),

$$C^i = \frac{\varepsilon^{ijk}}{\sqrt{g}} \frac{\partial}{\partial u^j} E_k \quad F^i = \frac{\varepsilon^{ijk}}{\sqrt{g}} \frac{\partial}{\partial u^j} B_k - J^i \quad (5.13)$$

In these terms, Faraday's law can simply be written:

$$\frac{\partial}{\partial t} B^i = -C^i \quad (5.14)$$

Writing each component out explicitly, and using the metric tensor (per Equation (5.5)) to eliminate contravariant magnetic field components¹⁰, Equation (5.14) becomes:

$$\begin{aligned} B_1 &\leftarrow B_1 - g_{11} \delta t C^1 - g_{13} \delta t C^3 \\ B_2 &\leftarrow B_2 - g_{22} \delta t C^2 \\ B_3 &\leftarrow B_3 - g_{31} \delta t C^1 - g_{33} \delta t C^3 \end{aligned} \quad (5.15)$$

⁷³⁷ Note that the \leftarrow operator is used in Equation (5.15) to indicate assignment, rather than equality. Terms on the left are new, while those on the right are old.

Unlike Faraday's law, Ampère's law cannot be trivially solved. Not only does the derivative of \underline{E} depend on its own future value, but the crosswise and azimuthal components of the equation are coupled by the Hall terms in the conductivity tensor. Fortunately,

¹⁰Fields are stored only in terms of their covariant components, and curls in terms of their contravariant components. This reduces Tuna's memory footprint (since each field need not be stored twice) as well as its computational cost (since time need not be spent rotating between bases). As a result, Tuna's solutions to Maxwell's equations are linear expressions whose coefficients are a mishmash of physical constants and geometric factors. To save time, each coefficient is computed once and stored, rather than being multiplied out from scratch with each time step.

the electric tensor can be inverted, allowing a solution by integrating factors:

$$\underline{\epsilon} \cdot \frac{\partial}{\partial t} \underline{E} = \frac{1}{\mu_0} \underline{F} - \underline{\sigma} \cdot \underline{E} \quad \text{becomes} \quad \left(\underline{\Omega} + \underline{\mathbb{I}} \frac{\partial}{\partial t} \right) \cdot \underline{E} = \underline{V}^2 \cdot \underline{F} \quad (5.16)$$

Where $\underline{\mathbb{I}}$ is the identity tensor and in x - y - z coordinates¹¹,

$$\underline{V}^2 \equiv \frac{1}{\mu_0} \underline{\epsilon}^{-1} = \begin{bmatrix} v_A^2 & 0 & 0 \\ 0 & v_A^2 & 0 \\ 0 & 0 & c^2 \end{bmatrix} \quad \text{and} \quad \underline{\Omega} \equiv \underline{\epsilon}^{-1} \cdot \underline{\sigma} = \begin{bmatrix} \frac{\sigma_P}{\epsilon_{\perp}} & \frac{-\sigma_H}{\epsilon_{\perp}} & 0 \\ \frac{\sigma_H}{\epsilon_{\perp}} & \frac{\sigma_P}{\epsilon_{\perp}} & 0 \\ 0 & 0 & \frac{\sigma_0}{\epsilon_0} \end{bmatrix} \quad (5.17)$$

Multiplying through by $\exp(\underline{\Omega} t)$ and applying the product rule, Equation (5.16) becomes¹²

$$\frac{\partial}{\partial t} \left(\exp(\underline{\Omega} t) \cdot \underline{E} \right) = \exp(\underline{\Omega} t) \cdot \underline{V}^2 \cdot \underline{F} \quad (5.18)$$

Equation (5.18) can then be integrated over a small time step δt and expressed in terms of the assignment operator introduced in Equation (5.15).

$$\underline{E} \leftarrow \exp(-\underline{\Omega} \delta t) \cdot \underline{E} + \delta t \exp(-\underline{\Omega} \frac{\delta t}{2}) \cdot \underline{V}^2 \cdot \underline{F} \quad (5.19)$$

The tensor exponential can be evaluated by splitting $\underline{\Omega}$ into the sum of its diagonal and Hall components¹³. The Hall exponential condenses into sines and cosines, giving a rotation around the magnetic field line:

$$\underline{E} \leftarrow \exp(-\underline{\Omega}' \delta t) \cdot \underline{R}_z \left(\frac{-\sigma_H \delta t}{\epsilon_{\perp}} \right) \cdot \underline{E} + \delta t \underline{V}^2 \cdot \exp(-\underline{\Omega}' \frac{\delta t}{2}) \cdot \underline{R}_z \left(\frac{-\sigma_H \delta t}{2\epsilon_{\perp}} \right) \cdot \underline{F} \quad (5.20)$$

¹¹Note the parallel component of the present definition of $\underline{\Omega}$ differs slightly from that used in Chapter 4, due to the present neglect of inertial effects; see Chapter 6.

¹²Tensor exponentiation is analogous to scalar exponentiation[38]: $\exp(\underline{T}) \equiv \sum_n \frac{1}{n!} \underline{T}^n$.

¹³For tensors, $\exp(\underline{S} + \underline{T}) = \exp(\underline{S}) \exp(\underline{T})$ as long as $\underline{S} \cdot \underline{T} = \underline{T} \cdot \underline{S}$.

Where

$$\underline{\underline{R}}_z(\theta) = \begin{bmatrix} \cos \theta & -\sin \theta & 0 \\ \sin \theta & \cos \theta & 0 \\ 0 & 0 & 1 \end{bmatrix} \quad \text{and} \quad \underline{\underline{\Omega}}' \equiv \begin{bmatrix} \frac{\sigma_P}{\epsilon_{\perp}} & 0 & 0 \\ 0 & \frac{\sigma_P}{\epsilon_{\perp}} & 0 \\ 0 & 0 & \frac{\sigma_0}{\epsilon_0} \end{bmatrix} \quad (5.21)$$

The parallel component of term of Equation (5.20) is simply

$$E_z \leftarrow E_z \exp\left(\frac{-\sigma_0 \delta t}{\epsilon_0}\right) + c^2 \delta t F_z \exp\left(\frac{-\sigma_0 \delta t}{2\epsilon_0}\right) \quad (5.22)$$

Or, using Equation (5.7) to map to the covariant basis,

$$E_3 \leftarrow E_3 \exp\left(\frac{-\sigma_0 \delta t}{\epsilon_0}\right) + c^2 \delta t (g_{31} F^1 + g_{33} F^3) \exp\left(\frac{-\sigma_0 \delta t}{2\epsilon_0}\right) \quad (5.23)$$

⁷³⁹ Tuna's conductivity profile gives a minimum value of $\frac{\sigma_0 \delta t}{\epsilon_0}$ on the order of 10^3 , making
⁷⁴⁰ $\exp\left(\frac{-\sigma_0 \delta t}{\epsilon_0}\right)$ far too small to be stored in a double precision variable¹⁴. That is, this
⁷⁴¹ model takes E_3 (and, proportionally, E_z) to be uniformly zero. This issue is revisited
⁷⁴² in Chapter 6.

The perpendicular components of Equation (5.20) give the expressions:

$$\begin{aligned} E_1 + \frac{g^{13}}{g^{11}} E_3 &\leftarrow E_1 \cos\left(\frac{-\sigma_H \delta t}{\epsilon_{\perp}}\right) \exp\left(\frac{-\sigma_P \delta t}{\epsilon_{\perp}}\right) \\ &\quad + E_2 \sin\left(\frac{-\sigma_H \delta t}{\epsilon_{\perp}}\right) \exp\left(\frac{-\sigma_P \delta t}{\epsilon_{\perp}}\right) \sqrt{\frac{g^{22}}{g^{11}}} \\ &\quad + E_3 \cos\left(\frac{-\sigma_H \delta t}{\epsilon_{\perp}}\right) \exp\left(\frac{-\sigma_P \delta t}{\epsilon_{\perp}}\right) \frac{g^{13}}{g^{11}} \\ &\quad + F^1 \cos\left(\frac{-\sigma_H \delta t}{2\epsilon_{\perp}}\right) \exp\left(\frac{-\sigma_P \delta t}{2\epsilon_{\perp}}\right) \frac{v_A^2 \delta t}{g^{11}} \\ &\quad + F^2 \sin\left(\frac{-\sigma_H \delta t}{2\epsilon_{\perp}}\right) \exp\left(\frac{-\sigma_P \delta t}{2\epsilon_{\perp}}\right) \frac{v_A^2 \delta t}{\sqrt{g^{11} g^{22}}} \end{aligned} \quad (5.24)$$

¹⁴Not coincidentally, $\frac{\sigma_0}{\epsilon_0}$ can also be written $\frac{\omega_P^2}{\nu}$. At the ionosphere, the collision frequency ν is fast compared to field line resonance timescales, but it's still slow compared to the plasma frequency.

and

$$\begin{aligned}
E_2 \leftarrow & -E_1 \sin\left(\frac{-\sigma_H \delta t}{\epsilon_{\perp}}\right) \exp\left(\frac{-\sigma_P \delta t}{\epsilon_{\perp}}\right) \sqrt{\frac{g^{11}}{g^{22}}} \\
& + E_2 \cos\left(\frac{-\sigma_H \delta t}{\epsilon_{\perp}}\right) \exp\left(\frac{-\sigma_P \delta t}{\epsilon_{\perp}}\right) \\
& - E_3 \sin\left(\frac{-\sigma_H \delta t}{\epsilon_{\perp}}\right) \exp\left(\frac{-\sigma_P \delta t}{\epsilon_{\perp}}\right) \frac{g^{13}}{\sqrt{g^{11} g^{22}}} \\
& - F^1 \sin\left(\frac{-\sigma_H \delta t}{2\epsilon_{\perp}}\right) \exp\left(\frac{-\sigma_P \delta t}{2\epsilon_{\perp}}\right) \frac{v_A^2 \delta t}{\sqrt{g^{11} g^{22}}} \\
& + F^2 \cos\left(\frac{-\sigma_H \delta t}{2\epsilon_{\perp}}\right) \exp\left(\frac{-\sigma_P \delta t}{2\epsilon_{\perp}}\right) \frac{v_A^2 \delta t}{g^{22}}
\end{aligned} \tag{5.25}$$

743 The E_3 terms in Equations (5.24) and (5.25) can be ignored at present. They are
744 revisited in Chapter 6.

745 It bears recalling that the driving current is defined as part of \underline{F} , per Equation (5.13).
746 When the driving current is purely azimuthal ($J^1 = J^3 = 0$), the driving is in principle
747 applied to both the poloidal and the toroidal electric fields through F^2 . However,
748 in practice, the driving applied to the toroidal electric field is vanishingly small. The
749 driving current J^2 is localized around $5 R_E$ geocentric, and $\exp\left(\frac{-\sigma_P \delta t}{2\epsilon_{\perp}}\right)$ drops off quickly
750 with altitude.

751 5.5 Boundary Conditions

752 Dirichlet and Neumann boundary conditions are applied to the electric field components
753 and magnetic field components respectively. That is, electric fields are forced to go to
754 zero at the inner and outer boundaries, and magnetic fields are forced to have a zero
755 derivative normal to the inner and outer boundaries.

756 These boundary conditions can in principle cause nonphysical reflections at the bound-
757 ary¹⁵. However, in practice, wave activity is concentrated well within the simulation
758 domain. Simulation results are robust under an exchange of Dirichlet and Neumann

¹⁵See, for example, the bottom row of Figure 5.4.

759 boundary conditions (though a self-inconsistent set of boundary condidtions, such as
 760 applying Neumann boundary conditions to B_1 but Dirichlet boundary conditions to B_3 ,
 761 quickly causes instability).

762 The Earthward boundary conditions are as follows.

Between the top of the neutral atmosphere and the bottom of the ionosphere, the model includes a thin, horizontal current sheet representing the ionosphere's E layer[59]. By integrating Ampère's law over the layer, it can be shown[28] that the horizontal electric field values at the edge of the grid are determined by the jump in the horizontal magnetic fields:

$$\underline{\underline{\Sigma}} \cdot \underline{E} = \frac{1}{\mu_0} \lim_{\delta r \rightarrow 0} \left[\hat{r} \times \underline{B} \right]_{R_I - \delta r}^{R_I + \delta r} \quad (5.26)$$

The integrated conductivity tensor $\underline{\underline{\Sigma}}$ can be written in θ - ϕ coordinates as[59]:

$$\underline{\underline{\Sigma}} \equiv \begin{bmatrix} \frac{\Sigma_0 \Sigma_P}{\Sigma_0 \cos^2 \alpha + \Sigma_P \sin^2 \alpha} & \frac{-\Sigma_0 \Sigma_H}{\Sigma_0 \cos^2 \alpha + \Sigma_P \sin^2 \alpha} \\ \frac{\Sigma_0 \Sigma_H}{\Sigma_0 \cos^2 \alpha + \Sigma_P \sin^2 \alpha} & \Sigma_P + \frac{\Sigma_H^2 \sin^2 \alpha}{\Sigma_0 \cos^2 \alpha + \Sigma_P \sin^2 \alpha} \end{bmatrix} \quad (5.27)$$

763 Where α is the angle between the magnetic field and the vertical direction, given by
 764 $\cos \alpha \equiv \frac{-2 \cos \theta}{\sqrt{1+3 \cos^2 \theta}}$, and Σ_P , Σ_H , and Σ_0 are the height-integrated Pedersen, Hall,
 765 and parallel conductivities respectively. Their values are determined by integrating
 766 Kelley's[49] conductivity profiles from Earth's surface to the ionospheric boundary; val-
 767 ues are shown in Table 5.2.

Table 5.2: Integrated Atmospheric Conductivity (S)

	Σ_0	Σ_P	Σ_H
Active Day	424	0.65	6.03
Quiet Day	284	0.44	4.02
Active Night	9	0.01	0.12
Quiet Night	9	0.01	0.12

An expression for the horizontal electric fields at the boundary can be obtained by inverting Equation (5.26). After mapping to covariant coordinates per Equation (5.8), and taking $\Sigma \equiv \det \underline{\underline{\Sigma}}$,

$$\begin{aligned} E_1 &\leftarrow \frac{1}{\mu_0 \Sigma} \lim_{\delta r \rightarrow 0} \left[-\Sigma_{\theta\phi} B_1 - \sqrt{\frac{g_{11}}{g_{22}}} \Sigma_{\phi\phi} B_2 \right]_{R_I-\delta r}^{R_I+\delta r} \\ E_2 &\leftarrow \frac{1}{\mu_0 \Sigma} \lim_{\delta r \rightarrow 0} \left[\sqrt{\frac{g_{22}}{g_{11}}} \Sigma_{\theta\theta} B_1 + \Sigma_{\phi\theta} B_2 \right]_{R_I-\delta r}^{R_I+\delta r} \end{aligned} \quad (5.28)$$

768 In order to compute the atmospheric magnetic field, a scalar magnetic potential (Ψ
769 such that $\underline{B} = \nabla\Psi$) is computed as a linear combination of harmonics. The neutral
770 atmosphere is considered to be a perfect insulator, giving $\nabla \times \underline{B} = 0$. Combined with
771 $\nabla \cdot \underline{B} = 0$ (per Maxwell's equations), Ψ satisfies Laplace's equation, $\nabla^2\Psi = 0$.

Laplace's equation can be solved analytically; however, a numerical solution is preferable to ensure orthonormality on a discrete and incomplete¹⁶ grid. After separating out the radial and azimuthal dependence in the usual way, the latitudinal component of Laplace's equation can be written in terms of $s \equiv -\sin^2\theta$:

$$(4s^2 + 4s) \frac{d^2}{ds^2} Y_\ell + (4 + 6s) \frac{d}{ds} Y_\ell - \frac{m^2}{s} Y_\ell = \ell(\ell+1) Y_\ell \quad (5.29)$$

Using centered differences to linearize the derivatives, Equation (5.29) becomes a system of coupled linear equations, one per field line. It can be solved numerically for eigenvalues $\ell(\ell+1)$ and eigenfunctions Y_ℓ ¹⁷. In terms of the harmonics Y_ℓ , Ψ between the Earth's surface and the top of the atmosphere can be written using eigenweights a_ℓ and b_ℓ :

$$\Psi = \sum_\ell \left(a_\ell r^\ell + b_\ell r^{-\ell-1} \right) Y_\ell \quad (5.30)$$

¹⁶As discussed in Section 5.1, the grid is constrained to finite L , which excludes the equator as well as the poles.

¹⁷Solving Laplace's equation analytically results in spherical harmonics indexed by both ℓ and m , the separation constants for θ and ϕ respectively. In two and a half dimensions, ϕ is not explicitly resolved, so m is set manually.

As a boundary condition for Ψ , Earth is assumed to be a perfect conductor. This forces the magnetic field at Earth's surface to be horizontal; that is, $B_r = \frac{\partial}{\partial r}\Psi = 0$. Noting that solutions to Laplace's equation are orthonormal, each element of the sum in Equation (5.30) must be independently zero at R_E . This allows the coefficients a_ℓ and b_ℓ to be expressed in terms of one another.

$$b_\ell = \frac{\ell}{\ell+1} R_E^{2\ell+1} a_\ell \quad (5.31)$$

The current sheet at the top of the atmosphere is assumed to be horizontal, so the radial component of the magnetic field must be the same just above and just below it. Taking the radial derivative of Equation (5.30) at the top of the atmosphere, and eliminating b_ℓ with Equation (5.31), gives

$$B_r = \sum_\ell \ell a_\ell R_I^{\ell-1} \left(1 - \lambda^{2\ell+1}\right) Y_\ell \quad \text{where} \quad \lambda \equiv \frac{R_E}{R_I} \sim 0.975 \quad (5.32)$$

The summation can be collapsed by “integrating” over a harmonic¹⁸. Inverse harmonics can be obtained by inverting the eigenvector matrix. Then $Y_\ell \cdot Y_{\ell'}^{-1} = \delta_{\ell\ell'}$ by construction.

$$a_\ell = \frac{1}{\ell R_I^{\ell-1}} \frac{B_r \cdot Y_\ell^{-1}}{1 - \lambda^{2\ell+1}} \quad (5.33)$$

Combining Equations (5.30), (5.31), and (5.33) allows the expression of Ψ at the top and bottom of the atmosphere as a linear combination of radial magnetic field components at the bottom of the ionosphere.

$$\begin{aligned} \Psi_E &= \sum_\ell Y_\ell \frac{R_I}{\ell(\ell-1)} \frac{(2\ell-1)\lambda^\ell}{1-\lambda^{2\ell+1}} B_r \cdot Y_\ell^{-1} \\ \Psi_I &= \sum_\ell Y_\ell \frac{R_I}{\ell(\ell-1)} \frac{(\ell-1)+\ell\lambda^{2\ell+1}}{1-\lambda^{2\ell+1}} B_r \cdot Y_\ell^{-1} \end{aligned} \quad (5.34)$$

¹⁸Because the functions are defined on a discrete grid, their inner product is not an integral, but a sum: $B_r \cdot Y_\ell^{-1} \equiv \sum_i B_r[i] Y_\ell^{-1}[i]$.

Horizontal magnetic fields are obtained by taking derivatives of Ψ .

$$B_1 = \frac{\partial}{\partial u^1} \Psi \quad B_2 = \frac{\partial}{\partial u^2} \Psi \quad (5.35)$$

- 772 Horizontal magnetic field values at the top of the atmosphere are used to impose bound-
773 ary conditions on the electric fields at the bottom of the ionosphere, per Equation (5.28).
774 Those at Earth's surface are valuable because they allow a direct comparison between
775 model output and ground magnetometer data, after being mapped to physical coordi-
776 nates per Equation (5.8).

777 **Chapter 6**

778 **Electron Inertial Effects**

779 As laid out in Chapter 5, Tuna resolves neither parallel currents nor parallel electric
780 fields. This is unfortunate; parallel electric fields generated by kinetic and inertial Alfvén
781 waves (including fundamental field line resonances[80, 96]) are a topic of particular
782 interest in the study of auroral particle precipitation.

Parallel currents and electric fields can be added to Tuna through the consideration of electron inertial effects in Ohm's law:

$$0 = \sigma_0 E_z - J_z \quad \text{becomes} \quad \frac{1}{\nu} \frac{\partial}{\partial t} J_z = \sigma_0 E_z - J_z \quad (6.1)$$

With the addition of the electron inertial term, it is necessary to track the parallel current independent of the parallel electric field¹. Solving by integrating factors² gives

$$J_3 \leftarrow J_3 \exp(-\nu \delta t) + \delta t \frac{ne^2}{m_e} E_3 \exp\left(-\nu \frac{\delta t}{2}\right) \quad (6.2)$$

¹The parallel current J_z is defined on the same points of the Yee grid as E_z . It is offset in time by half of a time step.

²The integrating factors technique is laid out explicitly for Ampère's law in Section 5.4.

From there, the parallel electric field can be updated directly; Equation (5.23) is replaced by the following:

$$E_3 \leftarrow E_3 + c^2 \delta t (g_{31} F^1 + g_{33} F^3) - \frac{\delta t}{\epsilon_0} J_3 \quad (6.3)$$

783 The present section explores the complications that arise from the addition of the elec-
 784 tron inertial term to Ohm's law, as well as a few results that may be gleaned despite
 785 those complications. Notably — for reasons discussed in Section 6.3 — the results
 786 presented in Chapter 7 do not make use of the electron inertial term.

787 6.1 The Boris Factor

With the addition of the electron inertial term, a cyclical dependence appears between Ampère's law and Ohm's law:

$$\frac{\partial}{\partial t} E_z \sim -\frac{1}{\epsilon_0} J_z \quad \text{and} \quad \frac{\partial}{\partial t} J_z \sim \frac{ne^2}{m_e} E_z \quad \text{so} \quad \frac{\partial^2}{\partial t^2} E_z \sim -\omega_P^2 E_z \quad (6.4)$$

788 That is, electron inertial effects come hand in hand with the plasma oscillation.
 789 As mentioned in Chapter 4 and shown in Figure 6.1, plasma oscillation is quite fast —
 790 several orders of magnitude smaller than Tuna's time step as determined in Section 5.1
 791 ($\sim 10 \mu\text{s}$). This poses a conundrum. At Tuna's usual time step, the plasma oscillation
 792 becomes unstable within seconds³. On the other hand, reducing the time step by three
 793 orders of magnitude to resolve the plasma oscillation is computationally infeasible; a
 794 run slated for an hour would require six weeks to complete.
 795 As it happens, this problem can be solved by artificially increasing the parallel electric
 796 constant above its usual value of ϵ_0 . Doing so lowers both the speed of light and the
 797 plasma frequency within the simulation.
 798 This technique — and others like it — has been widespread in numerical modeling since
 799 it was presented by Boris in 1970[6]. More recently, Lysak and Song considered its use

³For stability, $\omega_P \delta t < 1$ is necessary.

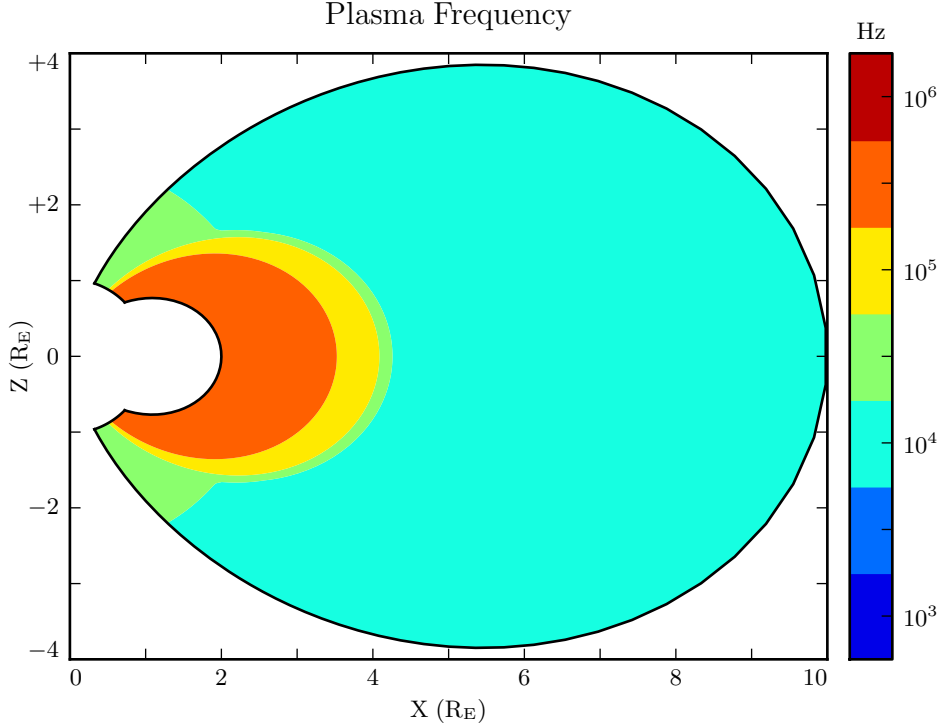


Figure 6.1: The plasma frequency reaches a peak value just under 10^6 Hz near the equator. Outside the plasmasphere, its value is closer to 10^4 Hz, which is still not well-resolved by Tuna's usual time step.

800 specifically for the case of electron inertial effects[61]. The following paraphrases their
 801 argument.

Supposing that the current and electric field are oscillating at frequency ω , the parallel components of Ampère's law and Ohm's law can be written

$$-i\omega\epsilon_0 E_z = \frac{1}{\mu_0} (\nabla \times \underline{B})_z - J_z \quad -\frac{i\omega}{\nu} J_z = \sigma_0 E_z - J_z \quad (6.5)$$

Then, eliminating the current, the parallel electric field can be related to the curl of the magnetic field by⁴

$$\left(1 - \frac{\omega^2 - i\nu\omega}{\omega_P^2}\right) E_z = \frac{c^2}{\omega_P^2} (\nu - i\omega) (\nabla \times \underline{B})_z \quad (6.6)$$

- 802 In Equation (6.6), $\frac{c}{\omega_P}$ is the electron inertial length. While the speed of light and the
 803 plasma frequency each depend on ϵ_0 , their ratio does not. This allows an estimation of
 804 how much the model should be affected by an artificially-large electric constant (and
 805 thus an artificially-small plasma frequency). So long as $\frac{\omega^2 - i\nu\omega}{\omega_P^2}$ remains small compared
 806 to unity, the model should behave faithfully.
- 807 For waves with periods of a minute or so, even perhaps-implausibly large Boris factors
 808 are allowed; for example, increasing ϵ_0 by a factor of 10^6 gives $\left|\frac{\omega^2 + i\omega\nu}{\omega_P^2}\right| \lesssim 0.01$.

809 6.2 Parallel Currents and Electric Fields

- 810 As discussed in Section 4.4, parallel electric fields in this regime are expected to be six
 811 or more orders of magnitude smaller than the perpendicular electric fields. Numerical
 812 results show general agreement: in Figure 6.2, the parallel electric field appears com-
 813 parable to its perpendicular counterparts only after its been scaled up by six orders of
 814 magnitude.
- 815 As such, the inclusion of electron inertial effects does not appreciably impact the sim-
 816 ulation's gross behavior; in Faraday's law, $\nabla \times \underline{E}$ is essentially unaffected. Side by side
 817 snapshots of the magnetic fields in runs carried out with and without electron inertial
 818 effects are not visibly distinguishable⁵ (not shown).
- 819 Even if there is no significant feedback through Faraday's law, it's informative to con-
 820 sider the structures that arise in parallel currents and electric fields driven by pertur-
 821 bations in the ring current. For example, the parallel electric field perturbation (with

⁴From Equation (4.4), $c^2 \equiv \frac{1}{\mu_0 \epsilon_0}$ and $\sigma_0 \equiv \frac{ne^2}{m_e \nu}$ and $\omega_P^2 \equiv \frac{ne^2}{m_e \epsilon_0}$.

⁵In a sense, this is reassuring. It ensures that the present section does not cast doubt on the results presented in Chapter 7, where electron inertial effects are neglected.

Electric Field Snapshots: Quiet Day, 10mHz Current, $m = 16$

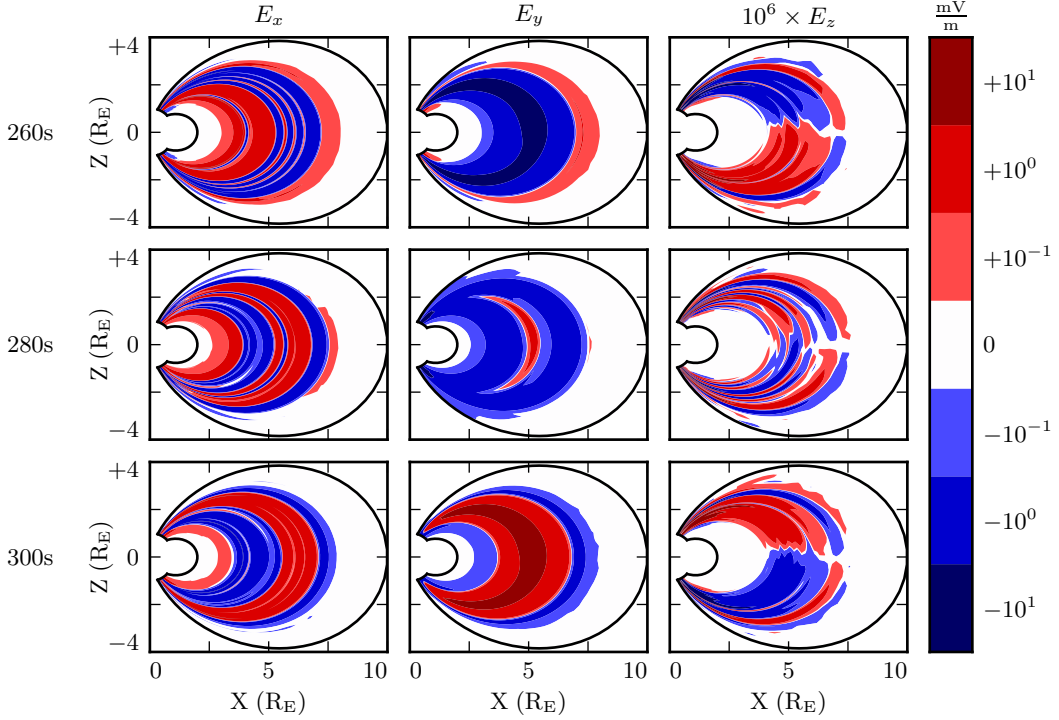


Figure 6.2: Parallel electric fields are smaller than perpendicular electric fields by about six orders of magnitude. As a result, parallel electric fields do not contribute significantly to $\nabla \times \underline{E}$ in Faraday's law.

maxima near the ionosphere) exhibits the opposite harmonic structure to the perpendicular electric field components (which peak near the equator). It is furthermore notable that the parallel electric field (and the parallel current that comes from it) exhibits real and imaginary components of comparable magnitude.

TODO: The compressional component of the magnetic field is also flipped compared to the perpendicular components. Should this have been mentioned in Chapter 3, with the figures showcasing harmonic structure? Radoski showed that it should be the case[79].

829

At low altitude, where the Hall conductivity muddles all of the electric field components together, parallel currents coincide with strong Poynting flux. The imaginary component

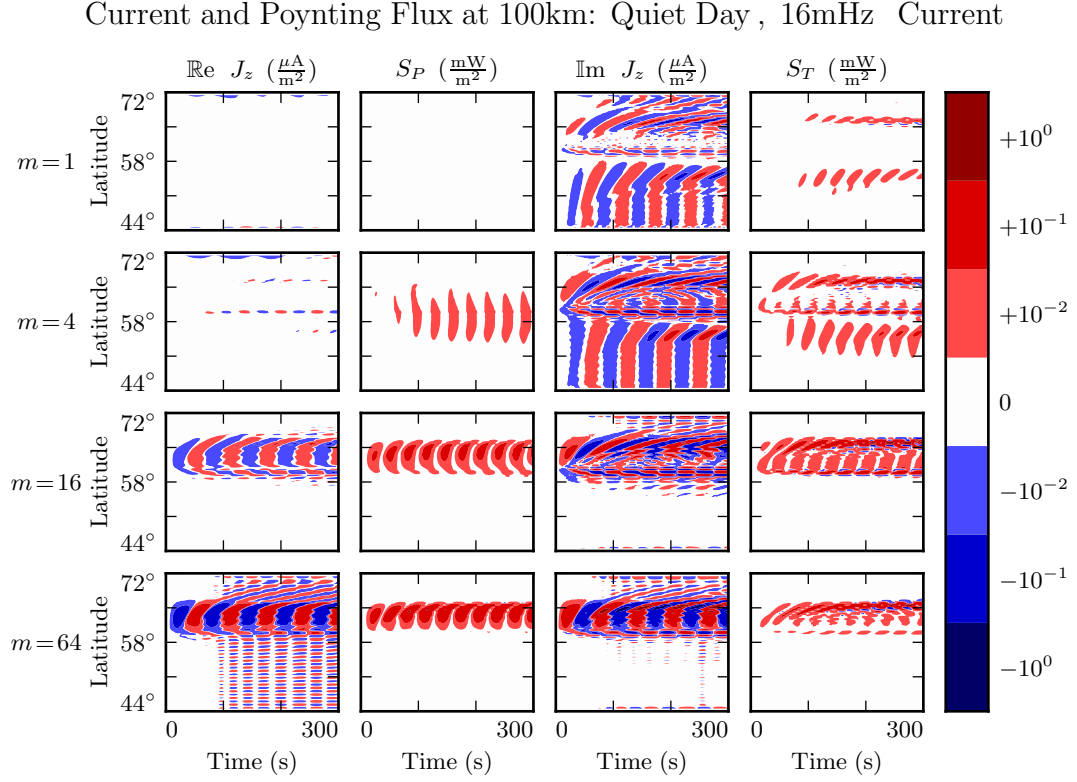


Figure 6.3: TODO: ...

- of the current lines up with the toroidal Poynting flux (which comes from imaginary E_x and imaginary B_y^*), while the real current lines up with the poloidal Poynting flux (E_y and B_x^* are real)⁶. This is shown in Figure 6.3, which lays out the real and imaginary components of the parallel current (in the first and third column respectively) next to the poloidal and toroidal Poynting flux (second and fourth columns). Four runs are shown, one per row, with azimuthal modenumbers 1, 4, 16, and 64. Values are measured at an altitude of 100 km, the edge of the simulation.
- Notably, the Poynting flux waveforms are rectified — they primarily carry energy Earthward. The current, on the other hand, alternates between upward and downward flow.

⁶As mentioned in Chapter 5, poloidal field components are in practice overwhelmingly real, indicating that they coincide azimuthally with the (real) driving. Toroidal components are overwhelmingly imaginary, which corresponds to an azimuthal offset.

- 841 This effect presumably arises because the current is a linear quantity while the Poynting
 842 flux is quadratic: the electric and magnetic fields that make it up oscillate in phase, so
 843 their product is positive even when they are negative.
- 844 At higher altitude, where the Hall conductivity is small, parallel current is associated
 845 only with the toroidal mode. Figure 6.4 shows data from the same runs as Figure 6.3,
 846 arranged in the same way, but the values are taken at an altitude of 1000 km instead of
 847 100 km.
- 848 In Figure 6.4, as in Figure 6.3, the imaginary component of the parallel current (third
 849 column) coincides more or less with the toroidal Poynting flux (fourth column). How-
 850 ever, the real component of the parallel current (first column) is vanishingly small, even
 851 when the poloidal Poynting flux (second column) is strong. **TODO: Is this expected?**
 852 **Tikhonchuk[96] looks specifically at the toroidal mode when considering shear Alfven**
 853 **waves. Does the poloidal mode count as compressional even when it's guided?**
- 854 The magnitude of the parallel current tops out over $1 \mu\text{A}/\text{m}^2$, just shy of the up-to-tens
 855 of $\mu\text{A}/\text{m}^2$ inferred from ground observations and seen in situ[8, 47, 83].

It's also possible to consider the effect of parallel currents and electric fields on the ionosphere's energy budget, per Poynting's theorem:

$$\frac{\partial}{\partial t} u = -\nabla \cdot \underline{E} - \underline{J} \cdot \underline{E} \quad (6.7)$$

- 856 As shown in Figure 6.5, little energy transfer in the ionosphere is mediated by perpen-
 857 dicular components of the Poynting flux. The parallel component of $\underline{J} \cdot \underline{E}$ is comparably
 858 unimportant. The energy deposited in the ionosphere by the Poynting flux matches
 859 closely with the energy lost to Joule dissipation — as it should, to conserve energy
 860 — but according to the model, parallel currents and electric fields do not contribute
 861 significantly.

Current and Poynting Flux at 1000km: Quiet Day , 16mHz Current

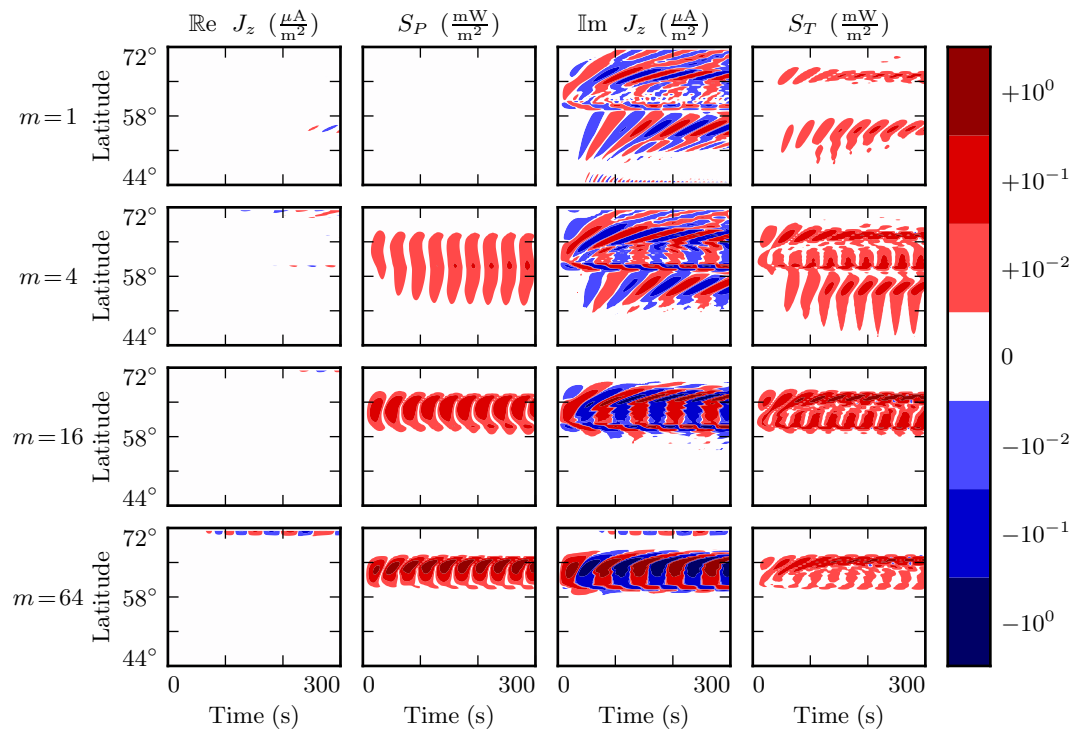


Figure 6.4: TODO: ...

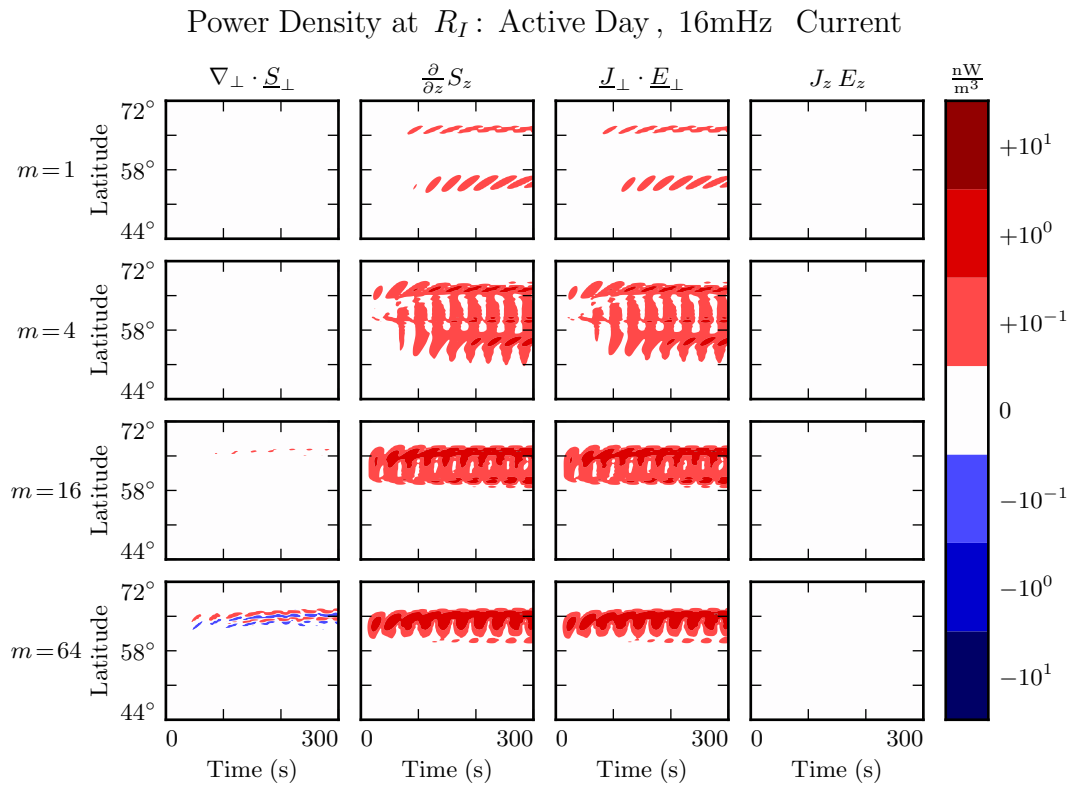


Figure 6.5: While field-aligned currents can be of significant size, they are not particularly good at depositing energy in the ionosphere. Energy deposited by the Poynting flux matches closely with Joule dissipation from the perpendicular currents, while $J_z E_z$ is smaller by several orders of magnitude.

862 **6.3 Inertial Length Scales**

863 It's not quite fair to compare the parallel and perpendicular contributions to $\nabla \times \underline{E}$ as
864 is done in Section 6.2. Perpendicular electric fields are on the order of 1 mV/m, with
865 wavelengths on the order of 10^5 km; they give rise to magnetic field gradients around
866 0.1 nT/s. Parallel electric fields, closer to 10^{-6} mV/m, would need to vary over length
867 scales of 0.1 km to match with that.

868 Such scales are believable. The characteristic length scale of the plasma oscillation is
869 the electron inertial length, $\frac{c}{\omega_p}$, which is on the order of 1 km in the auroral ionosphere
870 and 0.1 km in the low-altitude plasmasphere. However, Tuna's usual grid doesn't resolve
871 structures so fine; its resolution bottoms out closer to 10 km. That is, with the inclusion
872 of electron inertial effects, Tuna's grid is too coarse to resolve all of the waves expected
873 to be present. The model is prone to instability as a result.

874 Figure 6.6 shows a run with perpendicular resolution smaller than the electron inertial
875 length, side by side with an analogous run on the usual grid. In order to carry out
876 the inertial-scale run, several concessions were made to computational cost. The run
877 simulates only a duration of 100 s (other results in previous sections and in Chapter 7
878 show 300 s), and the grid covers only the auroral latitudes from $L = 5$ to $L = 7$.

879 Even so, the run presents a significant computational expense. Spread over 16 cores, a
880 100 s run on Tuna's usual grid takes well under an hour. The inertial-scale run barely
881 finished in 96 hours, the cutoff at the Minnesota Supercomputing Institute⁷.

882 The snapshot shown in Figure 6.6 uses a perpendicular grid resolution of 0.7 km at the
883 Earthward edge, which just satisfies the Nyquist rate for the minimum inertial length
884 of 1.7 km. It's still too coarse. There is clearly some small-scale structure developing in
885 the ionosphere, but it's not well resolved. The large number of "wiggles" portends an
886 imminent crash.

⁷Runtime goes as the inverse square of grid resolution. Not only does finer resolution require more grid cells, but it also gives rise to proportionally smaller crossing times, imposing a smaller time step.

Parallel Electric Fields: Quiet Day, 100s of 16mHz Current, $m = 16$

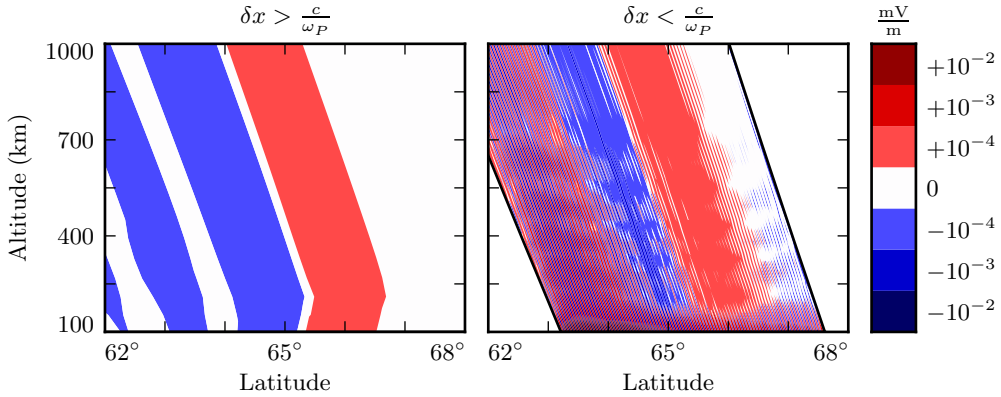


Figure 6.6: The parallel electric field develops significant structure when the perpendicular grid resolution is smaller than the electron inertial length. Unfortunately, such runs are prohibitively expensive. The lower panel — which still fails to resolve wave structure properly — represents a 100-fold increase in computational time.

887 6.4 Discussion

888 TODO: The dispersion relation in Chapter 4 suggests that parallel electric fields should
 889 be smaller than perpendicular electric fields by at least six orders of magnitude. Tuna
 890 agrees.

891 TODO: Tuna computes parallel currents a bit weaker than those that are observed —
 892 $\sim 1 \mu\text{A}/\text{m}^2$ rather than $\sim 10 \mu\text{A}/\text{m}^2$. The currents accompany the toroidal mode, but
 893 not the poloidal mode, except where the two are coupled by a strong Hall conductivity.
 894 Is this expected?

895 TODO: When inertial effects are not properly resolved, the code is prone to instability.
 896 Resolving inertial scales properly presents a prohibitive computational expense.

897 Electron inertial effects present a promising first-principles-based approach to the in-
 898 vestigation of parallel currents and electric fields associated with field line resonances.
 899 Unfortunately, because of the large differences in scale between Pc4 pulsations and the

900 plasma oscillation, the proper deployment of inertial effects presents a prohibitive com-
901 putational expense. Results shown in Chapter 7 make use of the core version of Tuna
902 presented in Chapter 5, which does not include the effects of electron inertia.

903 **Chapter 7**

904 **Numerical Results**

905 In his 1974 paper, Radoski argues that a poloidally-polarized wave should asymptotically rotate to the toroidal polarization[79] as a result of the curved derivative in the 906 meridional plane. The question of finite poloidal lifetimes is considered further in a 1995 907 paper by Mann and Wright[65]. Their numerical work used a straightened field line, 908 with an Alfvén speed gradient in the “radial” direction. They also found a rotation over 909 time from poloidal to toroidal polarization, with the characteristic time proportional to 910 the azimuthal modenumber.

912 **TODO:** Ding et al[21] did similar work just before Mann and Wright, but results were 913 less clear, possibly due to issues with grid resolution (as discussed in [65]).

914 **TODO:** Mann and Wright looked specifically at second harmonics. This work is on first 915 harmonics. (In principle Tuna allows arbitrary driving waveforms and spatial distribu-916 tions.)

917 The present chapter builds on the aforementioned results by relaxing several of their 918 nonphysical assumptions. Tuna’s geometry (as described in Chapter 5) is far more 919 realistic than Radoski’s half-cylinder or the box model used by Mann and Wright. 920 Magnetic field lines are dipolar. Alfvén speed is based on an empirical profile, and 921 varies along and across field lines. The present work also features driving delivered over 922 time through perturbation of the ring current; past work has instead considered only the

923 evolution of an initial condition. Finally, the present model includes a height-resolved
 924 ionosphere (rather than perfectly-reflecting boundaries). The ionospheric conductivity
 925 provides a direct coupling between the poloidal and toroidal modes, in addition to
 926 dissipating energy.

Energy is computed per Poynting's theorem, with due consideration of the unusual geometry. Energy density is integrated over the meridional plane, but not in the azimuthal direction, giving units of gigajoules per radian; more than anything else, this serves as a reminder that the waves under consideration are azimuthally localized. The energy in the poloidal mode and the energy in the toroidal mode are, respectively,

$$U_P = \int \frac{du^1 du^3}{2\mu_0 \sqrt{g}} \left(B_x^2 + \frac{1}{v_A^2} E_y^2 \right) \quad U_T = \int \frac{du^1 du^3}{2\mu_0 \sqrt{g}} \left(B_y^2 + \frac{1}{v_A^2} E_x^2 \right) \quad (7.1)$$

927 TODO: We look at the interplay between poloidal-to-toroidal rotation, Joule dissipation,
 928 etc.

929 TODO: The overarching motivation for this work is that Pc4 pulsations vary in interesting
 930 ways with respect to azimuthal modenumber, and that prior models have been
 931 unable to give a good picture of that behavior.

932 TODO: It's possible that the contour plots (Sections 7.2 and 7.4) should go before the
 933 line plots (Sections 7.1 and 7.3). They sorta depend on one another. Unclear if there's
 934 a better way to divide things up.

935 7.1 Finite Poloidal Lifetimes: Dayside

936 Each subplot in Figures 7.1 and 7.2 is analogous to Figure 3 in Mann and Wright's
 937 paper[65]. Blue lines show the total energy in the poloidal mode as a function of time.
 938 Red lines show toroidal energy. Runs are organized such that driving frequency is
 939 constant down each column, and azimuthal modenumber is constant across each row.
 940 Axis bounds are held constant across all subplots.

941 The 28 runs shown in Figure 7.1 use a high-conductivity profile, corresponding to the
 942 dayside with low solar activity (shown in Section 5.2). The two dayside profiles —

943 active and quiet — are contrasted briefly in Section 7.6. However, the primary focus is
944 on the difference between the dayside and the nightside. The differences between the
945 two dayside profiles are minor in comparison.

946 The fact that red (toroidal) lines appear at all speaks to the coupling of the poloidal
947 and toroidal modes. As discussed in Section 5.3, driving in Tuna is delivered purely
948 into the poloidal electric field (reflecting the azimuthal direction of the ring current).

949 As expected, the rotation from poloidal to toroidal is slowest at large azimuthal mode-
950 numbers. The toroidal energy overtakes the poloidal energy within a single drive period
951 at $m = 4$; at $m = 64$, the most of the energy is in the poloidal mode for ~ 10 periods.
952 However, the relationship between azimuthal modenumber and rotation timescale is not
953 linear, as was suggested by Mann and Wright. Instead, the rotation is fastest at $m = 4$.

954 This hints at two competing effects, and there are only so many options. In addition
955 to the poloidal-to-toroidal rotation, the two modes are coupled by the ionospheric Hall
956 conductivity; energy is also lost when waves propagate out of the simulation domain,
957 when driving interferes destructively with a wave, and as a result of Joule dissipation.

958 In practice, the Hall conductivity does not move large amounts of energy between the
959 poloidal and toroidal modes. In fact, when the runs shown in Figure 7.1 are repeated
960 with Hall conductivity uniformly zero (not shown), the energy curves do not change
961 appreciably.

962 Joule dissipation — a recurring topic in the present chapter — is a major player in the
963 simulation’s energy economy, but does not depend directly on the azimuthal modenum-
964 ber. Similarly, azimuthal modenumber does not immediately impact the interference
965 between a wave and its driver.

966 That leaves the propagation of energy across field lines, which does explain the ob-
967 served behavior. As the azimuthal modenumber increases past order unity, compres-
968 sional Alfvén waves in the Pc4 band become evanescent¹. Runs in the top two rows
969 lose considerable sums of energy as a result of waves propagating out of the simulation

¹See Section 4.4.

970 domain. In contrast, runs conducted at higher modenumber do not permit the com-
971 pressional propagation of Alfvén waves, so energy does not escape through the outer
972 boundary.

973 Notably, the low-modenumber runs at 19 mHz do accumulate significant energy over
974 time, while those at 13 mHz, 16 mHz, and 22 mHz falter. This response is likely non-
975 physical, and is discussed in Section 7.2.

976 In each run, the energy of the system is asymptotically determined by the balance
977 between the energy input (from driving) and the energy loss (through Joule dissipation
978 in the ionosphere and escape through the boundary). When the driving frequency
979 matches closely with the local Alfvén frequency, energy accumulates over a number of
980 drive periods, leading to a relatively large asymptotic energy in the system.

981 The system’s resonant frequency (for a fundamental poloidal mode at $L \sim 5$) is affected
982 significantly by the size of the plasmasphere. In Figure 7.1, with the plasmapause at
983 $L_{PP} = 4$, the system resonates at 19 mHz at low m ; as m becomes large, the resonant
984 frequency is closer to 22 mHz. Figure 7.2 shows the effect of moving the plasmapause
985 to $L_{PP} = 5$: resonance is closer to 16 mHz. The runs are otherwise identical to those
986 shown in Figure 7.1.

987 **TODO:** In most cases, the energy in the toroidal mode exceeds the energy in the poloidal
988 mode.

989 **TODO:** The late, long dips in energy are probably due to “beats” in the interference
990 between the driving frequency and the bounce frequency.

Poloidal (Blue) and Toroidal (Red) Energy: Quiet Day , $L_{PP} = 4$, $L_{drive} = 5$

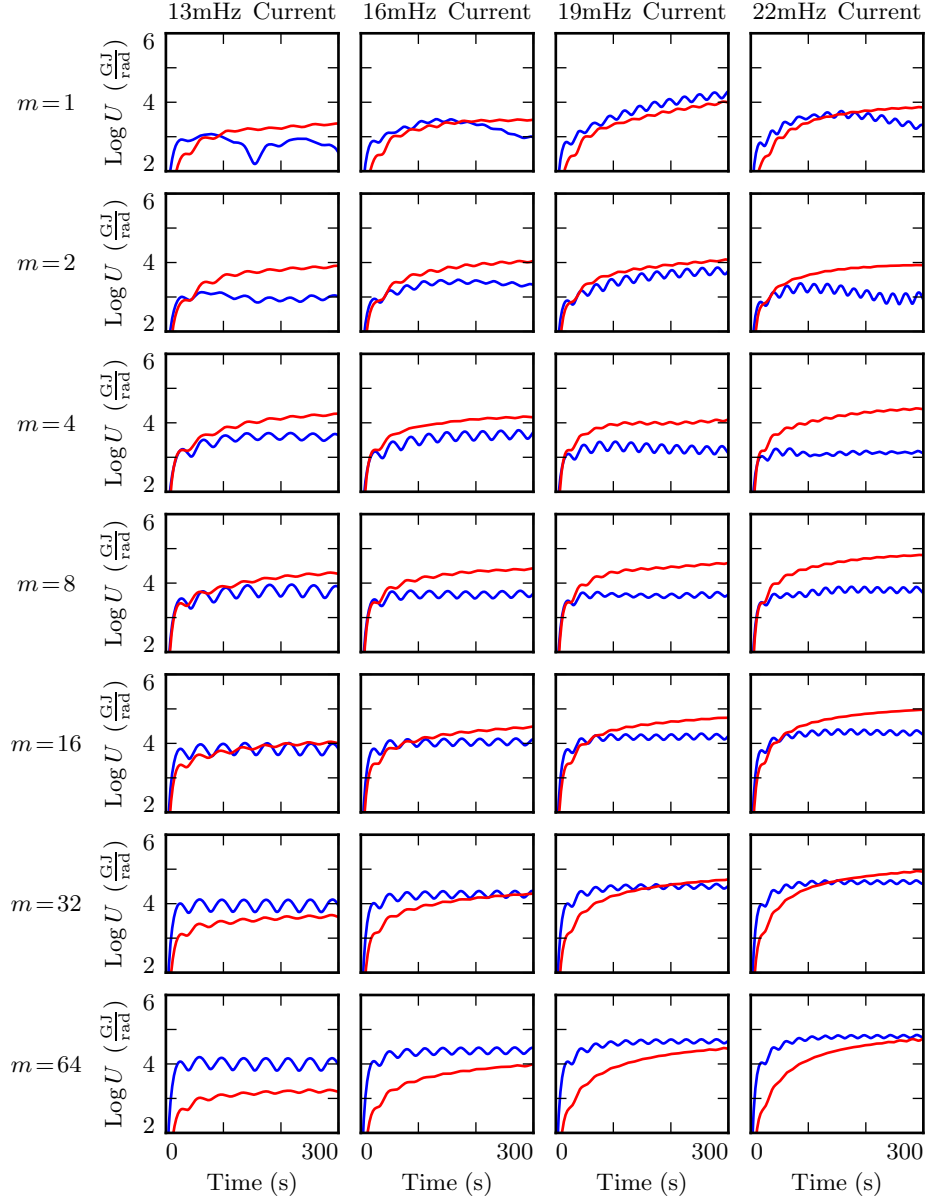


Figure 7.1: Each subplot above corresponds to a 300s run of Tuna. Driving is continuously injected into the poloidal mode (energy in blue). The waves rotate asymptotically to the toroidal mode (red). When the azimuthal modenumber (rows) is large, the rotation is slower. The driving frequency (columns) also affects the asymptotic accumulation of energy.

Poloidal (Blue) and Toroidal (Red) Energy: Quiet Day , $L_{PP} = 5$, $L_{drive} = 5$

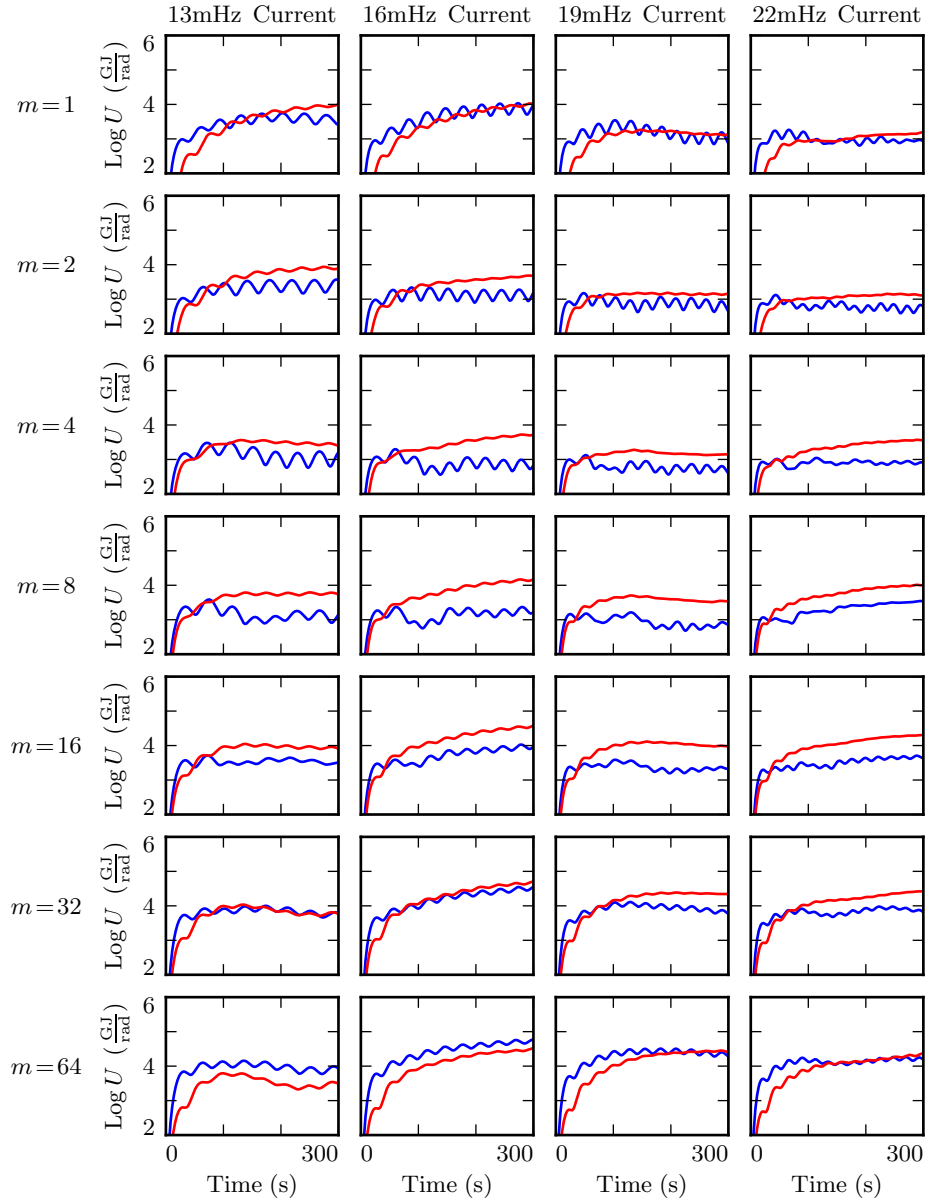


Figure 7.2: Above is a figure identical to Figure 7.1, except that the plasmapause has been moved from $L_{PP} = 4$ to $L_{PP} = 5$. This affects which driving frequency is closest to the resonant Alfvén frequency, and hence is most effective in causing a buildup of energy over time.

991 7.2 Spatial Distribution of Energy: Dayside

992 Looking a bit deeper, it's possible to comment on the structure of the poloidal and
993 toroidal modes, not just their magnitudes. The subplots in Figures 7.3 to 7.5 are
994 arranged analogously to those in Section 7.1: each comes from a different run, mode-
995 number is held constant across each row, and frequency down each column.

996 Contours represent energy density, averaged over the volume of a flux tube. The vertical
997 axis shows L -shell, while the horizontal axis is time. As above, poloidal and toroidal
998 energy density are computed separately.

999 Figure 7.3 shows why, at low modenumber, the poloidal mode does not resonate well.
1000 Its compressional component allows energy to be spread broadly in L — in fact, at
1001 $m = 1$, no energy buildup at all is apparent at the location of the driving.

1002 Some energy moves inward, and is trapped in the plasmapause's steep Alfvén speed
1003 gradient (particularly visible in the 16 mHz, $m = 4$ run). Some energy builds up in a
1004 third harmonic resonance near the outer boundary (shown best in runs with $m = 1$). The
1005 time spent propagating across field lines counts against the poloidal mode's finite lifetime
1006 — by the time a poloidally-polarized wave reaches the outer boundary, a significant
1007 fraction of its energy has rotated to the toroidal mode.

1008 It's likely that at 19 mHz, with $m = 1$, the response is artificially amplified through
1009 interaction with the boundary conditions. As mentioned in Section 5.5, nonphysical
1010 reflections can occur when waves are very close to the boundary. In most cases, waves
1011 are not localized at the boundary, so this is not a concern.

1012 The peak energy density in the bottom-right run (22 mHz driving, $m = 64$) is by far the
1013 largest of any run in Figure 7.3. The azimuthal modenumber is large, so the poloidal
1014 mode is purely guided; no time is wasted with movement across magnetic field lines.
1015 And, crucially, the frequency of the driving aligns closely with the resonant frequency
1016 where it's delivered. Other runs on the bottom row also have $m = 64$ (and so are also
1017 guided), but their driving frequencies do not align with the local resonant frequency.
1018 As a result, they do not accumulate energy over a large number of drive periods.

1019 Similar behavior can be seen in Figure 7.4 (which shows the same runs as Figure 7.2,
1020 with the plasmapause moved to $L_{PP} = 5$ from its default location at $L_{PP} = 4$). A third
1021 harmonic resonance can be seen at the outer boundary for runs on the top row ($m = 1$).
1022 The effect of the plasmapause is particularly visible in the middle row, $m = 8$, where
1023 energy accumulates both just inside and just outside $L_{PP} = 5$. At high modenumber,
1024 the driving resonates best at 16 mHz; at other frequencies, energy density has a lower
1025 asymptotic value, which is reached more quickly.

1026 In Figures 7.3 and 7.4, the poloidal contours show energy smeared across a swath of
1027 L -shells. On the other hand — as shown in Figure 7.5 — the toroidal mode appears
1028 only where the drive frequency matches the local eigenfrequency.

1029 A horizontal line drawn through the Alfvén speed frequency profiles (recall Figure 3.1)
1030 intersects the profile up to three times: once as the Alfvén frequency drops through the
1031 Pc4 range from its low-latitude peak, again as the Alfvén frequency rises sharply at the
1032 plasmapause, and a third time as the Alfvén frequency drops asymptotically. Toroidal
1033 waves can be seen resonating at all three of these locations in the $m = 4, 19$ mHz run
1034 in Figure 7.5, along with a third harmonic at large L .

1035 This is consistent with observations: toroidal resonances are noted for having frequencies
1036 which depend strongly on L , in contrast to the poloidal mode’s less-strict relationship
1037 between frequency and location.

1038 The dayside poloidal modes shown in Figures 7.3 and 7.4 attain an energy density on the
1039 order of 10^{-1} nJ/m³ only under ideal conditions: high modenumber runs with driving
1040 close to the local Alfvén frequency. Between the 56 dayside runs shown, such energy
1041 density appears only twice. On the other hand, the toroidal mode reaches $\sim 10^{-1}$ nJ/m³
1042 in six of the runs in Figure 7.5 alone. That is, the poloidal mode only exhibits a high
1043 energy density on the dayside only when conditions are ideal; the toroidal mode isn’t
1044 nearly so particular.

Poloidal Energy Density by L-Shell: Quiet Day , $L_{PP} = 4$, $L_{drive} = 5$

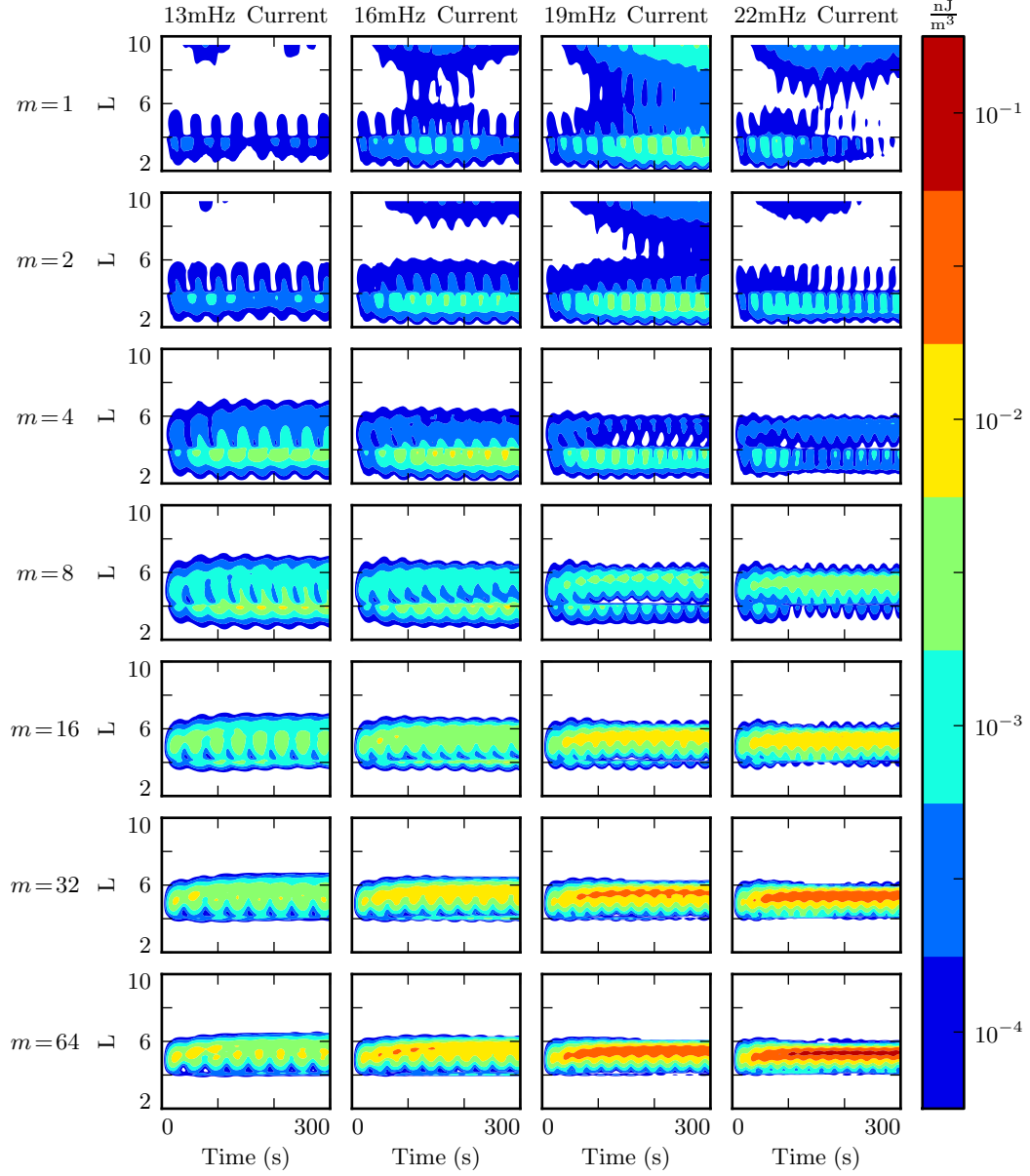


Figure 7.3: Each subplot above corresponds to a 300s run of Tuna, driven in the poloidal mode. At low m , energy instead moves radially and rotates quickly to the toroidal mode, precluding the formation of poloidal FLRs. At high m , the poloidal mode is guided, and the mode rotation is slow, allowing a strong resonance — but only when the driving frequency matches the local Alfvén frequency.

Poloidal Energy Density by L-Shell: Quiet Day , $L_{PP} = 5$, $L_{drive} = 5$

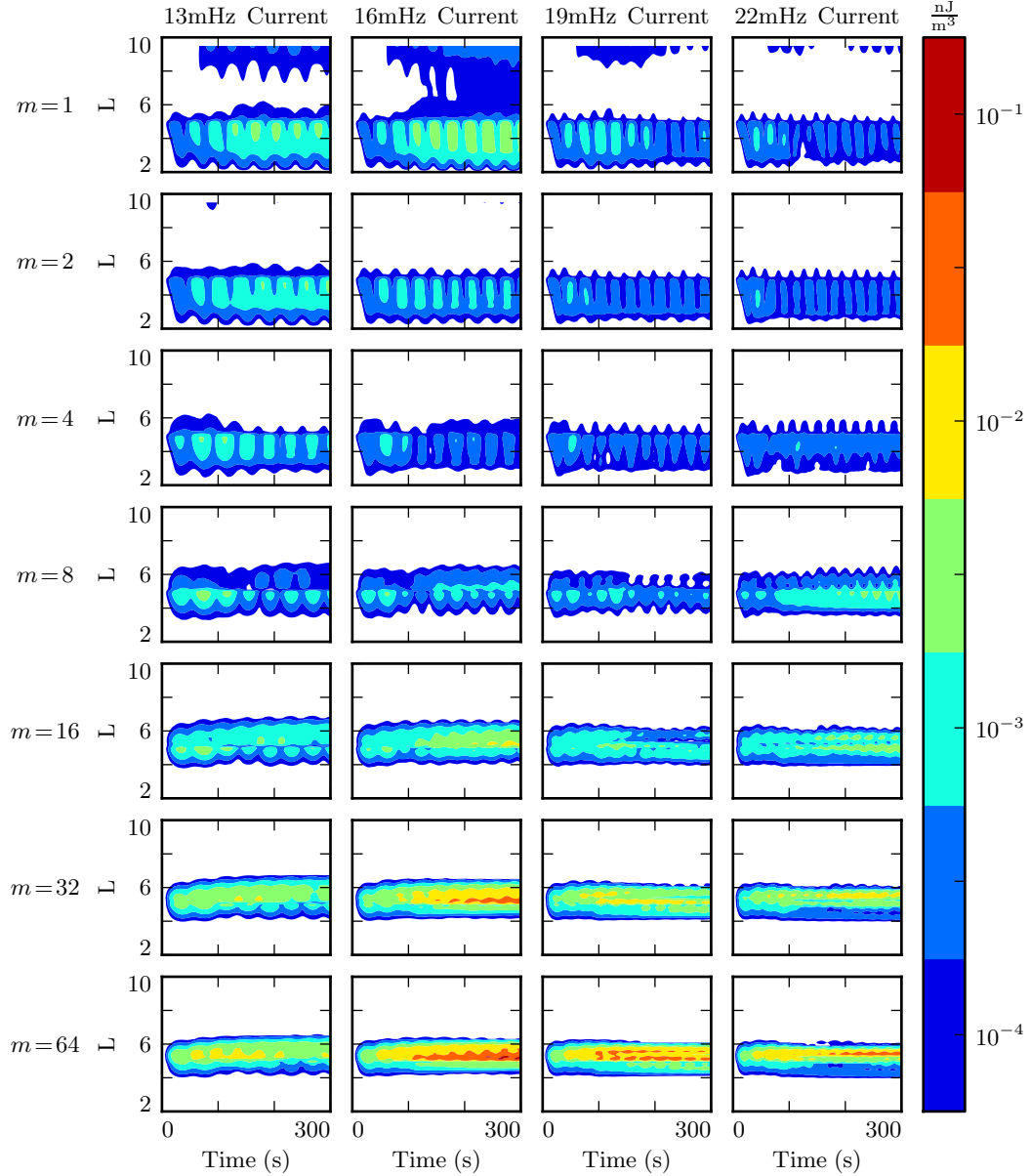


Figure 7.4: The Alfvén frequency profile is significantly affected by the size of the plasmasphere. The runs shown above are identical to those in Figure 7.3, except that the plasmapause has been moved from $L_{PP} = 4$ to $L_{PP} = 5$. As a result, the most effective resonance at $L \sim 5$ is shifted from 22 mHz to 16 mHz.

Toroidal Energy Density by L-Shell: Quiet Day , $L_{PP} = 4$, $L_{drive} = 5$

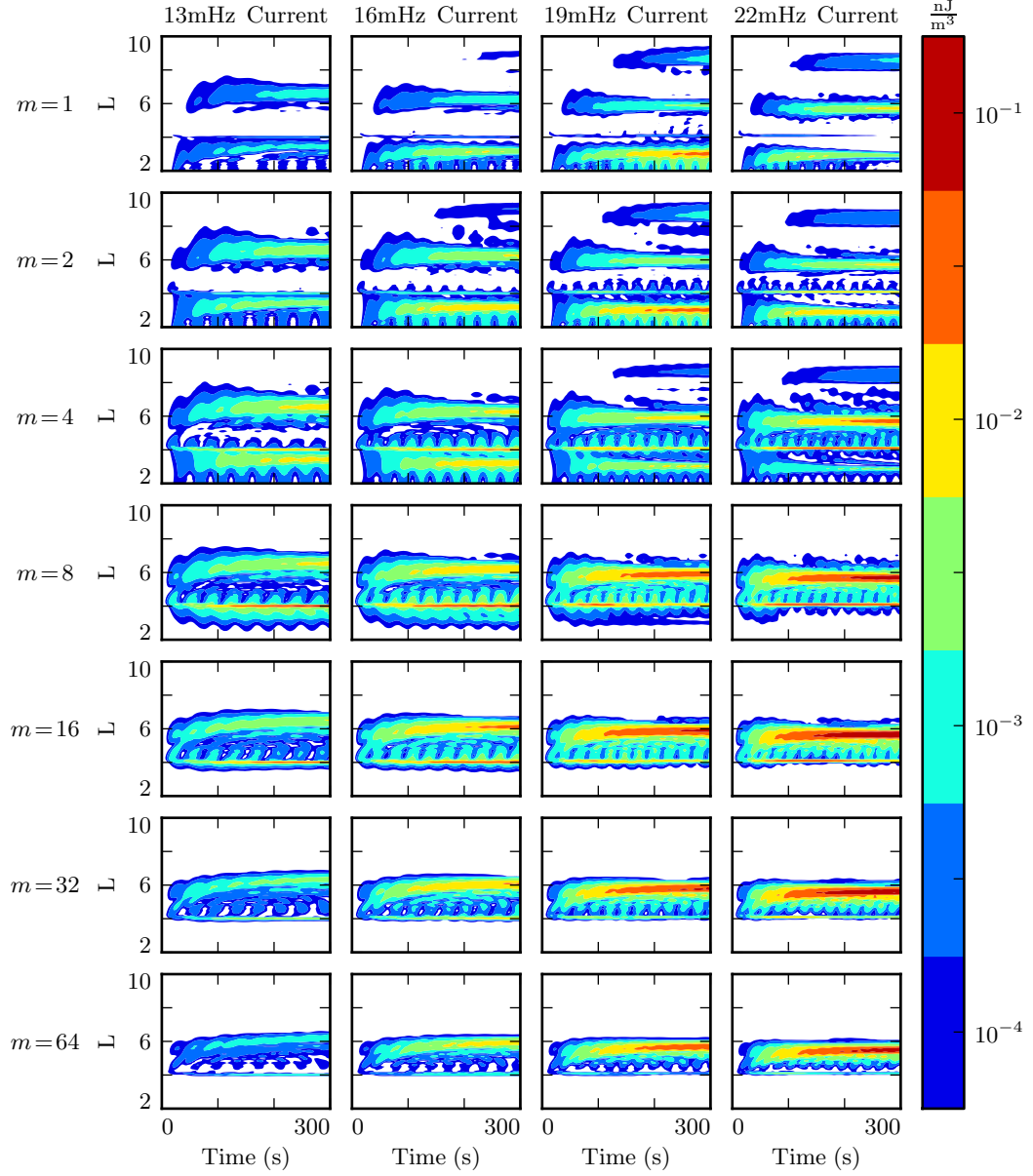


Figure 7.5: On the dayside, energy accumulates in the toroidal mode only at L values where the drive frequency matches a local eigenfrequency. This is in contrast to the more smeared appearance of the poloidal contours shown in Figures 7.3 and 7.4. Furthermore, the toroidal mode attains a high energy density under more diverse conditions than the poloidal mode.

1045 **7.3 Finite Poloidal Lifetimes: Nightside**

1046 Compared to the dayside ionosphere employed in Section 7.1, the nightside profiles
1047 exhibit two major differences. The ionospheric conductivity is lower, and the Alfvén
1048 speed is higher. The present section and Section 7.4 show results using only the active
1049 nightside profile. The differences between the quiet and active nightside ionospheric
1050 profiles are small compared to the differences between either dayside profile and either
1051 nightside profile; all four profiles are briefly compared in Section 7.6.

1052 The low conductivity on the nightside gives rise to strong Joule dissipation. Waves are
1053 damped out in just a few bounces, so asymptotic energy values are reached quickly.
1054 Even so, the poloidal-to-toroidal rotation is qualitatively the same as on the dayside.
1055 The further the azimuthal modenumber from the rotation peak at $m = 4$, the lower the
1056 asymptotic toroidal energy level is compared to the poloidal. If anything, the effect is
1057 exaggerated by the small dissipation timescale. When $m = 64$, no more than $\sim 10\%$ of
1058 the energy in the poloidal mode rotates to the toroidal mode before being lost.

1059 Figure 7.6 is arranged analogously to the figures in Section 7.1: each subplot is an inde-
1060 pendent run, drive frequency is constant down each column, and azimuthal modenumber
1061 is constant across each row. Poloidal energy is blue; toroidal energy is red.

1062 The lower energies in Figure 7.6 (compared to Figure 7.1, the analogous dayside runs)
1063 are not entirely due to increased Joule dissipation. Due to the difference in electric
1064 constant between the dayside and nightside magnetospheres², resonant frequencies just
1065 outside the typical ($L_{PP} = 4$) plasmapause fall well outside the $Pc4$ range. None of
1066 the frequencies shown in Figure 7.6, when delivered at $L_{drive} = 5$, align with the local
1067 eigenfrequency.

1068 As in Section 7.1, the 19 mHz run with $m = 1$ is an apparent exception. A large
1069 amount of energy builds up in a third harmonic very close to the outer boundary. The
1070 interaction is likely nonphysical.

1071 **TODO:** It may be significant that $\int \sigma dz$ is constant across all L -shells, but $\int \frac{\sigma}{v_A^2} dz$ is
1072 not.

2See Figure 3.1.

1073 Behavior closer to resonance is shown in Figure 7.7. The plasmapause remains at
1074 $L_{PP} = 4$, but the driving is moved out to $L_{drive} = 6$, at which point the local Alfvén
1075 frequency overlaps the Pc4 frequency band.

1076 There is surprisingly little difference between Figures 7.6 and 7.7 (the subplots of which
1077 are arranged analogously). Asymptotic energy levels vary — in the case of high m and
1078 low frequency, runs in Figure 7.7 are more energetic by an order of magnitude or more
1079 — but the qualitative behavior is the same. Driving is balanced by dissipation over the
1080 course of just a few drive periods. Dissipation outstrips poloidal-to-toroidal rotation in
1081 the case of large azimuthal modenumber. And, unlike on the dayside, the toroidal mode
1082 typically does not match the asymptotic energy level seen in the poloidal mode.

Poloidal (Blue) and Toroidal (Red) Energy: Active Night , $L_{PP} = 4$, $L_{drive} = 5$

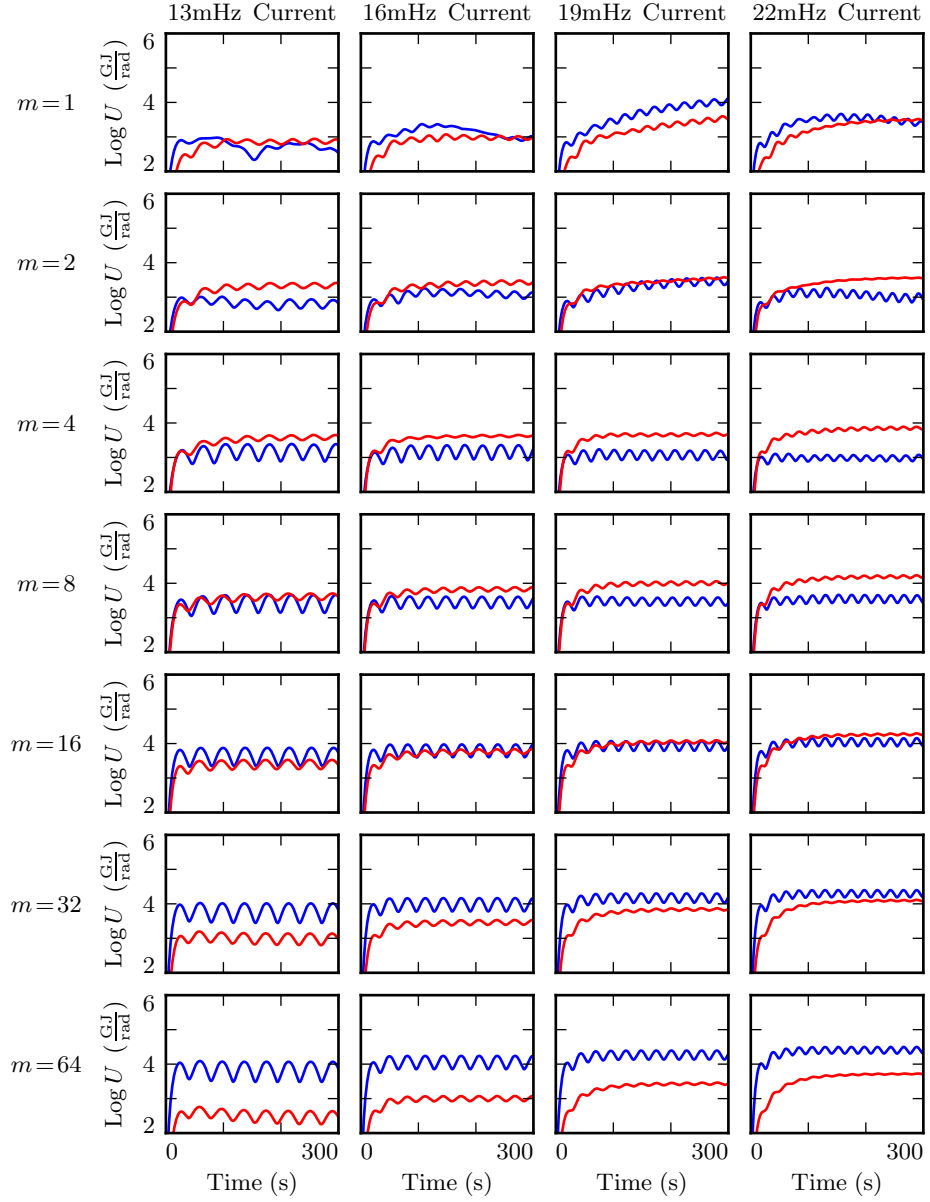


Figure 7.6: On the nightside, driving in the $\text{Pc}4$ band is not resonant at $L \sim 5$. This — combined with the lower ionospheric conductivity — causes the poloidal (blue) and toroidal (red) energies to quickly reach their asymptotic values. As on the dayside, energy rotates from poloidal to toroidal most effectively at small-but-finite m .

Poloidal (Blue) and Toroidal (Red) Energy: Active Night , $L_{PP} = 4$, $L_{drive} = 6$

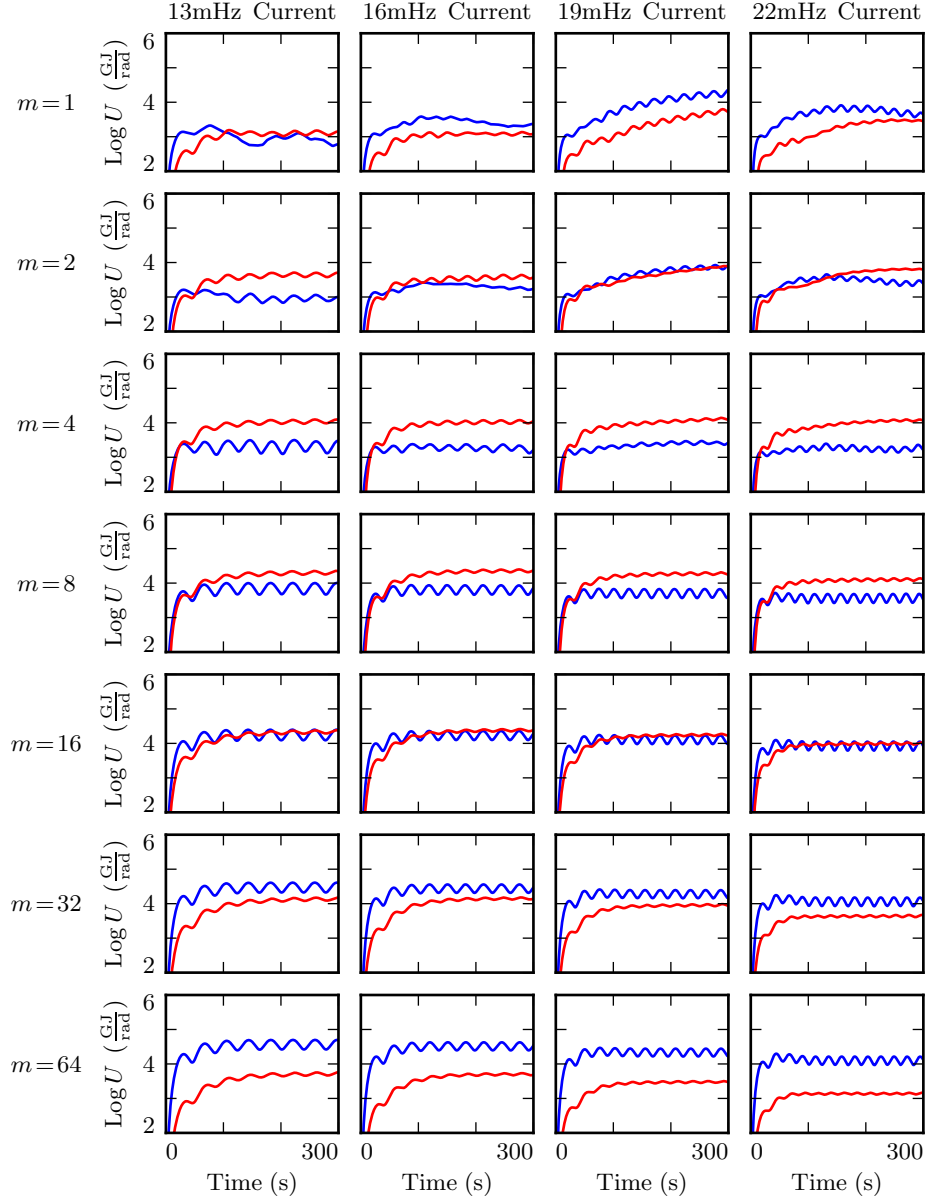


Figure 7.7: Even when the drive frequency does line up with the local Alfvén frequency, the low ionospheric conductivity prevents the accumulation of energy over the course of a large number of drive periods. Asymptotic energies are higher above than in analogous runs shown in Figure 7.6 — but compared to the dayside, the asymptotic energies are still small, and are still reached quickly.

1083 **7.4 Spatial Distribution of Energy: Nightside**

1084 Figure 7.8 shows the radial distribution of poloidal energy on the nightside — a slice of
1085 each run shown in Figure 7.7. Broadly speaking, the behavior is consistent with that
1086 seen in Section 7.2: energy is smeared across L -shells at small m and guided at high
1087 m , with particularly strong energy buildup when the drive frequency matches the local
1088 Alfvén frequency.

1089 As discussed in Section 7.3, the nightside’s relatively low ionospheric conductivity in-
1090 creases the rate of dissipation. Asymptotic energy content is reached quickly, and is
1091 small compared to that seen in analogous dayside runs.

1092 The effect is particularly pronounced at large modenumber, where the poloidal-to-
1093 toroidal rotation timescale is slower than the nightside dissipation timescale. In most
1094 of the dayside runs shown in Section 7.2, the toroidal mode asymptotically exceeds the
1095 poloidal mode both in terms of total energy content and in terms of peak energy density.
1096 On the nightside, the opposite is true. At high modenumber, the asymptotic rotation
1097 from the poloidal mode to the toroidal mode doesn’t occur until most of the energy has
1098 been lost to Joule dissipation. Peak poloidal energy densities at $m = 64$ exceed their
1099 toroidal counterparts — shown in Figure 7.9 — by an order of magnitude.

1100 **TODO:** On the nightside, unlike the dayside, toroidal contours are messy. Why?

Poloidal Energy Density by L-Shell: Active Night , $L_{PP} = 4$, $L_{drive} = 6$

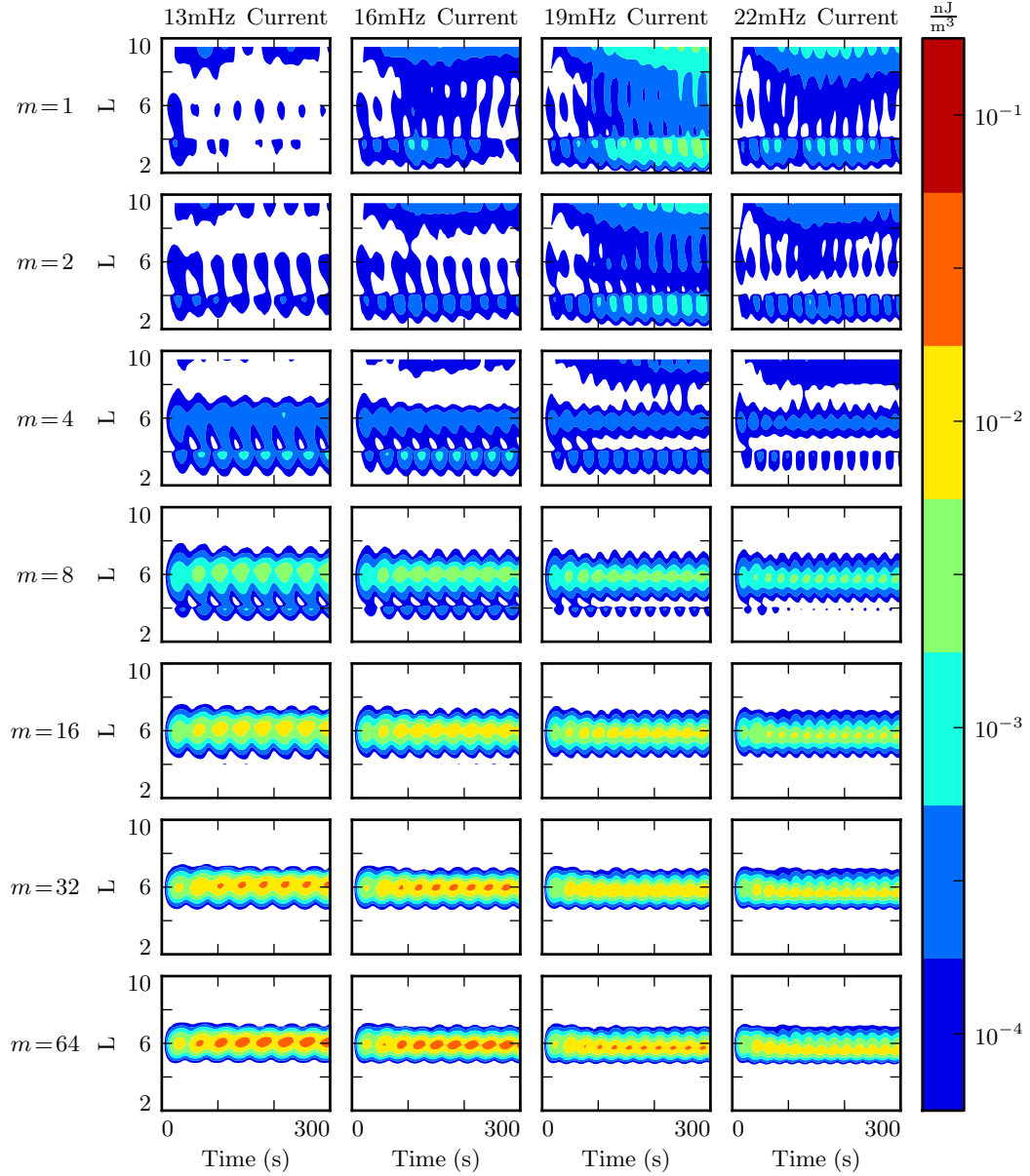


Figure 7.8: The behavior of the poloidal mode on the nightside matches qualitatively with the behavior on the dayside. At low m , energy is lost to the outer boundary. At high m , resonance occurs, but only if the drive frequency is close to the local eigenfrequency. The big difference is that, due to the increased dissipation in the ionosphere, asymptotic energy densities are relatively low, and reached relatively quickly.

Toroidal Energy Density by L-Shell: Active Night , $L_{PP} = 4$, $L_{drive} = 6$

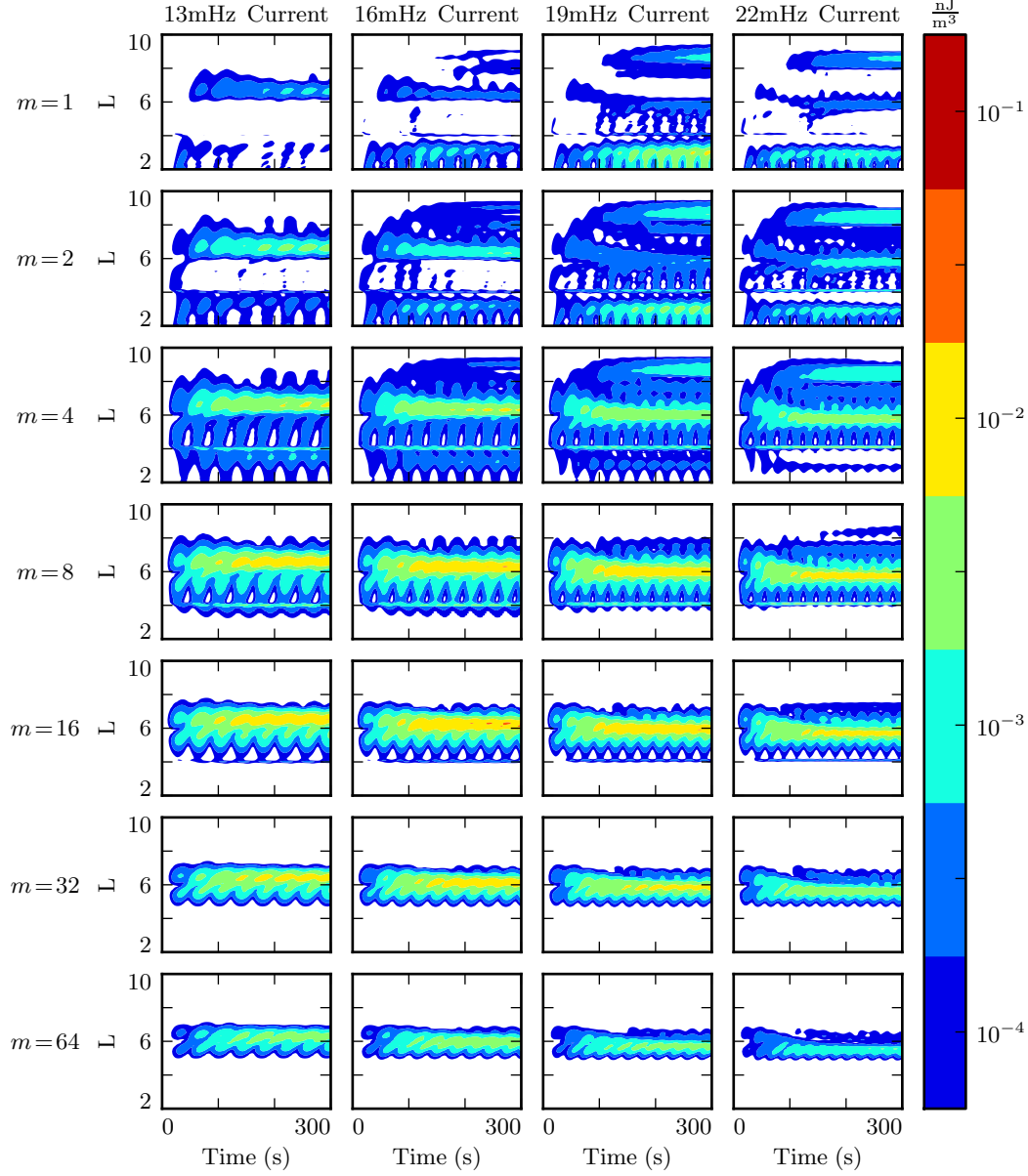


Figure 7.9: In low- m runs, the poloidal mode loses energy to the outer boundary, which impairs the growth of the toroidal mode. At high m , poloidal-to-toroidal rotation is slow compared to dissipative timescales on the nightside. The strongest toroidal waves — which are still weak compared to those on the dayside — thus appear at moderate m .

1101 7.5 Modenumber and Compressional Coupling

1102 The fact that the poloidal mode is compressional at low modenumber, but not at high
1103 modenumber, is well known. However, the relationship is not well quantified. Theoretical
1104 work has historically been focused on the limits $m \rightarrow 0$ and $m \rightarrow \infty$ [15, 79], and
1105 only a handful of satellite observations have explicitly considered an event's azimuthal
1106 modenumber[18, 71, 91].

1107 Figures 7.10 and 7.11 show the strength of the compressional magnetic field, as compared
1108 to the poloidal magnetic field, for two ensembles of runs. Each subplot in Figures 7.10
1109 and 7.11 corresponds to a run. Azimuthal modenumber is held constant across each
1110 row, and drive frequency is constant down each column.

1111 The runs shown in Figure 7.10 are carried out using the quiet dayside ionospheric
1112 profile. Similar runs using the active dayside and active nightside profiles give numbers
1113 that match closely. Using the quiet nightside profile, compressional coupling at high m
1114 is stronger by a factor of ~ 2 , as shown in Figure 7.11.

The quantity shown in Figures 7.10 and 7.11 is the ratio of the RMS compressional magnetic field to the RMS poloidal magnetic field:

$$\text{TODO: name?} = \sqrt{\frac{\int dV B_z^2}{\int dV B_x^2}} \quad (7.2)$$

1115 The dotted lines indicate the mean, which is listed at the top of each subplot.

1116 At $m = 1$, when the cutoff frequency³ is well below the drive frequency, the compressional and poloidal wave magnetic fields are (on average) equally strong. As m increases, the poloidal mode's compressional propagation becomes constrained, and the compressional magnetic field weakens. The compressional magnetic field's relative magnitude is cut in half by $m \sim 5$ (for non-quiet-night profiles), and cut in half again by $m \sim 10$. (Using the quiet night profile, the strength is instead halved at $m \sim 7$ and quartered at $m \sim 14$).

³See Figure 4.1.

- 1123 TODO: The nature of the relationship between m and the compressional coupling is not
 1124 obvious. It's not linear, logarithmic, or a power law. When the compressional magnetic
 1125 field is compared to the total wave magnetic field ($\sqrt{B_x^2 + B_y^2 + B_z^2}$) instead of to the
 1126 poloidal magnetic field, the pattern remains unclear.
- 1127 TODO: These results line up nicely with Dai's 2015 survey of poloidal Pc4 events[17].
 1128 Events are characterized as compressional or non-compressional based on the ratio $\left| \frac{B_z}{B_x} \right|$.
 1129 The threshold is arbitrarily set to 0.2 — with no suggestion of a corresponding value of
 1130 m . The results in Figure 7.10 suggest that Dai's threshold (conveniently!) aligns closely
 1131 with the paper's definition of “small m ” to mean $m < 10$.
- 1132 TODO: Check if a relationship is given in Hughes[43]. That's what Lei cites for “low- m
 1133 waves are compressional.” Other papers give no indication that this has been looked at
 1134 before[15, 79].
- 1135 TODO: Results might vary significantly for even modes. Radoski's 1974 paper suggests
 1136 that $\left| \frac{B_z}{B_x} \right| \sim \frac{1}{n}$ (where n is the harmonic number).
- 1137 TODO: There's a bit of frequency dependence in the compressional coupling. Higher-
 1138 frequency runs are more compressional. This is presumably because higher-frequency
 1139 runs are closer to the compressional cutoff, so they are not quite as evanescent in the
 1140 compressional direction.
- 1141 TODO: Sawtooth shape — the compressional magnetic field is pumped up by the driv-
 1142 ing, but drops quickly since compressional propagation is evanescent.

RMS Compressional Coupling to the Poloidal Mode: Quiet Day

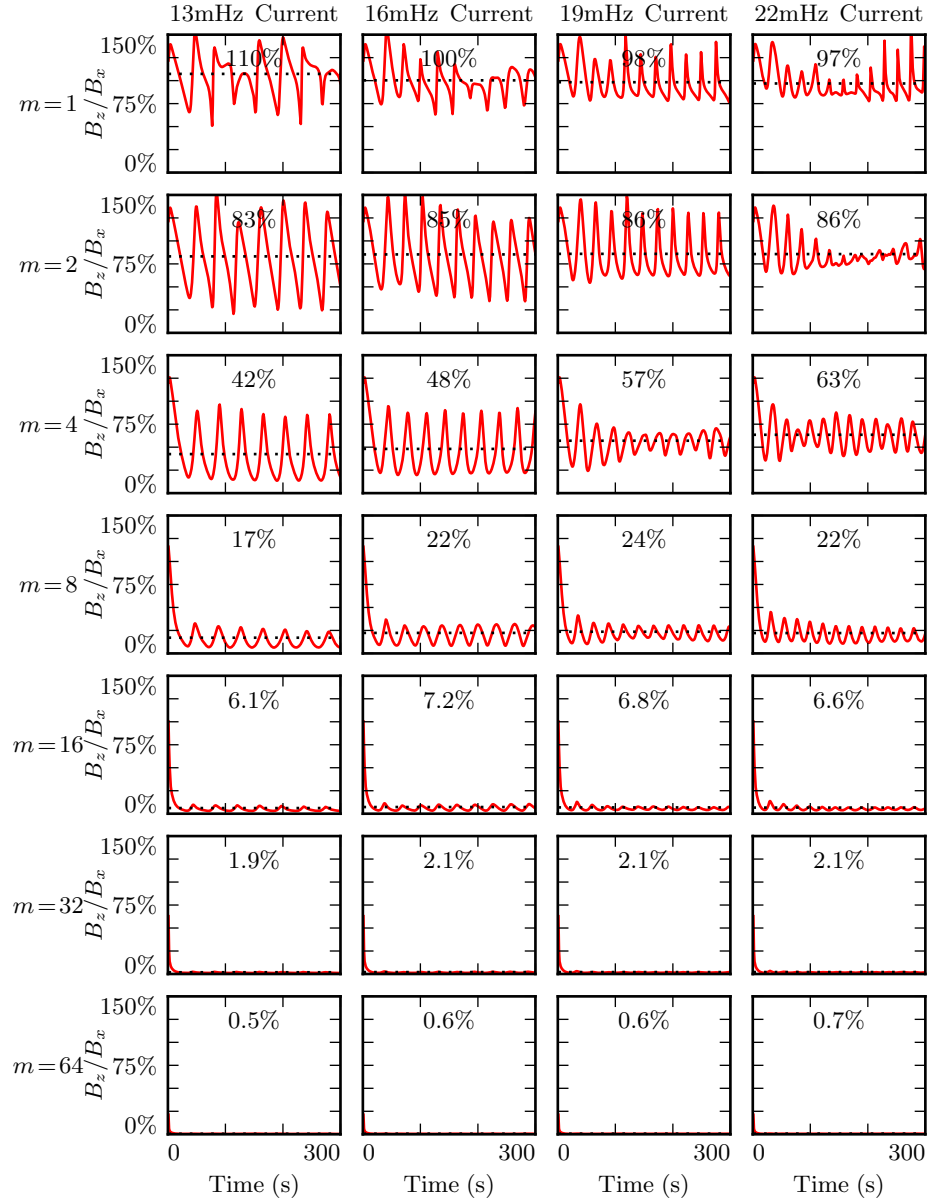


Figure 7.10: **TODO: ...**

RMS Compressional Coupling to the Poloidal Mode: Quiet Night

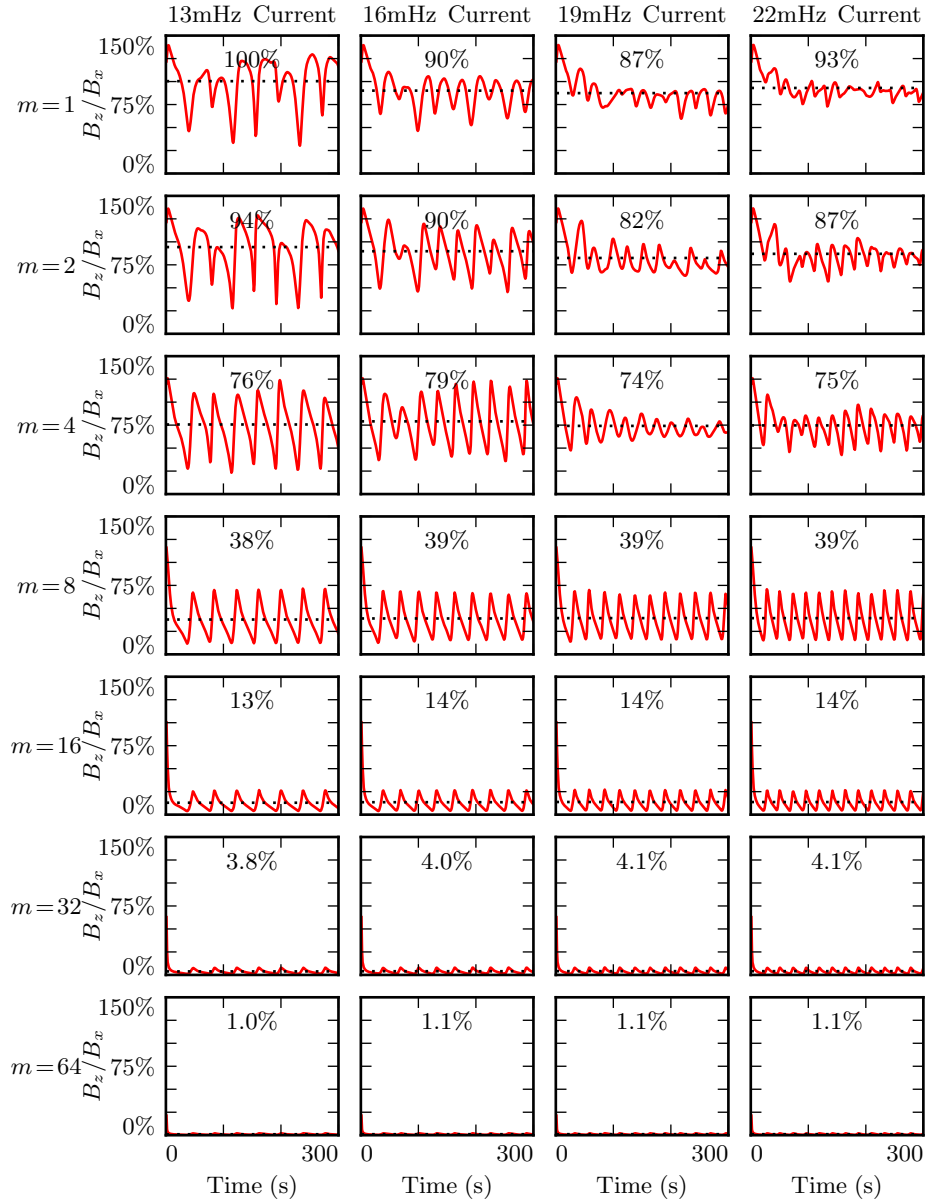


Figure 7.11: TODO: The other three models give comparable compressional couplings. Oddly, the quiet night profile gives twice as much.

1143 7.6 Ground Signatures and Giant Pulsations

1144 While the majority of the action is in space, the majority of FLR observations have
1145 been ground-based. The present section explores the same simulations discussed in
1146 Sections 7.1 to 7.4, but in terms of their ground signatures rather than their broad
1147 energy distributions.

1148 As in the figures shown in Sections 7.1 to 7.4, each row in Figures 7.12 and 7.13 shows
1149 runs at a different modenumber. The columns are magnetic field contours; the vertical
1150 axis is latitude, and the horizontal axis is time. The four columns are components of
1151 the magnetic field signatures at the ground: the north-south magnetic field (first and
1152 third columns) and the east-west magnetic field (second and fourth columns). The pair
1153 on the left show a simulation carried out using the active ionospheric profile, and the
1154 pair on the right show a simulation using the quiet profile.

1155 Notably, the magnetic polarization of a low frequency Alfvén wave is rotated by $\sim 90^\circ$ as
1156 it passes through the ionosphere[42]. The east-west field on the ground (B_ϕ) corresponds
1157 to the poloidal polarization in space, and the north-south field on the ground (B_θ)
1158 corresponds to the toroidal mode.

1159 **TODO:** What's going on with the empty frame for nightside, $m = 1, 16\text{ mHz}$?

1160 **TODO:** Don't use 19 mHz! It's wonky at low modenumber. Use 22 mHz instead.

1161 The most striking feature of Figures 7.12 and 7.13 is the modenumber dependence.
1162 As modenumber increases, the magnetic field signatures become sharply localized in
1163 latitude. At high m , ground signatures are concentrated between 60° and 70° , peaking
1164 just below 65° . This shows good agreement with observations of Pgs peaked near 66° .

1165 At low modenumber, magnetic signatures are weak on the ground because the waves
1166 in space are also weak. At high modenumber, waves in space are strong, but so is
1167 the attenuation of magnetic signatures by the ionosphere⁴. The “sweet spot” at which
1168 magnetic ground signatures are maximized falls at $m = 16$ to $m = 32$. For comparison,
1169 Pgs are generally observed with azimuthal modenumbers of 16 to 35[93].

⁴See Equation (3.2).

1170 Ground signatures are maximized at $m = 16$ and $m = 32$ on both the dayside (Figure
1171 7.12) and the nightside (Figure 7.13). Dayside signatures are stronger than those on
1172 the nightside, and quiet dayside and quiet nightside responses are stronger than those
1173 on the active dayside and active nightside respectively. The strongest magnetic fields
1174 at the ground are primarily east-west polarized – as Pgs are[93].

1175 TODO: At present, Tuna's ionospheric profiles do not allow the dawn and dusk flanks
1176 to be distinguished from the dayside and nightside.

Magnetic Ground Signatures: 22mHz Current , $L_{PP} = 4$, $L_{drive} = 5$

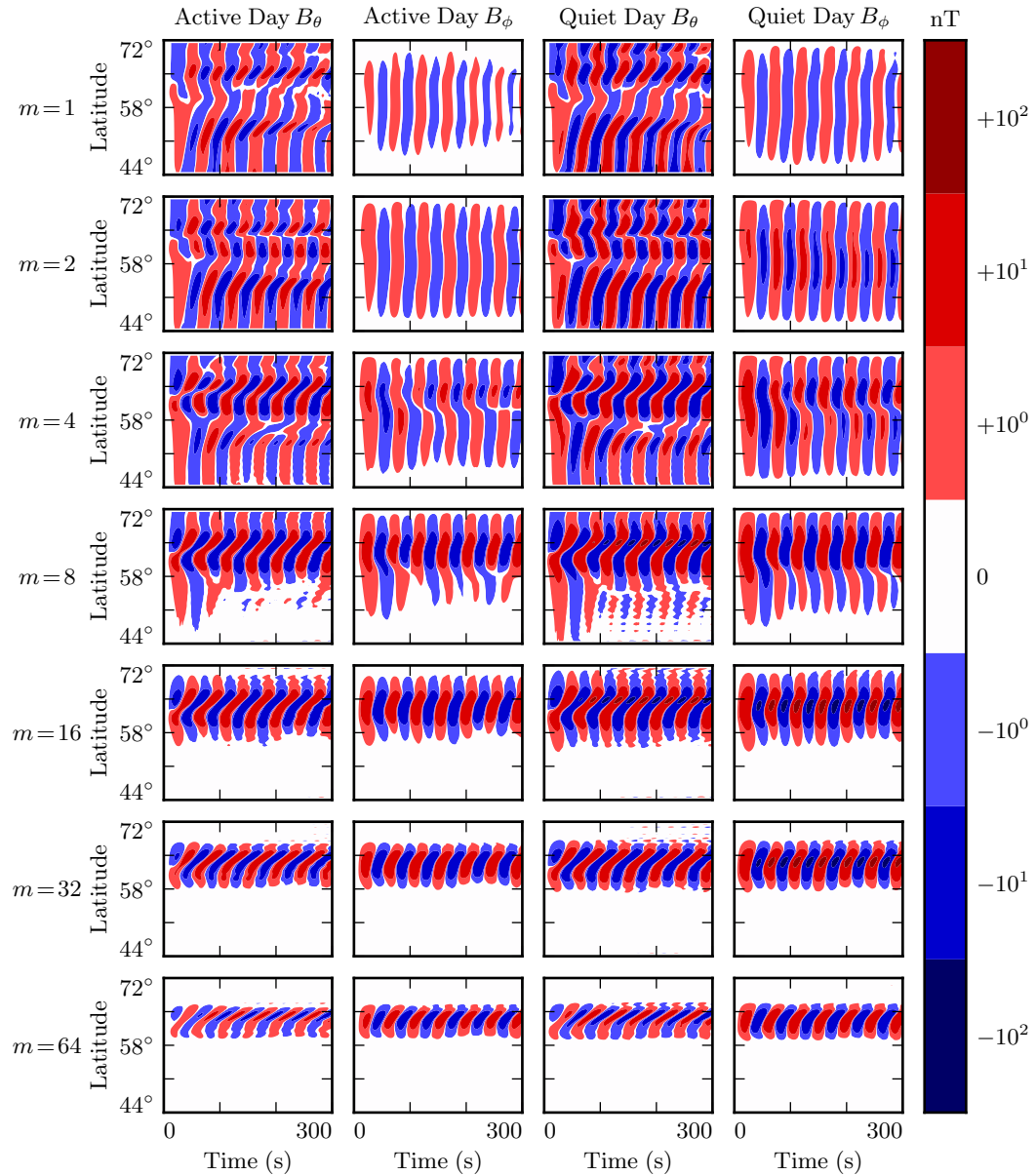


Figure 7.12: TODO: Use 22 mHz instead! At 19 mHz and low m , there's something weird happening at the outer boundary.

Magnetic Ground Signatures: 16mHz Current , $L_{PP} = 4$, $L_{drive} = 5$

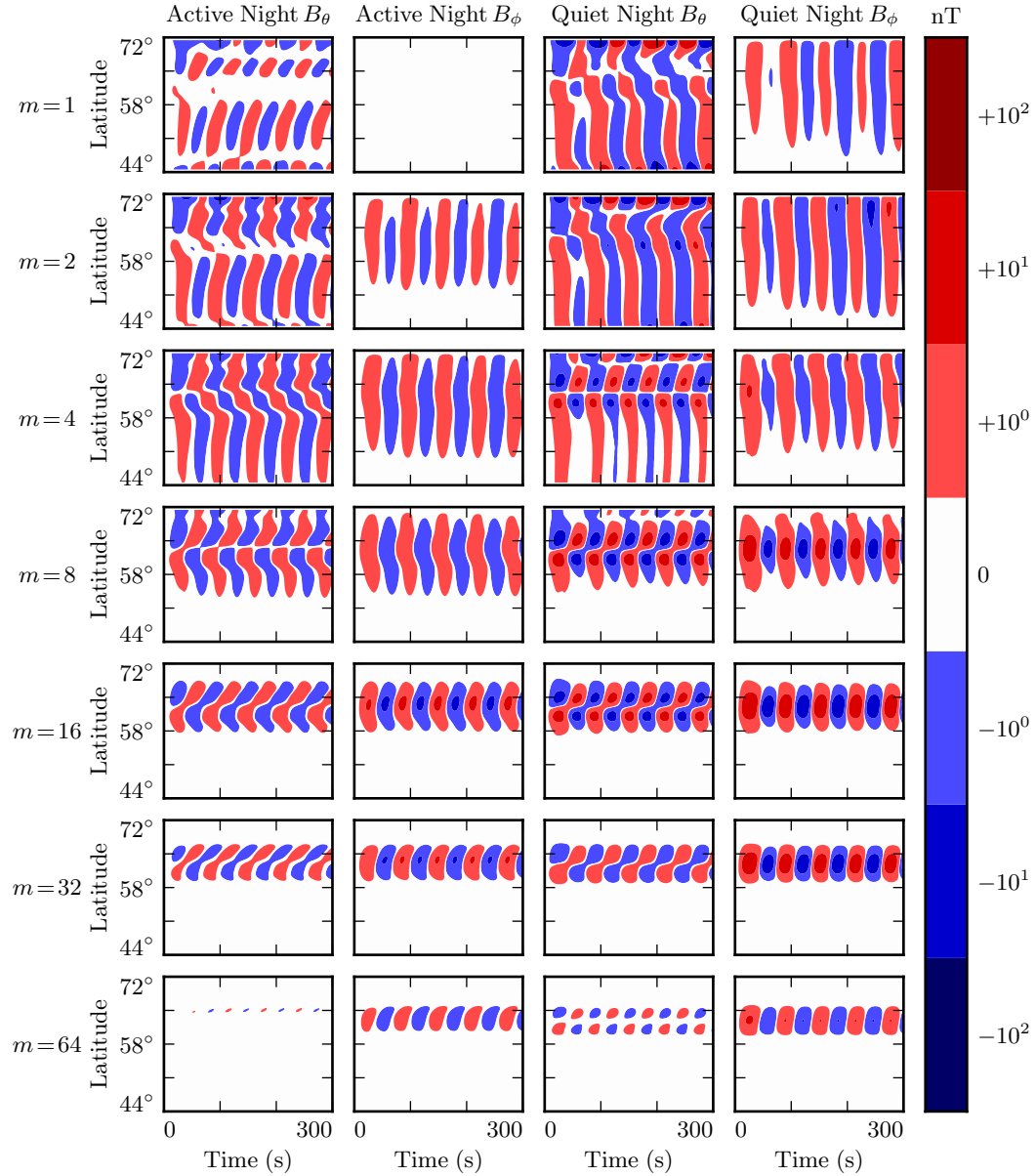


Figure 7.13: Nightside ground signatures are less strongly peaked than those on the dayside, but qualitative features are the same: the strongest signals are in B_ϕ , peaked over just a few degrees in latitude, at a modenumber of 16 or 32, under quiet ionospheric conditions.

1177 **7.7 Discussion**

1178 **TODO:** Make this section read nicely.

1179 Poloidal FLRs rotate to the toroidal mode over time. Toroidal modes do not appear to
1180 rotate back to the poloidal mode. When m is small, the rotation is comparable to an
1181 oscillation period; when m is large, rotation timescales are comparable to ten periods,
1182 sometimes more.

1183 On the dayside, little damping takes place over rotation timescales, so the toroidal mode
1184 asymptotically exceeds the toroidal mode. The exception is waves with low modenumber,
1185 where poloidal waves can escape by propagating across field lines. An evaluation
1186 of what happens then — whether they bounce back off the magnetopause, for example
1187 — is beyond the scope of the present work.

1188 On the nightside, the conductivity of the ionosphere is low enough that damping
1189 timescales become comparable to oscillation timescales. Waves are weaker, since they
1190 are unable to accumulate energy over as many periods. High- m toroidal waves are
1191 particularly weak, since the dissipation timescale is faster than the poloidal-to-toroidal
1192 rotation timescale.

1193 Waves resonate best when the frequency of the driving matches the local eigenfrequency
1194 where it's delivered. The eigenfrequency is significantly affected by the size of the
1195 plasmasphere.

1196 The poloidal mode, due to its compressional character, exhibits an energy profile which
1197 is smeared in L . The toroidal mode, on the other hand, forms sharp resonances where the
1198 drive frequency matches the local eigenfrequency. This may explain why the observed
1199 frequencies of poloidal waves depend weakly on L , while the frequencies of toroidal
1200 waves are strongly dependent on L .

1201 At low m , ground signatures are weak because waves in space are weak because energy
1202 can easily escape through the simulation's outer boundary. At large m , ground signatures
1203 are attenuated by the ionosphere. The “sweet spot” in azimuthal modenumber at
1204 which ground signatures are strongest is around 16 to 32. Furthermore, ground signatures
1205 are strongest when ionospheric profiles corresponding to solar minimum are used.

1206 Driving in the poloidal electric field gives rise to primarily ground signatures polarized
1207 primarily in the east-west direction at the ground. And, when the frequency of the
1208 driving does not match the local eigenfrequency, the high- m resonates weakly in place,
1209 rather than tunneling across field lines to resonate strongly somewhere else.

1210 These findings imply, awkwardly, that the morphology of giant pulsations may reveal
1211 relatively little about their origins. One can consider a hypothetical magnetosphere
1212 subject to constant driving: broadband in frequency, broadband in modenumber, just
1213 outside the plasmapause. Low- m poloidal waves will quickly rotate to the toroidal mode
1214 (and/or propagate away). High- m waves will resonate in place, accumulating energy
1215 over time, and giving rise to “multiharmonic toroidal waves”[90]; Fourier components
1216 that do not match the local eigenfrequency will quickly asymptote. Waves with very high
1217 modenumbers will be attenuated by the ionosphere. The response on the ground will be
1218 significantly stronger during quiet solar conditions. In other words, the measurements
1219 on the ground will look very much like a giant pulsation.

1220 **TODO:** Notably, the present work offers no explanation as to Pgs’ distinctive distribu-
1221 tion in MLT!

1222 **Chapter 8**

1223 **Observations**

1224 TODO: You know what would be great for putting this numerical work in context?

1225 A nice, consistent survey that breaks down the occurrence rate of Pc4 pulsations by
1226 harmonic, etc.

1227 TODO: The tools used in the present chapter — SPEDAS and the SPICE kernel —
1228 are publicly available. They run best with an IDL license, which is not, but they are
1229 functional using just the (free) IDL virtual machine. The code is wrapped up in a Git
1230 repository: <https://github.com/chizarlicious/RBSP> (maybe should make a GitHub
1231 organization to hold this code, to decouple it from my personal account?).

1232 Previous work:

1233 Dai[17] used RBSP to look at poloidal Pc4 events, with a bias in favor of the second
1234 harmonic — 890 events. Events are most common near noon, but are spread across the
1235 day and dusk side, with a few stragglers at midnight.

1236 Anderson[3] used AMPTE/CCE (mostly $L > 7$, near the equator) to look at Pc4 events
1237 — 7000 hours. Limited commentary on parity. Toroidal modes were found to outnumber
1238 poloidal modes three-to-one. “Harmonic toroidal resonances” are spread 0600 to 1600.
1239 “Fundamental toroidal resonances” (which are not mutually exclusive with harmonic
1240 ones!) appear everywhere but dusk.

1241 Liu[57] used THEMIS (equatorial orbit, L out to ~ 10) to look at both poloidal and
1242 toroidal modes — 9805 one-minute Pc4 events (?). No commentary on parity. Poloidal
1243 events are most common at noon (with another peak post-midnight) and strongest
1244 on the dusk side. Toroidal events are most common from pre-dawn to pre-noon and
1245 strongest pre-midnight and post-dawn.

1246 Kokubun[53] used ATS6 (synchronous orbit) — ~ 150 events. No commentary on har-
1247 monic. Toroidal events dominate in the dawn sector. Poloidal events are spread across
1248 all MLT, with a peak in the early afternoon and Pgs in the early morning.

1249 Motoba[71] used GOES13 and GOES15 (geosynchronous) to look specifically at Pgs —
1250 105 events. Seen from midnight to noon, with a strong peak before dawn, 0300 or so.

1251 8.1 Sampling Bias and Event Selection

1252 The present analysis makes use of all available Van Allen Probe data, which spans from
1253 October 2012 to August 2015. Between the two probes, that's just over 2000 days of
1254 observation.

1255 For the purposes of Pc4 pulsations, it's reasonable to consider the two probes to be
1256 independent observers. Nearly all Pc4 events occur near apogee ($L \gtrsim 5$), at which
1257 point the two probes are several hours apart in MLT. Pc4 events are typically not large
1258 enough to be seen by both probes simultaneously, and not long enough in duration to
1259 be seen by two probes passing through the same region of space several hours apart.

1260 **TODO:** Quantify how often an event is seen by both probes?

1261 Electric and magnetic field waveforms are collected using the probes' **TODO: ...** in-
1262 strument. Values are cleaned up by averaging over the ten-second spin period. Three-
1263 dimensional electric field data is then obtained using the $\underline{E} \cdot \underline{B} = 0$ assumption. Notably,
1264 this assumption is taken only when the probe's spin plane is offset from the magnetic
1265 field by at least 15° . The rest of the data — about half — is discarded, which introduces
1266 a sampling bias against the flanks.

1267 A further bias is introduced by the probes' non-integer number of precessions around
 1268 Earth. As of July 2014, apogee had precessed once around Earth[17]. The present work
 1269 considers roughly one and a half precessions; the nightside has been sampled at apogee
 1270 twice as often as the dayside.

1271 The spatial distribution of usable data — that is, data for which three-dimensional
 1272 electric and magnetic fields are available — is shown in Figure 8.1. Bins are unitary
 1273 in L and in MLT. Event distribution in magnetic latitude is not shown; the Van Allen
 1274 Probes are localized to within $\sim 10^\circ$ of the equatorial plane.

1275 **TODO: L is italicized and MLT is not? That seems weird.**

1276 Field measurements are transformed from GSE coordinates into the same dipole coor-
 1277 dinates used in Chapters 5 and 7. The z axis is parallel to the background magnetic
 1278 field, which is estimated using a ten-minute running average of the magnetic field mea-
 1279 surements. The y axis is defined per $\hat{y} \parallel \hat{z} \times \underline{r}$. The x axis is then defined per $\hat{x} \equiv \hat{y} \times \hat{z}$.
 1280 This scheme guarantees that the axes are right-handed and pairwise orthogonal[57].

1281 The ~ 1000 days of usable data are considered half an hour at a time, which gives a fre-
 1282 quency resolution of ~ 0.5 mHz in the discrete Fourier transform. Spectra are computed
 1283 for all six field components: \tilde{B}_x , \tilde{B}_y , \tilde{B}_z , \tilde{E}_x , \tilde{E}_y , and \tilde{E}_z . The background magnetic
 1284 field is subtracted before transforming the magnetic field components, leaving only the
 1285 perturbation along each axis¹. Each waveform is also shifted horizontally so that its
 1286 mean over the thirty minute event is zero.

Frequency-domain Poynting flux is computed from the electric and magnetic field trans-
 forms. A factor of L^3 compensates the compression of the flux tube, so that the resulting
 values are effective at the ionosphere. Poloidal and toroidal Poynting flux, respectively,
 are given by:

$$\tilde{S}_P \equiv -\frac{L^3}{\mu_0} \tilde{E}_y \tilde{B}_x^* \quad \tilde{S}_T \equiv \frac{L^3}{\mu_0} \tilde{E}_x \tilde{B}_y^* \quad (8.1)$$

¹As in Chapters 5 and 7, B_x refers not to the full magnetic field in the x direction, but to the perturbation in the x direction from the zeroth-order magnetic field.

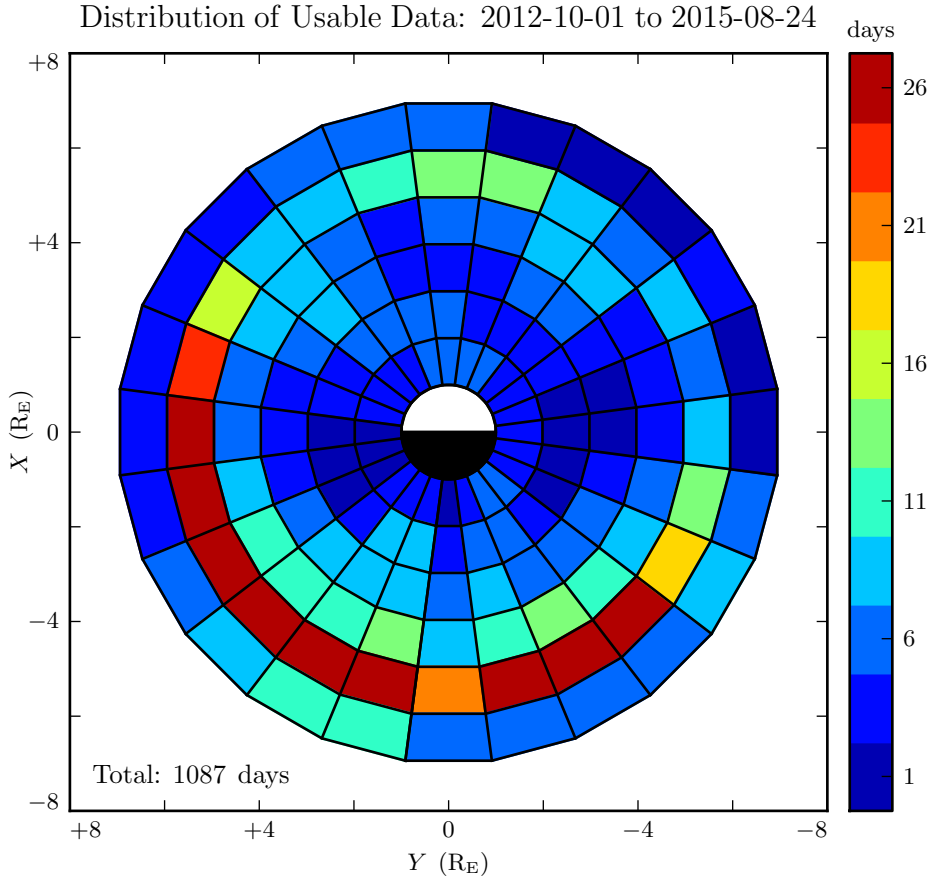


Figure 8.1: Three-dimensional electric field values are computed by assuming $\underline{E} \cdot \underline{B} = 0$. Data is discarded whenever the magnetic field falls within 15° of the spin plane, which introduces a bias against the flanks. Furthermore, the probes have completed one and a half precessions around Earth; the dayside has been sampled once at apogee, and the nightside twice.

1287 The poloidal and toroidal channels are independently checked for Pc4 waves. For each
 1288 channel, a Gaussian profile is fit to the magnitude of the Poynting flux, $|\tilde{\mathcal{S}}(\omega)|$. If the
 1289 fit fails to converge, or if the peak of the Gaussian does not fall within 5 mHz of the
 1290 peak value of $\tilde{\mathcal{S}}$, the event is discarded. Events are also discarded if their frequencies
 1291 fall outside the Pc4 frequency range (7 mHz to 25 mHz) or if their amplitudes fall below
 1292 10^{-2} mW/m² (out of consideration for instrument sensitivity).

1293 Events are discarded if their parity is ambiguous. The electric field and the magnetic
1294 field must be coherent at a level of 0.9 or better (judged at the discrete Fourier transform
1295 point closest to the peak of the Gaussian fit). Any event within 3° of the magnetic
1296 equator is also not used; as discussed in Chapter 3, in order to distinguish an odd mode
1297 from an even mode, it's necessary to know whether the observation is made north or
1298 south of the equator.

1299 **TODO:** How much time do the probes spend within 3° of the magnetic equator?

1300 Notably, events are not filtered based on the width of their spectra or on the division of
1301 their energy between standing and traveling modes. These two parameters are discussed
1302 in Section 8.6 and Section 8.5 respectively.

1303 **TODO:** First and third harmonics can only be distinguished by guessing at the fre-
1304 quency. Chisham and Orr[14] argue that around $7R_E$, frequency around 10 mHz pre-
1305 cludes higher harmonics. Or maybe look at [35]?

1306 **TODO:** Are we biased in terms of Dst? What's the distribution look like for the good
1307 data and for the bad data?

1308 8.2 Rate of Pc4 Events

1309 The filters described in Section 8.1 yield 840 Pc4 events, the spatial distribution of
1310 which is shown in Figure 8.2. In each bin, the event count is normalized to the amount
1311 of usable data, per Figure 8.1. Bins shown in white contain zero events.

1312 Consistent with previous work, Pc4 events are rarely observed at $L < 4$. Nearly 30 %
1313 of the usable data shown in Figure 8.1 is located inside $L = 4$, yet that data accounts
1314 for only 18 of the 840 events.

1315 **TODO:** Dai thinks that Pc4 pulsations are common inside the plasmasphere. He uses
1316 the plasma number density gradient to estimate the plasmapause location. We use
1317 Scott's method, which is a cutoff of $100 / \text{cm}^3$. We find basically no events inside the
1318 plasmapause — only 43 out of 840.

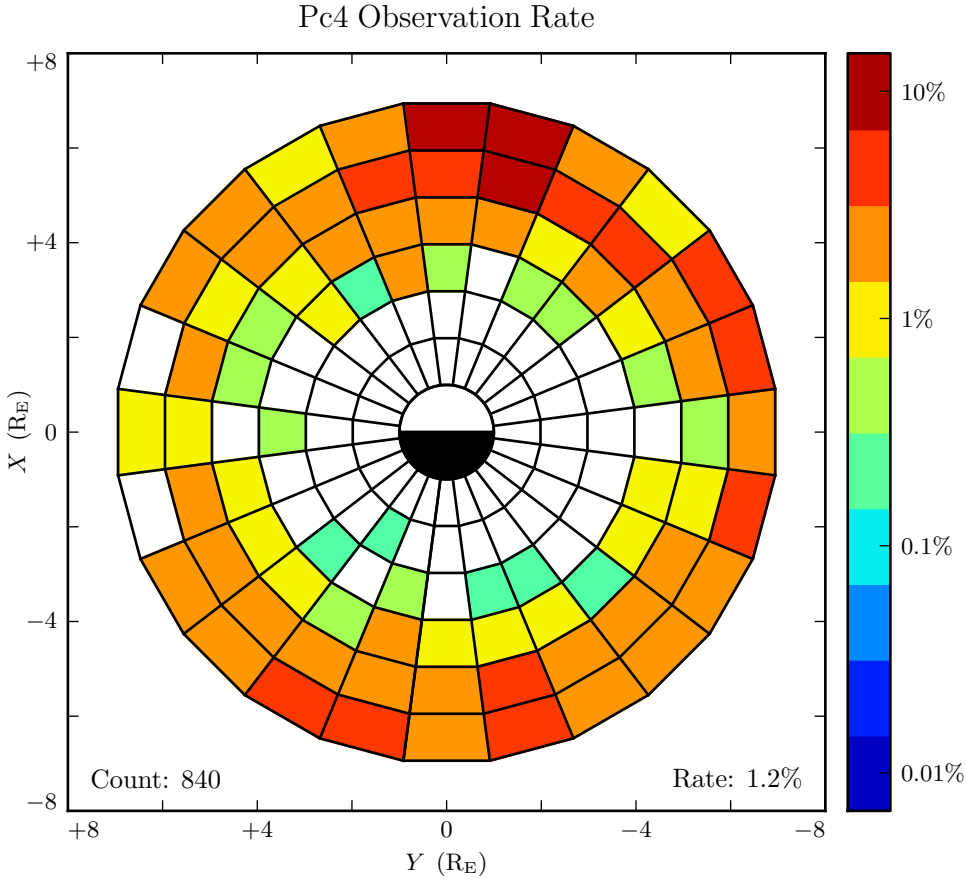


Figure 8.2: The above figure shows the spatial distribution of all 840 observed Pc4 events. Counts are normalized by the amount of usable data in each bin. The value in the bottom-right corner is the mean of the rate in each bin; it's an estimate of how often Pc4 events would be observed if the sampling were distributed uniformly in space. Events where the poloidal and toroidal channel trigger simultaneously ($\sim 10\%$ of cases) are counted as only a single event. Bins shown in white contain zero events.

1319 In Figure 8.3, events are partitioned by parity and polarization, yielding 141 odd poloidal
 1320 events, 237 even poloidal events, 457 odd toroidal events, and 87 even toroidal events
 1321 — a total of 922 events. The total is greater than 840 because in $\sim 10\%$ of events, the
 1322 poloidal and toroidal channels trigger independently. Such cases count as only a single
 1323 event in Figure 8.2, but the toroidal and poloidal events are both shown in Figure 8.3.

1324 TODO: Even poloidal events and even toroidal events are distributed similarly, which is
1325 good to see, since even poloidal events give rise to even toroidal events. The relationship
1326 is less clear for odd events, though odd poloidal modes and odd toroidal modes are both
1327 least common at dusk.

1328 TODO: Odd toroidal events are by far the most commonly observed. Oddly, even
1329 poloidal events are the least common.

1330 TODO: Even modes are less likely to be observed on the ground? [93]

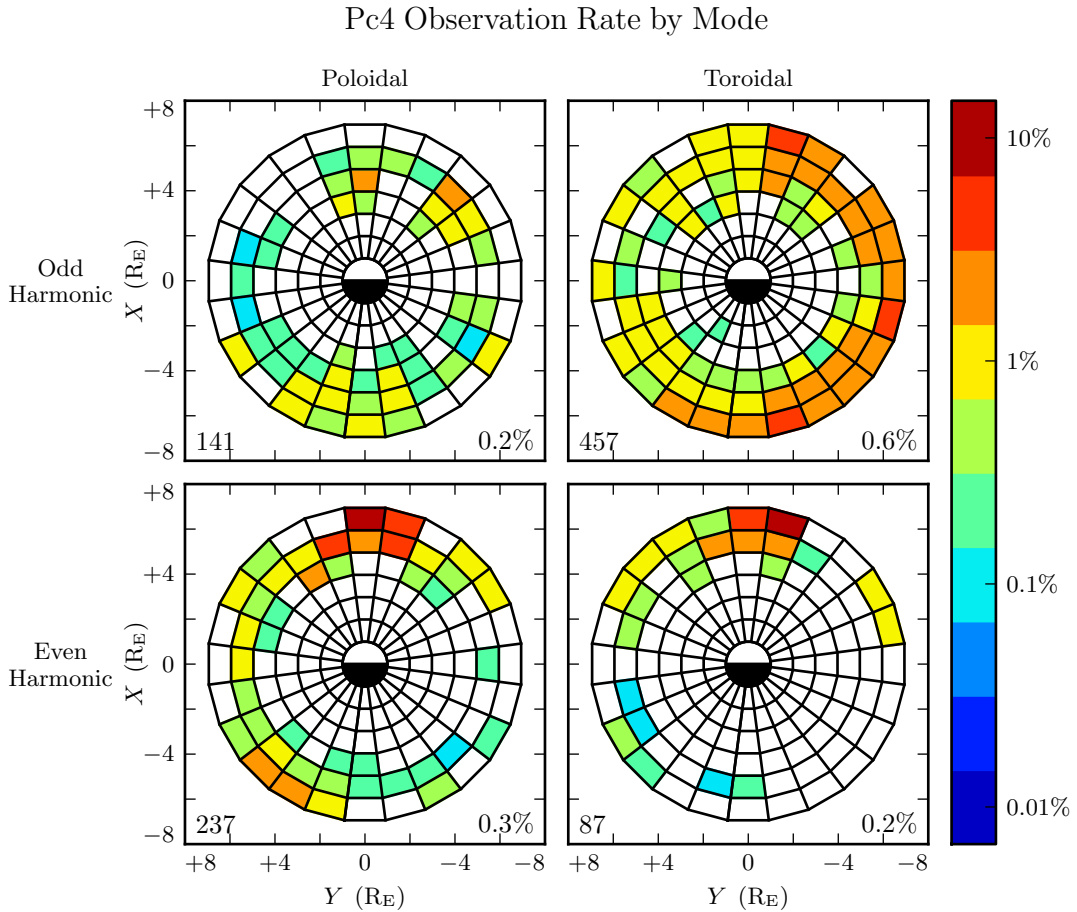


Figure 8.3: The above figure shows the spatial distribution for the same 840 events shown in Figure 8.2, partitioned by polarization and parity. The selection criteria described in Section 8.1 ensure that both properties are known for all events. Event counts are normalized by the time spent by the amount of usable data in each bin. Event counts do not sum to 840 because some events trigger on both the poloidal channel and the toroidal channel. Bins shown in white contain zero events.

1331 8.3 Rate of Pc4 Events by Amplitude

Amplitude Distribution of Pc4 Events by Mode

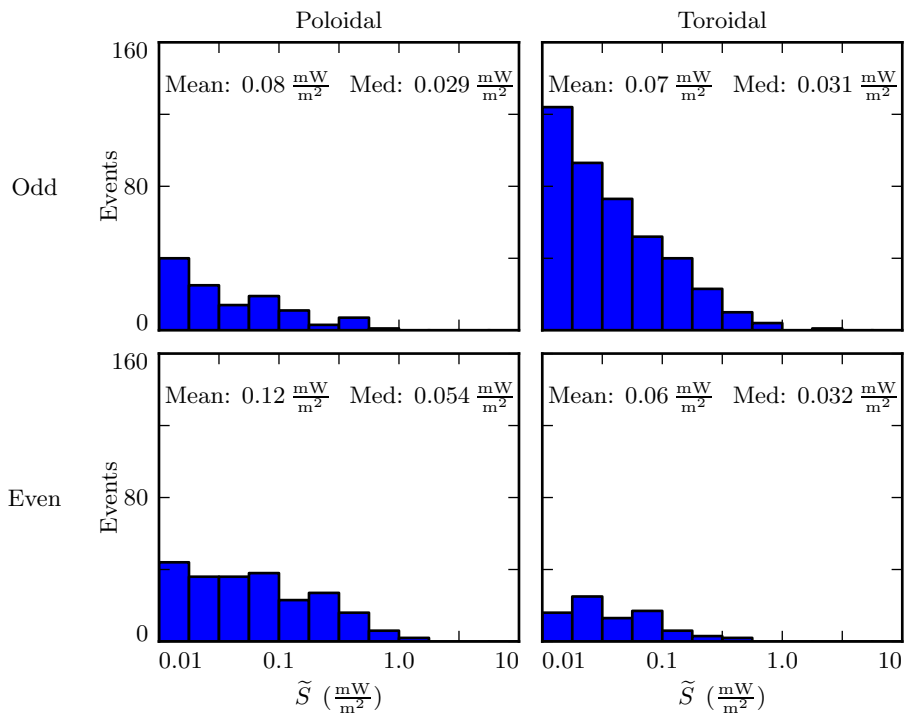


Figure 8.4: TODO: ...

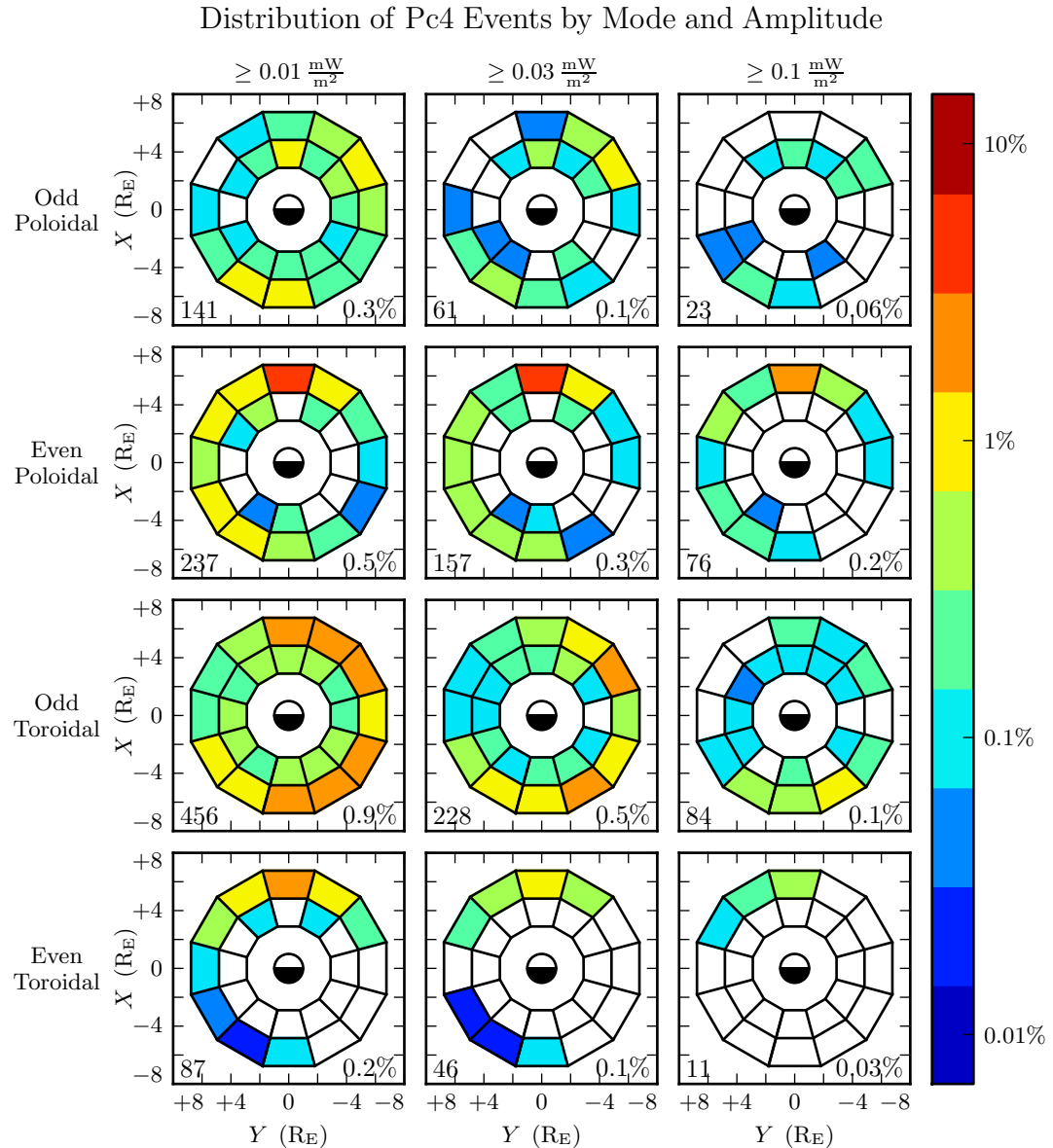


Figure 8.5: TODO: ...

₁₃₃₂ 8.4 Rate of Pc4 Events by Frequency

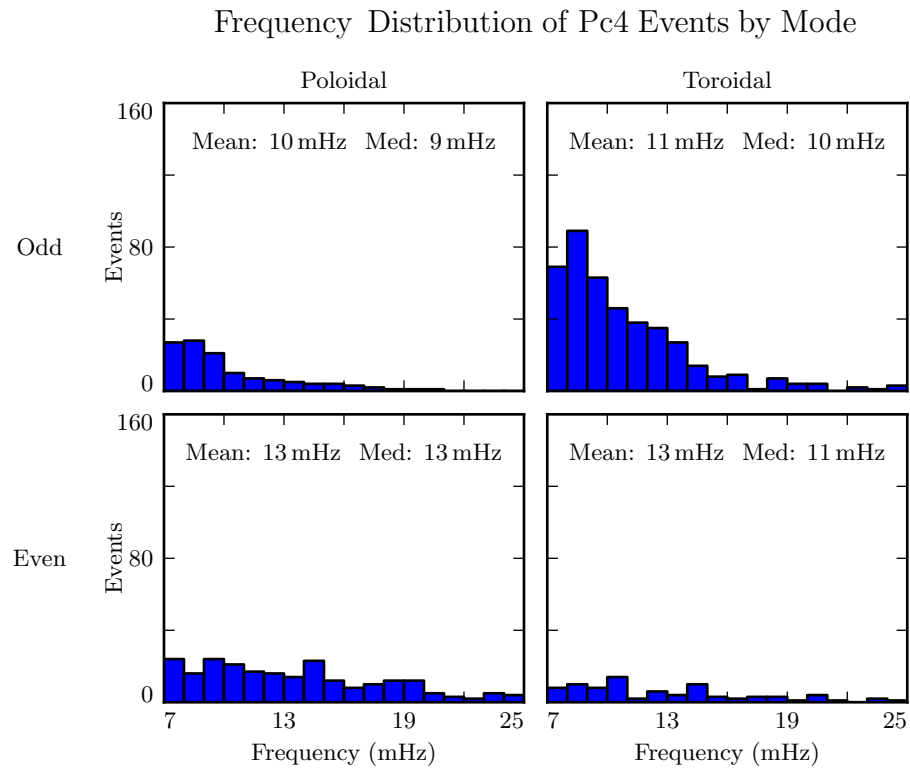


Figure 8.6: TODO: ...

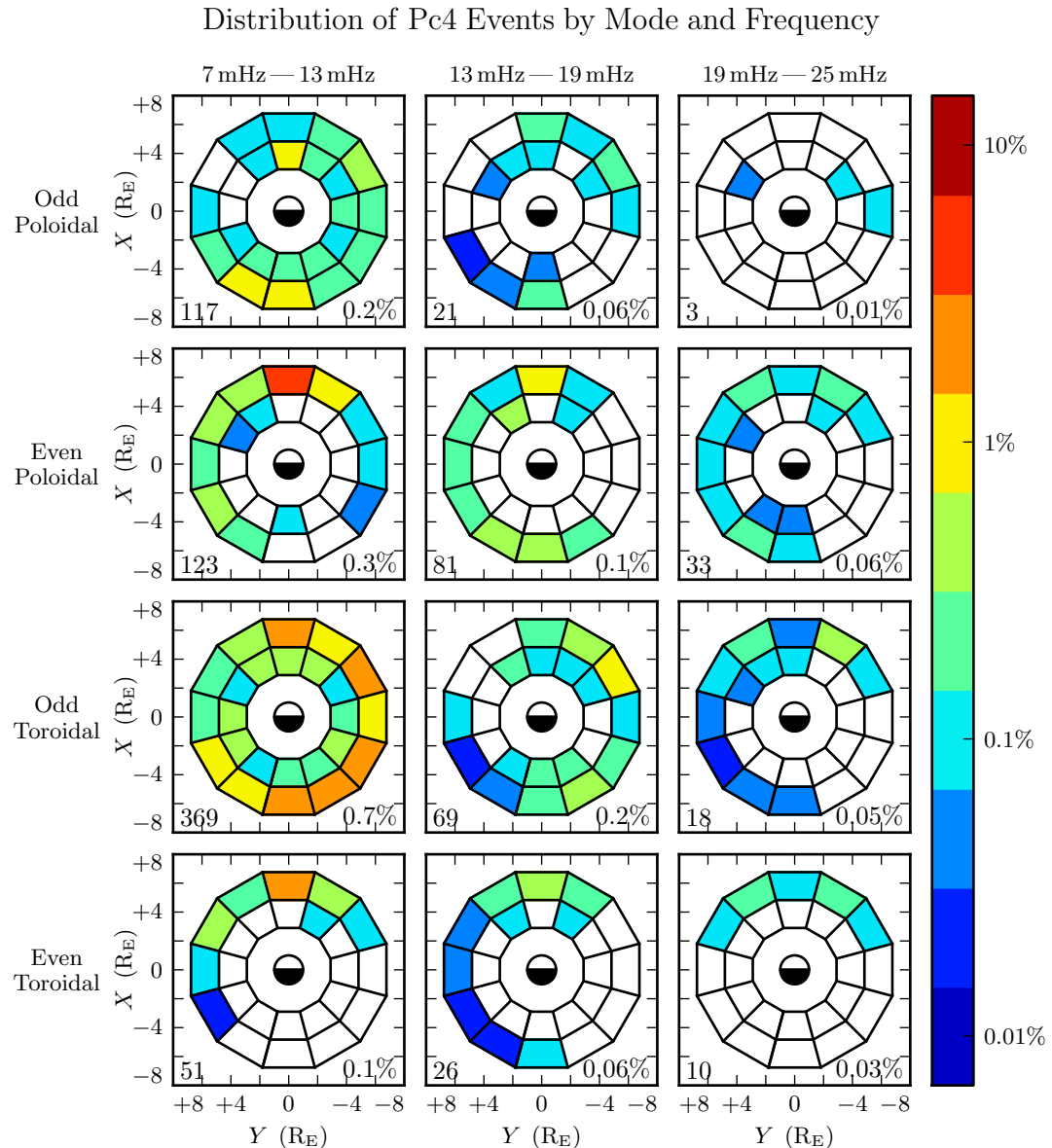


Figure 8.7: TODO: ...

₁₃₃₃ 8.5 Rate of Pc4 Events by Phase

Phase Distribution of Pc4 Events by Mode

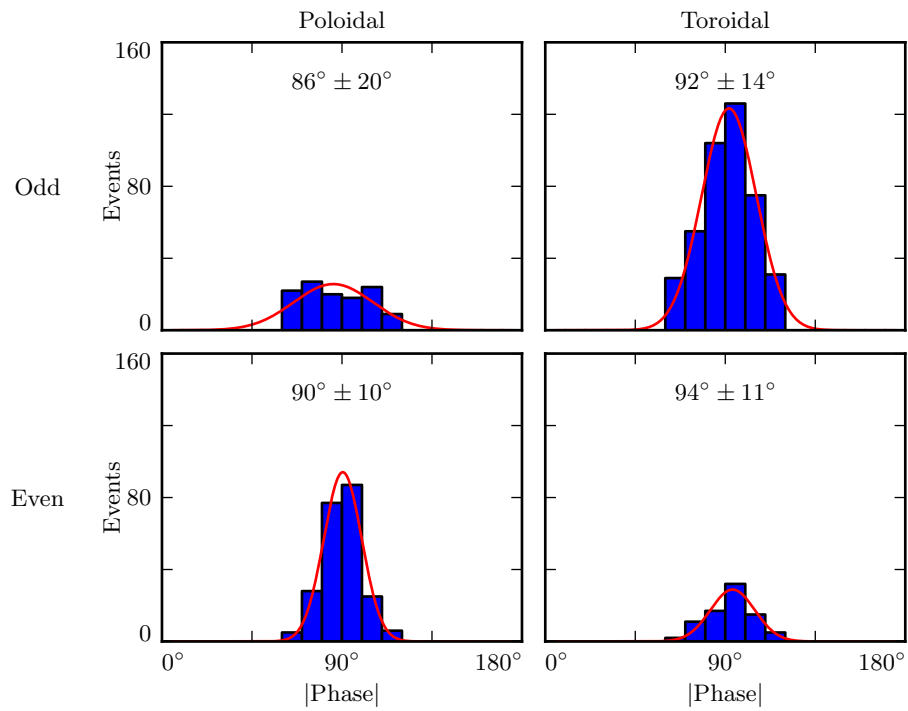


Figure 8.8: TODO: ...

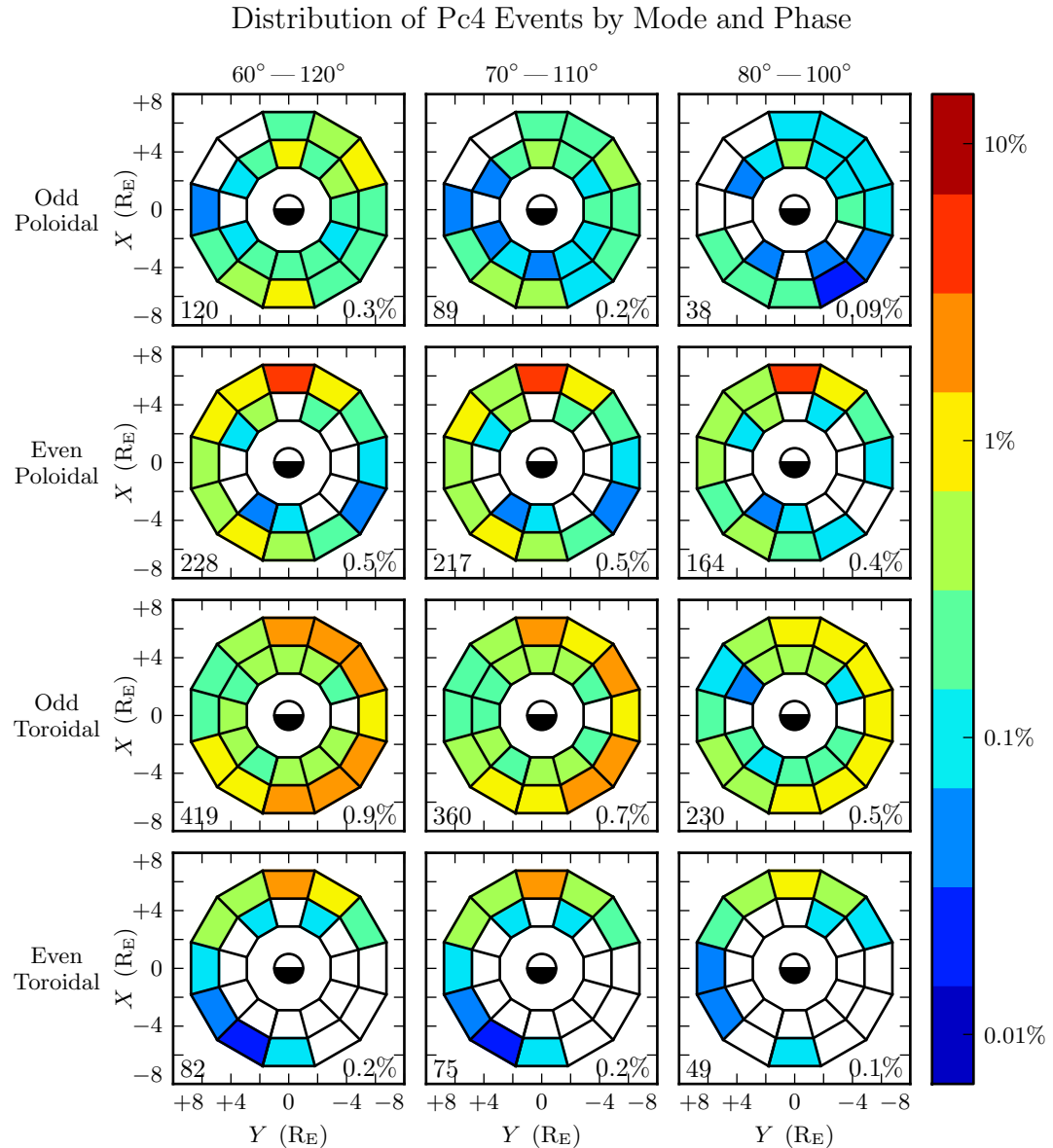


Figure 8.9: TODO: ...

8.6 Rate of Pc4 Events by Spectral Width

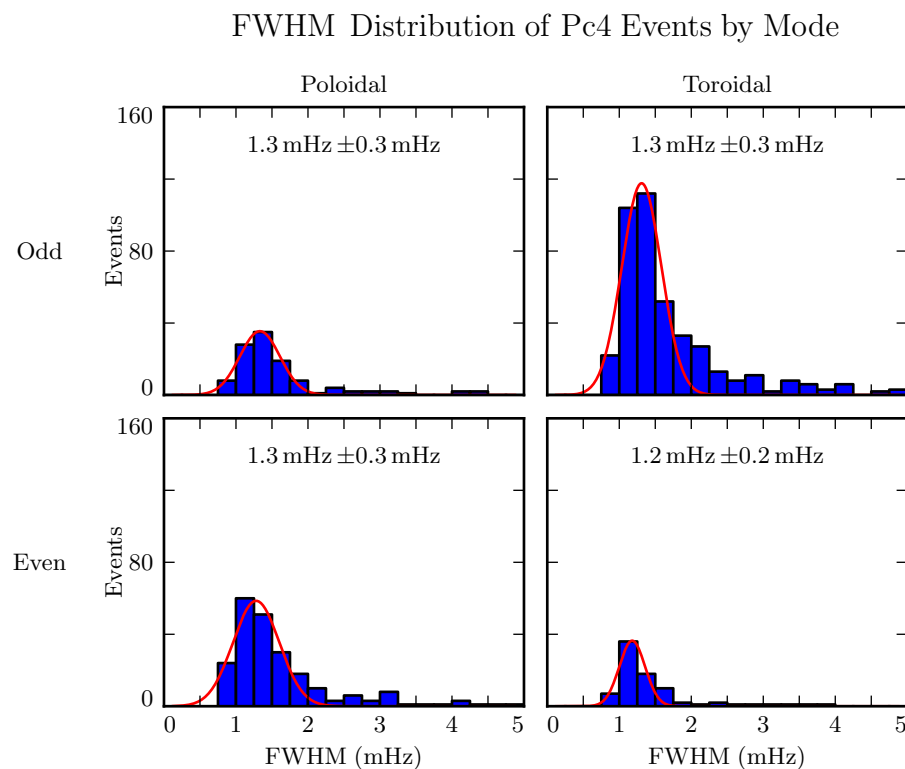


Figure 8.10: TODO: ...

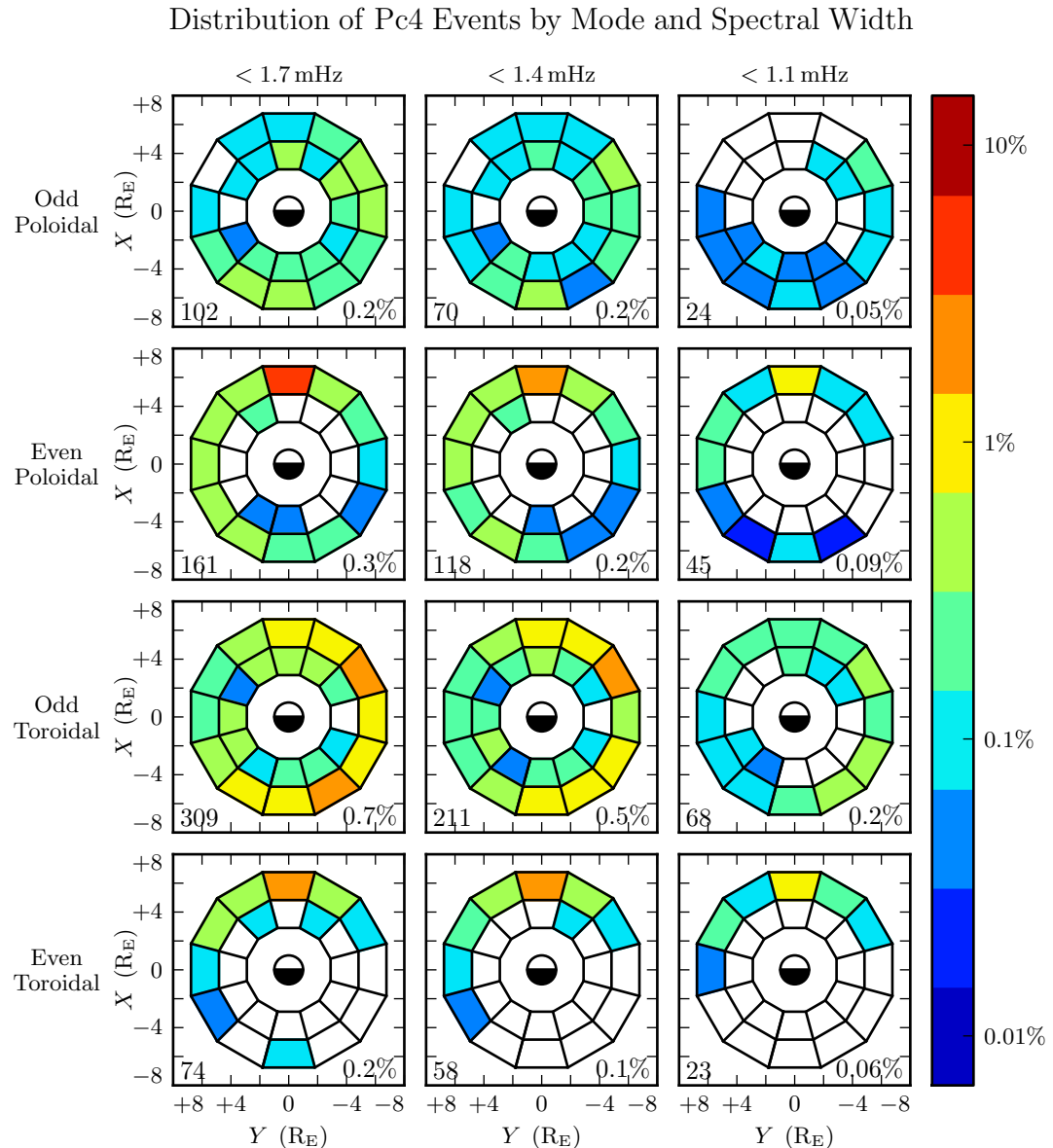


Figure 8.11: **TODO:** ...

₁₃₃₅ **8.7 Discussion**

₁₃₃₆ **TODO:** ...

1337 **Chapter 9**

1338 **Conclusion**

1339 **9.1 Summary of Results**

1340 TODO: Code development... Chapters 5 and 6

1341 TODO: Make the Git repository public, and link to it.

1342 TODO: Numerical results... Chapter 7

1343 TODO: Re-summarize the Discussion sections, I guess.

1344 TODO: Observational results... Chapter 8

1345 TODO: Link to the Git repository.

1346 **9.2 Future Work**

1347 TODO: Code development.

1348 Arbitrary deformation of grid. Get $\hat{e}_i = \frac{\partial}{\partial u^i} \underline{x}$, then $g_{ij} = \hat{e}_i \cdot \hat{e}_j$, then invert the metric tensor for contravariant components.

1350 MPI. Time to compute vs time to broadcast. This might make sense for inertial length scales.

1352 Better ionospheric profiles. Distinction between the dawn and dusk flanks. Maybe even
1353 update the conductivity based on energy deposition — precipitation causes ionization!

1354 IRI ionosphere model. Solar illumination effects.

1355 **TODO: Numerical work.**

1356 More complicated driving. Higher harmonics, non-sinusoidal waveforms. Maybe even
1357 drive based on events?

1358 **TODO: Analysis of RBSP data.**

1359 Basically just do everything over again, twice as well, once the probes have finished
1360 sampling the dayside again.

References

- 1361
- [1] S.-I. Akasofu. The development of the auroral substorm. *Planetary and Space Science*, 12(4):273–282, 1964.
 - [2] H. Alfvén. On the cosmogony of the solar system III. *Stockholms Observatoriums Annaler*, 14:9.1–9.29, 1946.
 - [3] B. J. Anderson, M. J. Engebretson, S. P. Rounds, L. J. Zanetti, and T. A. Potemra. A statistical study of Pc 3-5 pulsations observed by the AMPTE/CCE magnetic fields experiment, 1. occurrence distributions. *J. Geophys. Res.*, 95(A7):10495, 1990.
 - [4] V. Angelopoulos. The THEMIS mission. *Space Science Reviews*, 141(1-4):5–34, 2008.
 - [5] K. Birkeland. Expédition norvégienne de 1899-1900 pour l'étude des aurores boréales. *Mat. Naturvidensk. Kl.*, KI(I), 1901.
 - [6] J. P. Boris. A physically motivated solution of the Alfvén problem. *NRL Memorandum Report*, 2167, 1970.
 - [7] A. Brekke, T. Feder, and S. Berger. Pc4 giant pulsations recorded in Tromsø, 1929-1985. *Journal of Atmospheric and Terrestrial Physics*, 49(10):1027–1032, 1987.
 - [8] C. W. Carlson, R. F. Pfaff, and J. G. Watzin. The fast auroral Snapshot (FAST) mission. *Geophys. Res. Lett.*, 25(12):2013–2016, 1998.

- 1381 [9] A. A. Chan, M. Xia, and L. Chen. Anisotropic alfvén-balloon modes in Earth's
1382 magnetosphere. *J. Geophys. Res. Space Physics*, 99(A9):17351–17366, 1994.
- 1383 [10] L. Chen and A. Hasegawa. A theory of long-period magnetic pulsations: 1. steady
1384 state excitation of field line resonance. *J. Geophys. Res.*, 79(7):1024–1032, 1974.
- 1385 [11] L. Chen and A. Hasegawa. Kinetic theory of geomagnetic pulsations: 1. internal
1386 excitations by energetic particles. *J. Geophys. Res.*, 96(A2):1503, 1991.
- 1387 [12] L. Chen, R. White, C. Cheng, F. Romanelli, J. Weiland, R. Hay, J. V. Dam,
1388 D. Barnes, M. Rosenbluth, and S. Tsai. Theory and simulation of fishbone-type
1389 instabilities in beam-heated tokamaks. Technical report, 1984.
- 1390 [13] C. Z. Cheng and Q. Qian. Theory of ballooning-mirror instabilities for anisotropic
1391 pressure plasmas in the magnetosphere. *J. Geophys. Res.*, 99(A6):11193, 1994.
- 1392 [14] G. Chisham and D. Orr. Statistical studies of giant pulsations (pgs): Harmonic
1393 mode. *Planetary and Space Science*, 39(7):999–1006, 1991.
- 1394 [15] W. D. Cummings, R. J. O'Sullivan, and P. J. Coleman. Standing Alfvén waves in
1395 the magnetosphere. *J. Geophys. Res.*, 74(3):778–793, 1969.
- 1396 [16] L. Dai. Collisionless magnetic reconnection via Alfvén eigenmodes. *Phys. Rev.*
1397 *Lett.*, 102(24), 2009.
- 1398 [17] L. Dai, K. Takahashi, R. Lysak, C. Wang, J. R. Wygant, C. Kletzing, J. Bonnell,
1399 C. A. Cattell, C. W. Smith, R. J. MacDowall, S. Thaller, A. Breneman, X. Tang,
1400 X. Tao, and L. Chen. Storm time occurrence and spatial distribution of Pc4
1401 poloidal ULF waves in the inner magnetosphere: A Van Allen Probes statistical
1402 study. *J. Geophys. Res. Space Physics*, 120:4748–4762, 2015.
- 1403 [18] L. Dai, K. Takahashi, J. R. Wygant, L. Chen, J. Bonnell, C. A. Cattell, S. Thaller,
1404 C. Kletzing, C. W. Smith, R. J. MacDowall, D. N. Baker, J. B. Blake, J. Fennell,
1405 S. Claudepierre, H. O. Funsten, G. D. Reeves, and H. E. Spence. Excitation of
1406 poloidal standing Alfvén waves through drift resonance wave-particle interaction.
1407 *Geophys. Res. Lett.*, 40:4127–4132, 2013.

- 1408 [19] A. W. Degeling, R. Rankin, and Q.-G. Zong. Modeling radiation belt electron
1409 acceleration by ULF fast mode waves, launched by solar wind dynamic pressure
1410 fluctuations. *J. Geophys. Res. Space Physics*, 119(11):8916–8928, 2014.
- 1411 [20] W. D. D’haeseleer, W. N. G. H. J. D. Callen, and J. L. Shohet. *Flux Coordinates*
1412 and *Magnetic Field Structure*. Springer-Verlag, New York, 1991.
- 1413 [21] D. Q. Ding, R. E. Denton, M. K. Hudson, and R. L. Lysak. An MHD simulation
1414 study of the poloidal mode field line resonance in the Earth’s dipole magneto-
1415 sphere. *J. Geophys. Res.*, 100:63–77, 1995.
- 1416 [22] J. W. Dungey. The attenuation of Alfvén waves. *J. Geophys. Res.*, 59(3):323–328,
1417 1954.
- 1418 [23] J. W. Dungey. Interplanetary magnetic field and the auroral zones. *Phys. Rev.*
1419 *Lett.*, 6(2):47–48, 1961.
- 1420 [24] A. Einstein. Die grundlage der allgemeinen relativitätstheorie. *Ann. Phys.*,
1421 354:769–822, 1916.
- 1422 [25] S. R. Elkington, M. K. Hudson, and A. A. Chan. Acceleration of relativistic
1423 electrons via drift-resonant interaction with toroidal-mode Pc-5 ULF oscillations.
1424 *Geophys. Res. Lett.*, 26(21):3273–3276, 1999.
- 1425 [26] M. J. Engebretson, D. L. Murr, K. N. Erickson, R. J. Strangeway, D. M. Klumpar,
1426 S. A. Fuselier, L. J. Zanetti, and T. A. Potemra. The spatial extent of radial
1427 magnetic pulsation events observed in the dayside near synchronous orbit. *J.*
1428 *Geophys. Res.*, 97(A9):13741, 1992.
- 1429 [27] P. T. I. Eriksson, L. G. Blomberg, A. D. M. Walker, and K.-H. Glassmeier. Poloidal
1430 ULF oscillations in the dayside magnetosphere: a Cluster study. *Ann. Geophys.*,
1431 23(7):2679–2686, 2005.
- 1432 [28] S. Fujita and T. Tamao. Duct propagation of hydromagnetic waves in the upper
1433 ionosphere, 1, electromagnetic field disturbances in high latitudes associated with
1434 localized incidence of a shear Alfvén wave. *J. Geophys. Res.*, 93(A12):14665, 1988.

- 1435 [29] K.-H. Glassmeier. Magnetometer array observations of a giant pulsation event. *J.
1436 Geophys.*, 48:127–138, 1980.
- 1437 [30] K.-H. Glassmeier. On the influence of ionospheres with non-uniform conductivity
1438 distribution on hydromagnetic waves. *J. Geophys.*, 54(2):125–137, 1984.
- 1439 [31] K.-H. Glassmeier, S. Buchert, U. Motschmann, A. Korth, and A. Pedersen. Concerning
1440 the generation of geomagnetic giant pulsations by drift-bounce resonance
1441 ring current instabilities. *Ann. Geophysicae*, 17:338–350, 1999.
- 1442 [32] K.-H. Glassmeier, D. Klimushkin, C. Othmer, and P. Mager. ULF waves at
1443 mercury: Earth, the giants, and their little brother compared. *Advances in Space
1444 Research*, 33(11):1875–1883, 2004.
- 1445 [33] C. Goertz. Kinetic alfvén waves on auroral field lines. *Planetary and Space Science*,
1446 32(11):1387–1392, 1984.
- 1447 [34] C. K. Goertz and R. W. Boswell. Magnetosphere-ionosphere coupling. *J. Geophys.
1448 Res.*, 84(A12):7239, 1979.
- 1449 [35] C. A. Green. Giant pulsations in the plasmasphere. *Planetary and Space Science*,
1450 33(10):1155–1168, 1985.
- 1451 [36] J. L. Green and S. Boardsen. Duration and extent of the great auroral storm of
1452 1859. *Advances in Space Research*, 38(2):130–135, 2006.
- 1453 [37] C. Greifinger and P. S. Greifinger. Theory of hydromagnetic propagation in the
1454 ionospheric waveguide. *J. Geophys. Res.*, 73(23):7473–7490, 1968.
- 1455 [38] B. C. Hall. *Lie Groups, Lie Algebras, and Representations*. Graduate Texts in
1456 Mathematics. Springer, New York, second edition, 2015.
- 1457 [39] Y. X. Hao, Q.-G. Zong, Y. F. Wang, X.-Z. Zhou, H. Zhang, S. Y. Fu, Z. Y.
1458 Pu, H. E. Spence, J. B. Blake, J. Bonnell, J. R. Wygant, and C. A. Kletzing.
1459 Interactions of energetic electrons with ULF waves triggered by interplanetary
1460 shock: Van allen probes observations in the magnetotail. *J. Geophys. Res. Space
1461 Physics*, 119(10):8262–8273, 2014.

- 1462 [40] L. Harang. *Pulsations in the terrestrial magnetic records at high latitude stations.*
1463 Grondahl, 1942.
- 1464 [41] O. Hillebrand, J. Muench, and R. L. McPherron. Ground-satellite correlative
1465 study of a giant pulsation event. *Journal of Geophysics Zeitschrift Geophysik*,
1466 51:129–140, 1982.
- 1467 [42] W. J. Hughes. The effect of the atmosphere and ionosphere on long period mag-
1468 netospheric micropulsations. *Planet. Space Sci.*, 22:1157–1172, 1974.
- 1469 [43] W. J. Hughes. Magnetospheric ULF waves: A tutorial with a historical perspec-
1470 tive. In M. J. Engebretson, K. Takahashi, and M. Scholer, editors, *Solar Wind*
1471 *Sources of Magnetospheric Ultra-Low-Frequency Waves*, volume 81 of *Geophys.*
1472 *Monogr.*, pages 1–12. American Geophysical Union, Washington, DC, 1994.
- 1473 [44] W. J. Hughes and D. J. Southwood. The screening of micropulsation signals by
1474 the atmosphere and ionosphere. *J. Geophys. Res.*, 81(19):3234–3240, 1976.
- 1475 [45] W. J. Hughes, D. J. Southwood, B. Mauk, R. L. McPherron, and J. N. Barfield.
1476 Alfvén waves generated by an inverted plasma energy distribution. *Nature*,
1477 275(5675):43–45, 1978.
- 1478 [46] J. A. Jacobs, Y. Kato, S. Matsushita, and V. A. Troitskaya. Classification of
1479 geomagnetic micropulsations. *J. Geophys. Res.*, 69(1):180–181, 1964.
- 1480 [47] T. Karlsson and G. T. Marklund. A statistical study of intense low-altitude electric
1481 fields observed by freja. *Geophys. Res. Lett.*, 23(9):1005–1008, 1996.
- 1482 [48] Y. Kato and T. Tsutomu. Hydromagnetic oscillations in a conducting medium
1483 with hall conduct-ivity under the uniform magnetic field. *Science reports of the*
1484 *Tohoku University. Ser. 5, Geophysics*, 7(3):147–164, 1956.
- 1485 [49] M. C. Kelley. *The Earth’s Ionosphere*. Academic Press, San Diego, second edition,
1486 1989.
- 1487 [50] R. L. Kessel. Solar wind excitation of pc5 fluctuations in the magnetosphere and
1488 on the ground. *J. Geophys. Res.*, 113(A4), 2008.

- 1489 [51] D. Y. Klimushkin, P. N. Mager, and K.-H. Glassmeier. Toroidal and poloidal
1490 Alfvén waves with arbitrary azimuthal wavenumbers in a finite pressure plasma
1491 in the earth's magnetosphere. *Annales Geophysicae*, 22(1):267–287, 2004.
- 1492 [52] S. Kokubun. Observations of Pc pulsations in the magnetosphere: Satellite-ground
1493 correlation. *J. Geomagn. Geoelec*, 32(Supplement2):SII17–SII39, 1980.
- 1494 [53] S. Kokubun, K. N. Erickson, T. A. Fritz, and R. L. McPherron. Local time asym-
1495 metry of Pc 4-5 pulsations and associated particle modulations at synchronous
1496 orbit. *J. Geophys. Res.*, 94(A6):6607–6625, 1989.
- 1497 [54] D.-H. Lee and K. Kim. Compressional MHD waves in the magnetosphere: A new
1498 approach. *J. Geophys. Res.*, 104(A6):12379–12385, 1999.
- 1499 [55] A. S. Leonovich and V. A. Mazur. Structure of magnetosonic eigenoscillations of
1500 an axisymmetric magnetosphere. *J. Geophys. Res.*, 105(A12):27707–27715, 2000.
- 1501 [56] W. Liu, J. B. Cao, X. Li, T. E. Sarris, Q.-G. Zong, M. Hartinger, K. Takahashi,
1502 H. Zhang, Q. Q. Shi, and V. Angelopoulos. Poloidal ULF wave observed in the
1503 plasmasphere boundary layer. *J. Geophys. Res. Space Physics*, 118(7):4298–4307,
1504 2013.
- 1505 [57] W. Liu, T. E. Sarris, X. Li, S. R. Elkington, R. Ergun, V. Angelopoulos, J. Bonnell,
1506 and K. H. Glassmeier. Electric and magnetic field observations of Pc4 and Pc5
1507 pulsations in the inner magnetosphere: A statistical study. *J. Geophys. Res.*,
1508 114(A12), 2009.
- 1509 [58] W. Liu, T. E. Sarris, X. Li, Q.-G. Zong, R. Ergun, V. Angelopoulos, and K. H.
1510 Glassmeier. Spatial structure and temporal evolution of a dayside poloidal ULF
1511 wave event. *Geophys. Res. Lett.*, 38(19), 2011.
- 1512 [59] R. L. Lysak. Magnetosphere-ionosphere coupling by Alfvén waves at midlatitudes.
1513 *J. Geophys. Res.*, 109, 2004.
- 1514 [60] R. L. Lysak and D. hun Lee. Response of the dipole magnetosphere to pressure
1515 pulses. *Geophys. Res. Lett.*, 19(9):937–940, 1992.

- 1516 [61] R. L. Lysak and Y. Song. A three-dimensional model of the propagation of Alfvén
1517 waves through the auroral ionosphere: first results. *Adv. Space Res.*, 28:813–822,
1518 2001.
- 1519 [62] R. L. Lysak, C. L. Waters, and M. D. Sciffer. Modeling of the ionospheric Alfvén
1520 resonator in dipolar geometry. *J. Geophys. Res. Space Physics*, 118, 2013.
- 1521 [63] P. N. Mager and D. Y. Klimushkin. Giant pulsations as modes of a transverse
1522 Alfvénic resonator on the plasmapause. *Earth, Planets and Space*, 65(5):397–409,
1523 2013.
- 1524 [64] I. R. Mann, E. A. Lee, S. G. Claudepierre, J. F. Fennell, A. Degeling, I. J. Rae,
1525 D. N. Baker, G. D. Reeves, H. E. Spence, L. G. Ozeke, R. Rankin, D. K. Milling,
1526 A. Kale, R. H. W. Friedel, and F. Honary. Discovery of the action of a geophysical
1527 synchrotron in the Earth’s Van Allen radiation belts. *Nature Communications*, 4,
1528 2013.
- 1529 [65] I. R. Mann and A. N. Wright. Finite lifetimes of ideal poloidal Alfvén waves. *J.
1530 Geophys. Res.*, 100:23677–23686, 1995.
- 1531 [66] I. R. Mann, A. N. Wright, and A. W. Hood. Multiple-timescales analysis of ideal
1532 poloidal Alfvén waves. *J. Geophys. Res.*, 102(A2):2381–2390, 1997.
- 1533 [67] T. Maynard, N. Smith, S. Gonzalez, et al. Solar storm risk to the North American
1534 electric grid. 2013.
- 1535 [68] K. McGuire, R. Goldston, M. Bell, M. Bitter, K. Bol, K. Brau, D. Buchenauer,
1536 T. Crowley, S. Davis, F. Dylla, H. Eubank, H. Fishman, R. Fonck, B. Grek,
1537 R. Grimm, R. Hawryluk, H. Hsuan, R. Hulse, R. Izzo, R. Kaita, S. Kaye, H. Kugel,
1538 D. Johnson, J. Manickam, D. Manos, D. Mansfield, E. Mazzucato, R. McCann,
1539 D. McCune, D. Monticello, R. Motley, D. Mueller, K. Oasa, M. Okabayashi,
1540 K. Owens, W. Park, M. Reusch, N. Sauthoff, G. Schmidt, S. Sesnic, J. Strachan,
1541 C. Surko, R. Slusher, H. Takahashi, F. Tenney, P. Thomas, H. Towner, J. Valley,
1542 and R. White. Study of high-beta magnetohydrodynamic modes and fast-ion
1543 losses in PDX. *Phys. Rev. Lett.*, 50(12):891–895, 1983.

- 1544 [69] R. L. McPherron. The role of substorms in the generation of magnetic storms.
1545 *Washington DC American Geophysical Union Geophysical Monograph Series*,
1546 98:131–147, 1997.
- 1547 [70] R. L. McPherron, G. K. Parks, D. S. Colburn, and M. D. Montgomery. Satellite
1548 studies of magnetospheric substorms on august 15, 1968: 2. solar wind and outer
1549 magnetosphere. *J. Geophys. Res.*, 78(16):3054–3061, 1973.
- 1550 [71] T. Motoba, K. Takahashi, J. V. Rodriguez, and C. T. Russell. Giant pulsations on
1551 the afternoonside: Geostationary satellite and ground observations. *J. Geophys.*
1552 *Res. Space Physics*, 120:8350–8367, 2015.
- 1553 [72] NASA. Coordinated data analysis (workshop) web.
- 1554 [73] NASA. Near miss: The solar superstorm of july 2012.
- 1555 [74] M. Nicolet. The collision frequency of electrons in the ionosphere. *Journal of*
1556 *Atmospheric and Terrestrial Physics*, 3(4):200–211, 1953.
- 1557 [75] L. G. Ozeke and I. R. Mann. Energization of radiation belt electrons by ring
1558 current ion driven ULF waves. *J. Geophys. Res.*, 113(A2), 2008.
- 1559 [76] E. M. Poulter, W. Allan, E. Nielsen, and K.-H. Glassmeier. Stare radar observa-
1560 tions of a PG pulsation. *J. Geophys. Res.*, 88(A7):5668, 1983.
- 1561 [77] J. A. Proehl, W. Lotko, I. Kouznetsov, and S. D. Geimer. Ultralow-frequency
1562 magnetohydrodynamics in boundary-constrained geomagnetic flux coordinates.
1563 *J. Geophys. Res.*, 107(A9):1225, 2002.
- 1564 [78] H. R. Radoski. A note on oscillating field lines. *J. Geophys. Res.*, 72(1), 1967.
- 1565 [79] H. R. Radoski. A theory of latitude dependent geomagnetic micropulsations: The
1566 asymptotic fields. *J. Geophys. Res.*, 79, 1974.
- 1567 [80] R. Rankin, J. C. Samson, and V. T. Tikhonchuk. Parallel electric fields in dis-
1568 persive shear alfvén waves in the dipolar magnetosphere. *Geophys. Res. Lett.*,
1569 26(24):3601–3604, 1999.
- 1570 [81] B. Rolf. Giant micropulsations at abisko. *J. Geophys. Res.*, 36(1):9, 1931.

- 1571 [82] G. Rostoker, H.-L. Lam, and J. V. Olson. PC 4 giant pulsations in the morning
1572 sector. *J. Geophys. Res.*, 84(A9):5153, 1979.
- 1573 [83] J. C. Samson, L. L. Cogger, and Q. Pao. Observations of field line resonances,
1574 auroral arcs, and auroral vortex structures. *J. Geophys. Res.*, 101(A8):17373–
1575 17383, 1996.
- 1576 [84] H. J. Singer, W. J. Hughes, and C. T. Russell. Standing hydromagnetic waves
1577 observed by ISEE 1 and 2: Radial extent and harmonic. *J. Geophys. Res.*,
1578 87(A5):3519, 1982.
- 1579 [85] D. J. Southwood. Some features of field line resonances in the magnetosphere.
1580 *Planetary and Space Science*, 22(3):483–491, 1974.
- 1581 [86] D. J. Southwood. A general approach to low-frequency instability in the ring
1582 current plasma. *J. Geophys. Res.*, 81(19):3340–3348, 1976.
- 1583 [87] J. Stratton and N. J. Fox. Radiation belt storm probes (RBSP) mission overview.
1584 In *2012 IEEE Aerospace Conference*. Institute of Electrical & Electronics Engi-
1585 neers (IEEE), 2012.
- 1586 [88] E. Sucksdorff. Giant pulsations recorded at sodankyl during 19141938. *Terrestrial
1587 Magnetism and Atmospheric Electricity*, 44(2):157–170, 1939.
- 1588 [89] K. Takahashi, J. Bonnell, K.-H. Glassmeier, V. Angelopoulos, H. J. Singer, P. J.
1589 Chi, R. E. Denton, Y. Nishimura, D.-H. Lee, M. Nosé, and W. Liu. Multipoint
1590 observation of fast mode waves trapped in the dayside plasmasphere. *J. Geophys.
1591 Res.*, 115(A12), 2010.
- 1592 [90] K. Takahashi, K.-H. Glassmeier, V. Angelopoulos, J. Bonnell, Y. Nishimura, H. J.
1593 Singer, and C. T. Russell. Multisatellite observations of a giant pulsation event.
1594 *J. Geophys. Res.*, 116:A11223, 2011.
- 1595 [91] K. Takahashi, M. D. Hartinger, V. Angelopoulos, K.-H. Glassmeier, and H. J.
1596 Singer. Multispacecraft observations of fundamental poloidal waves without
1597 ground magnetic signatures. *J. Geophys. Res. Space Physics*, 118:4319–4334, 2013.

- 1598 [92] K. Takahashi, R. W. McEntire, A. T. Y. Lui, and T. A. Potemra. Ion flux oscillations associated with a radially polarized transverse Pc 5 magnetic pulsation. *J. Geophys. Res.*, 95(A4):3717, 1990.
- 1599
- 1600
- 1601 [93] K. Takahashi, N. Sato, J. Warnecke, H. Lühr, H. E. Spence, and Y. Tonegawa. On the standing wave mode of giant pulsations. *J. Geophys. Res. Space Physics*, 97(A7):10717–10732, 1992.
- 1602
- 1603
- 1604 [94] B. J. Thompson and R. L. Lysak. Electron acceleration by inertial alfvén waves. *J. Geophys. Res.*, 101(A3):5359–5369, 1996.
- 1605
- 1606 [95] S. M. Thompson and M. G. Kivelson. New evidence for the origin of giant pulsations. *J. Geophys. Res.*, 106(A10):21237–21253, 2001.
- 1607
- 1608 [96] V. T. Tikhonchuk and R. Rankin. Electron kinetic effects in standing shear alfvén waves in the dipolar magnetosphere. *Physics of Plasmas*, 7(6):2630, 2000.
- 1609
- 1610 [97] B. T. Tsurutani, W. D. Gonzalez, G. S. Lakhina, and S. Alex. The extreme magnetic storm of 12 september 1859. *Journal of Geophysical Research: Space Physics*, 108(A7), 2003. 1268.
- 1611
- 1612
- 1613 [98] A. Y. Ukhorskiy. Impact of toroidal ULF waves on the outer radiation belt electrons. *J. Geophys. Res.*, 110(A10), 2005.
- 1614
- 1615 [99] J. Veldkamp. A giant geomagnetic pulsation. *Journal of Atmospheric and Terrestrial Physics*, 17(4):320–324, 1960.
- 1616
- 1617 [100] J. A. Wanliss and K. M. Showalter. High-resolution global storm index: Dst versus sym-h. *Journal of Geophysical Research: Space Physics*, 111(A2):n/a–n/a, 2006. A02202.
- 1618
- 1619
- 1620 [101] C. L. Waters, R. L. Lysak, and M. D. Sciffer. On the coupling of fast and shear Alfvén wave modes by the ionospheric Hall conductance. *Earth Planets Space*, 65:385–396, 2013.
- 1621
- 1622
- 1623 [102] C. L. Waters and M. D. Sciffer. Field line resonant frequencies and ionospheric conductance: Results from a 2-d MHD model. *J. Geophys. Res.*, 113(A5), 2008.
- 1624

- 1625 [103] D. M. Wright and T. K. Yeoman. High-latitude HF doppler observations of ULF
1626 waves: 2. waves with small spatial scale sizes. *Ann. Geophys.*, 17(7):868–876,
1627 1999.
- 1628 [104] J. R. Wygant, A. Keiling, C. A. Cattell, R. L. Lysak, M. Temerin, F. S. Mozer,
1629 C. A. Kletzing, J. D. Scudder, V. Streitsov, W. Lotko, and C. T. Russell. Evidence
1630 for kinetic alfvn waves and parallel electron energization at 46 re altitudes in the
1631 plasma sheet boundary layer. *Journal of Geophysical Research: Space Physics*,
1632 107(A8):SMP 24–1–SMP 24–15, 2002.
- 1633 [105] B. Yang, Q.-G. Zong, Y. F. Wang, S. Y. Fu, P. Song, H. S. Fu, A. Korth, T. Tian,
1634 and H. Reme. Cluster observations of simultaneous resonant interactions of ULF
1635 waves with energetic electrons and thermal ion species in the inner magnetosphere.
1636 *J. Geophys. Res.*, 115(A2), 2010.
- 1637 [106] K. Yee. Numerical solution of initial boundary value problems involving maxwell's
1638 equations in isotropic media. *IEEE Trans. Antennas Propagat.*, 14(3), 1966.
- 1639 [107] T. K. Yeoman and D. M. Wright. ULF waves with drift resonance and drift-bounce
1640 resonance energy sources as observed in artificially-induced HF radar backscatter.
1641 *Ann. Geophys.*, 19(2):159–170, 2001.
- 1642 [108] Q.-G. Zong, X.-Z. Zhou, X. Li, P. Song, S. Y. Fu, D. N. Baker, Z. Y. Pu, T. A.
1643 Fritz, P. Daly, A. Balogh, and H. Réme. Ultralow frequency modulation of ener-
1644 getic particles in the dayside magnetosphere. *Geophys. Res. Lett.*, 34(12), 2007.
- 1645 [109] Q.-G. Zong, X.-Z. Zhou, Y. F. Wang, X. Li, P. Song, D. N. Baker, T. A. Fritz,
1646 P. W. Daly, M. Dunlop, and A. Pedersen. Energetic electron response to ULF
1647 waves induced by interplanetary shocks in the outer radiation belt. *J. Geophys.*
1648 *Res.*, 114(A10), 2009.